Investigation of the Energy Gaps in Cuprate Superconductors

Dissertation

zur

Erlangung der naturwissenschaftlichen Doktorwürde
(Dr. sc. nat.)

vorgelegt der

Mathematisch-naturwissenschaftlichen Fakultät

der

Universität Zürich

von

Simon Strässle
von
Kirchberg SG

Promotionskomitee

Prof. Dr. Hugo Keller (Vorsitz)
Dr. Josef Roos (Leitung der Dissertation)
Prof. Dr. Mikhail V. Eremin
Dr. Jorge L. Gavilano

Zürich, 2009

Meiner Familie

Die vorliegende Arbeit wurde von der Mathematisch-naturwissenschaftlichen Fakultät der Universität Zürich auf Antrag von Prof. Dr. Hugo Keller als Dissertation angenommen.

Dank

Gerne möchte ich mich herzlich bei all jenen bedanken, die zum Gelingen dieser Arbeit beigetragen haben. Meine Zeit am Physik-Institut der Universität Zürich war eine sehr lehrreiche und dank der freundlichen und konstruktiven Arbeitsatmosphäre, dank einer Vielzahl von Leuten, die nachfolgend nicht persönlich erwähnt sind - danke! - auch eine schöne Zeit.

Als erstes möchte ich Prof. Hugo Keller für die Möglichkeit danken, meine Doktorarbeit in seiner Arbeitsgruppe durchzuführen. Die gewährte Freiheit, die vielfältigen Möglichkeiten und die gebotene Unterstützung, in finanzieller, wie auch in wissenschaftlicher Hinsicht, haben es mir erlaubt, wertvolle Erfahrungen in verschiedensten Gebieten zu sammeln. Trotz seiner knappen Zeit konnte ich stets auf eine fundierte Meinung und seine konstruktive Kritik zählen.

Dr. Josef Roos möchte ich für die tatkräftige und äusserst kompetente Unterstützung beim Experimentieren und die unzähligen Diskussionen, die im vergangenen halben Jahrzehnt nicht nur Physik, sondern auch oft das Leben zum Inhalt hatten, herzlich danken. Ich habe in vielen Bereichen sehr von seiner reichen Erfahrung profitiert.

Ein grosses Dankeschön auch an Dr. Mihael Mali, der mit seinem enormen Wissen über Physik und seinem Ideenreichtum stets eine ausgesprochene Bereicherung in jeder Diskussion ist. Seine immerzu freundliche Bereitschaft gewonnene Resultate zu diskutieren sei herzlich verdankt.

I would like to thank Dr. Rustem Khasanov for introducing me to the muons, and especially for all the valuable discussions on the various day and night shifts during beam times. It was always a pleasure to work together - his enthusiasm is simply contagious.

Herzlichen Dank auch Dr. Björn Graneli für die freundschaftliche Zusammenarbeit, auch wenn das Projekt mal etwas harzig gelaufen ist. Es war ihm nie zuviel, selbst mitten in der Nacht sich ins Labor aufzumachen, um eine neue Messung zu starten. Herzlichst verdankt sei auch das Korrekturlesen des vorliegenden Textes.

Stephen Weyeneth sei Dank für die lückenlose Versorgung mit flüssigem Helium, die ebenfalls zahlreichen Diskussionen und die gute Teamarbeit, wenn's mal etwas für die 'Doktoranden' zu tun gab.

Prof. Peter Meier gebührt Dank für die zahlreichen Diskussionen bezüglich theoretischer Aspekte der Kernspinresonanz. Prof. Andreas Schilling danke ich für die etlichen aufschlussreichen Gespräche, insbesondere über Vortexphysik.

Vielen Dank auch der Werkstatt für die Mithilfe beim Planen und Realisieren von Verbesserungen und Erweiterungen der Apparaturen. Die Arbeiten wurden stets zur vollsten Zufriedenheit ausgeführt. Besonders wertvoll empfand ich auch die spontane Bereitschaft eine dringliche Sache auch mal kurzerhand in der Kaffeepause zu erledigen.

Gute Experimente bedingen gute Proben - Dank gebührt Dr. Janusz Kaprinski und seiner Gruppe, wie auch PD Dr. Kazimierz Conder und seinen Mitarbeitern für die Herstellung zahlreicher Substanzen ausgezeichneter Qualität.

Walter Fässler danke ich für die stete Bereitschaft Dinge zu organisieren und durstige Apparaturen mit Kryoflüssigkeit zu tränken; Tiziano Crudeli für das Erstellen vieler schöner Bildchen für Vorträge und Manuskripte.

Thanks to Aaron Manalaysay for the help, when my English skills were not enough.

Many thanks to Alex Gafner, Alexander Maisuradze, Bastian Woyek, Dimitry Eshchenko, Fabio La Mattina, Ferenc Muranyi, Holger Bartolf, Petra Häfliger, Raffaele Dell Amore, Stefan Kohout, and Stefan Siegrist, and to everyone who was offering helping hands and minds.

Zu guter Letzt danke ich herzlichst meiner Familie für die fortwährende Unterstützung und die liebevolle Aufmunterung, wenn der Weg mal etwas steinig war.

Abstract

The cuprates constitute a fascinating class of material that hosts many physical phenomena not encountered in other solids. The most prominent feature is perhaps the transition to a superconducting state at a comparatively high temperature T_c, even exceeding 135 K in some compounds. Furthermore, a so-called pseudogap phase has been discovered, which is a peculiar state of the electronic system, associated with a partial gap in the electronic excitation spectrum. The superconducting energy gap and the pseudogap both open at the Fermi energy, but the pseudogap can appear already at temperatures substantially higher than T_c. Two decades of intense study since the discovery of these phenomena there is still no consensus on their origin and interplay. The research on cuprates remains, however, highly active. On the one hand the obvious potential for technical application of cuprates stokes justified hopes for new energy-efficient technologies, while on the other, the scientific challenge of understanding the physics involved prods researchers all over the world.

The first part of this Thesis is dedicated to our efforts to elucidate the nature of the pseudogap phase and its relevance for the occurrence of superconductivity. In the second part, we outline our investigations concerning the superconducting energy gap and the underlying mechanism responsible for its formation. A variety of methods, such as nuclear magnetic resonance (NMR), nuclear quadrupole resonance (NQR), muon-spin rotation (μSR), and magnetic susceptibility measurements was applied in our studies of various cuprate superconductors.

The notion of orbital currents for explaining the pseudogap phase has received wide attention in recent years, but no unambiguous experimental evidence confirms this proposed ordered state. Using NMR, we searched for magnetic fields associated with the orbital currents that are expected to appear in the copper-oxide planes of the cuprates. Our ^{89}Y NMR study of $Y_2Ba_4Cu_7O_{15-\delta}$ did not reveal any clear signature of orbital currents. From experimental results, limits for additional magnetic fields at the Y-site were deduced. Static magnetic fields as well as dynamic field amplitudes were investigated. Due to the specific properties of the bi-layer compound, a possible interaction between currents originating in neighboring copper-oxide planes was also considered. It was concluded that any additional static magnetic field at the Y-site, appearing in the normal-conducting state below room temperature, must be $\lesssim 0.15$ mT. For the fluctuating field amplitude, an upper limit of ~ 0.7 mT was determined. These values are considerably smaller than theoretical predictions for Y-Ba-Cu-O in the range of several tens of mT, thus imposing significant constraints on orbital-current models.

Another theoretical approach relates the occurrence of the pseudogap phase to charge inhomogeneity. In order to verify this conjecture, the Y-atom in optimally doped $YB_2Cu_3O_{7-\delta}$ was substituted for La, which has a nuclear quadrupole moment, thus enabling a direct test of charge effects by means of NMR/NQR. NMR relevant parameters for the La, such as the ^{139}La magnetic shift tensor, the quadrupole frequency, and the asymmetry parameter were successfully determined. The present status of our ^{139}La NMR/NQR investigation, however, does not allow conclusive statements about the role of charge inhomogeneity in cuprates. Further efforts are required, in particular to clarify the unusual and complex behavior of the nuclear relaxation. The spin-spin relaxation

of ^{139}La appears to be ambiguous and the findings strongly depend on effects that are expected to be of minor relevance for superconductivity. From the temperature dependence of the ^{139}La spin-lattice relaxation, however, it is evident that charge effects are indeed involved in the nuclear spin dynamics.

In order to investigate the role of the pseudogap in high-temperature superconductivity a μSR study on optimally doped $(BiPb)_2(SrLa)_2CuO_{6+\delta}$ single crystals was performed. From the field dependence of the μSR depolarization rate we concluded that the superfluid density in the copper-oxide planes shows a behavior that excludes isotropic s-wave superconductivity, but is consistent with a dominant d-wave order parameter. The comparison of the measured temperature dependence of the magnetic field penetration depth λ with results from a calculation using angular resolved photoemission data from a similar sample, suggests that the pseudogap and the superconducting phase are dominated by different parts of the Fermi surface, and indicates that the two phases coexist.

The question about the nature of the mechanism responsible for superconductivity was approached using magnetization measurements in low magnetic fields. Using powder samples the oxygen-isotope effect for the zero-temperature superconducting energy gap in $Y_{1-x}Pr_xBa_2Cu_3O_{7-\delta}$, including the doping dependence, was determined here for the first time. A non-trivial linear relation between the isotope effects on the gap and on T_c was found. Both isotope effects are most pronounced in the underdoped regime, and decrease toward optimum doping, eventually reversing the sign around optimum doping. This doping dependence, including the sign reversal, was predicted by model calculations based on polaron formation, and is not expected considering purely electronic mechanisms only. The presence of a substantial isotope effect shows the importance of the lattice for the physics of cuprate superconductivity.

The complex nature of the superconducting energy gap was further investigated by means of μSR experiments on single crystalline $YBa_2Cu_3O_{7-\delta}$. The μSR depolarization rate, which is proportional to the in-plane superfluid density, shows a distinct increase towards low temperatures as temperature is decreased. This behavior is expected for a two-gap mechanism for which one gap is considerably smaller. In contrast, the out-of-plane superfluid density saturates as the temperature decreases. The μSR data suggest the presence of a major d-wave gap in the copper-oxide planes of cuprates, which mixes with an isotropic gap and dominates the out-of-plane superfluid density. Due to this mixing a small s-wave component is also present in the in-plane superfluid density. This emphasizes the importance of the third dimension for the cuprates and limits the validity two-dimensional approaches that focus exclusively on the copper-oxide planes.

Zusammenfassung

Kuprate bilden eine äusserst interessante Werkstoffgruppe, die einige faszinierende fest-körperphysikalische Eigenschaften in sich vereint. Die mitunter bemerkenswerteste ist das Auftreten von Supraleitung bei rekordhohen Übergangstemperaturen von über 135 K. Des Weiteren wurde in den Kupraten die sogenannte Pseudogap-Phase lokalisiert, welche durch eine partielle Energielücke im elektronischen Anregungsspekrum charakterisiert ist. Die Energielücke, die mit der Supraleitung assoziiert ist, wie auch jene der Pseudogap-Phase, erscheinen beide an der Fermifläche, wobei sich die Pseudoenergielücke bereits bei deutlich höheren Temperaturen stabilisiert. Selbst nach zwei Jahrzehnten weltweiter intensivster Forschungsarbeit ist die Ursache, wie auch der genaue Zusammenhang der beiden Phänomene nicht vollständig geklärt. Diese fundamentalen Fragen bleiben dank berechtigter Hoffnungen auf neue energieeffiziente Technologien Gegenstand vieler Forschungsprojekte und einen Forschungsgruppen im Bestreben um Erkenntnis um den ganzen Globus.

Der erste Teil dieser Arbeit beschreibt unsere Experimente mit dem Ziel Neues zum grundlegenden Verständnis der Pseudogap-Phase beizutragen und Hinweise bezüglich deren Relevanz für das Auftreten der Hochtemperatursupraleitung zu finden. Im zweiten Teil werden unsere Untersuchungen zur attraktiven Wechselwirkung beschrieben, die zur Cooperpaarbildung und somit zur Supraleitung führt. Desweiteren werden Studien der Supraleiterenergielücke präsentiert. Zu den verwendeten Untersuchungsmethoden zählen die Kernspinresonanz (NMR), die Kernquadrupolresonanz (NQR), die Muonspinrotation (μSR) und die Messung der magnetischen Suszeptibilität, angewandt auf unterschiedliche Kupratsupraleiter.

In jüngster Zeit hat der Ansatz orbitaler Ströme, die in der Kupferoxidebene der Kuprate fliessen sollen, zur Erklärung der Pseudogap-Phase an Beachtung gewonnen. Bis heute fehlt jedoch der klare experimentelle Nachweis dieser Ströme. NMR ist eine sensitive Methode, bestens geeignet zur Messung der von möglichen orbitalen Strömen herrührenden Magnetfelder. Unsere ^{89}Y-NMR-Studie des $Y_2Ba_4Cu_7O_{15-\delta}$-Supraleiters hat keine direkten Hinweise für die Existenz orbitaler Ströme ergeben. Anhand der Daten wurde das maximale, von möglichen orbitalen Strömen verursachte Magnetfeld am Y-Platz ermittelt. Die spezifischen Eigenschaften des untersuchten Kuprates erlaubten es zudem, eine mögliche Wechselwirkung zwischen orbitalen Strömen benachbarter Kupferoxidebenen miteinzubeziehen. Aufgrund der Datenlage wurde gefolgert, dass statische Magnetfelder, die beim Eintritt in die Pseudogap-Phase erscheinen, kleiner als ~ 0.15 mT sind. Für die Obergrenze der Amplitude fluktuierender Magnetfelder wurde ein Wert von ~ 0.7 mT gefunden. Diese Grenzwerte unterschreiten die für Y-Ba-Cu-O-Materialien theoretisch vorhergesagten deutlich und stellen zwingende Bedingungen an Modelle orbitaler Ströme.

Ein weiterer Erklärungsversuch der Pseudogap-Phase thematisiert Effekte inhomogener Ladungsverteilung der Leitungselektronen. Um solche Ladungseffekte aufspüren zu können, wurde Y in optimal dotiertem $YB_2Cu_3O_{7-\delta}$ durch La ersetzt. Der La-Kern trägt ein Quadrupolmoment und verhält sich daher in NMR/NQR-Messungen sensitiv auf Ladungseffekte. Es wurden NMR-Parameter, wie der magnetische Verschiebungstensor, die Quadrupolfrequenz und der Asymmetrieparameter von ^{139}La bestimmt. Der

aktuelle Stand unserer ^{139}La-NMR/NQR-Studie lässt zur Zeit noch keine konkreten Schlussfolgerungen bezüglich der Relevanz von Ladungseffekten für Kupratsupraleitung zu. Es müssen weitere experimentelle Anstrengungen unternommen werden, um das komplexe Kernspinrelaxationsverhalten zu klären. Die Temperaturabhängigkeit der nuklearen Spin-Spin-Relaxationsrate scheint stark von Effekten beeinflusst, die nichts mit der Supraleitung zu tun haben, das unerwartete Temperaturverhalten der nuklearen Spin-Gitter-Relaxation von ^{139}La lässt auf die Beteiligung von Ladungseffekten schliessen.

Der Zusammenhang zwischen der Pseudogap- und der Supraleiterphase war Gegenstand einer μSR-Studie, durchgeführt an optimal dotierten $(BiPb)_2(SrLa)_2CuO_{6+\delta}$-Einkristallen. Die Magnetfeldabhängigkeit gewisser μSR-relevanter Parameter ist konsistent mit der Annahme, dass in diesem Material nicht ein konventioneller *s*-wellenartiger, sondern ein *d*-wellenartiger Supraleitungsordnungsparameter realisiert ist. Der direkte Vergleich von Berechnungen, basierend auf Resultaten winkelaufgelöster Photoemssions-Exerimente, mit Ergebnissen unserer μSR-Untersuchung legt nahe, dass das Phänomen der Supraleitung und jenes des Pseudogap-Zustandes von unterschiedlichen Regionen der Fermifläche dominiert werden, was wiederum darauf hindeutet, dass diese beiden Phasen nicht in direktem Zusammenhang stehen, sondern koexistieren. Weitere Untersuchungen zur Stützung dieser Aussage sind erforderlich.

In einem weiteren Projekt wurde der Einfluss eines Sauerstoffisotopenaustausches auf die Supraleiterenergielücke von $Y_{1-x}Pr_xBa_2Cu_3O_{7-\delta}$ mittels Messungen der magnetischen Suszeptibilität von Pulverproben untersucht. Diese Arbeit zielte darauf ab, das Verständnis um die attraktive Wechselwirkung, welche zur Supraleitung führt, zu mehren. Der Isotopeneffekt der Supraleiterenergielücke, einschliesslich dessen Dotierungsabhängigkeit, wurde erstmals betimmt. Ein nicht-trivialer linearer Zusammenhang zwischen dem Isotopeneffekt der Supraleiterenergielücke und demjenigen der Übergangstemperatur wurde gefunden. Es zeigte sich, dass der Einfluss des Isotopenaustausches mit zunehmender Dotierung sich zusehends vermindert, und schliesslich gar das Vorzeichen bei nahezu optimaler Dotierung ändert. Der gefundene Dotierungsverlauf entspricht der Vorhersage eines Modells, das auf Polaronen basiert. Das Auftreten des Isotopeneffekts weist deutlich auf die Beteiligung von Gittereffekten zur Kupratsupraleitung hin.

Die komplexe Natur der Supraleiterenergielücke wurde in einer weiteren μSR-Untersuchung eines $YBa_2Cu_3O_{7-\delta}$-Einkristalles genauer studiert. Ein signifikanter Anstieg der μSR-Depolarisationsrate, welche sich proportional zur planaren superfluiden Dichte des Supraleiters verhält, wurde bei tiefen Temperaturen festgestellt. Diese Beobachtung lässt sich durch Multi-Band-Supraleitung erklären, wobei eine der Supraleiterenergielücken, welche jeweils mit verschiedenen Bändern assoziiert sind, im Vergleich zu einer anderen deutlich kleiner sein muss. Im Gegensatz dazu sättigt die suprafluide Dichte mit sinkender Temperatur für die Komponente senkrecht zu den Kupferoxidschichten. Die μSR-Daten legen daher eine Supraleiterenergielücke mit dominant *d*-wellenartiger Komponente in den Kupferoxidschichten und einer dominat *s*-wellenartigen Komponente senkrecht nahe, wobei wegen der Wechselwirkung zwischen den verschiedenen Bändern in der planaren superfluiden Dichte eine Beimischung der *s*-Komponente und in derjenigen senkrecht zu den Schichten eine *d*-wellenartige Beimischung vorhanden scheint, was verdeutlicht, dass Erklärungsversuche der Supraleitung, welche sich ausschliesslich auf die Kupferoxidebenen der Kuprate konzentrieren, Wesentliches vernachlässigen.

Contents

List of acronyms

NMR	Nuclear Magnetic Resonance
NQR	Nuclear Quadrupole Resonance
μSR	Muon-Spin Rotation
ARPES	Angle Resolved Photoemission Spectroscopy
PSI	Paul Scherrer Institut
CC	Circulating Current
DDW	d-Density Wave
BCS	Bardeen Cooper Schrieffer
YBCO	Y-Ba-Cu-O cuprate family
Y123	$YBa_2Cu_3O_{7-\delta}$
Y1237	$YBa_2Cu_3O_7$
Y124	$YBa_2Cu_4O_8$
Y247	$Y_2Ba_4Cu_7O_{15-\delta}$
LSCO	La-Sr-Cu-O cuprate family
OP Bi2201	optimally doped $(BiPb)_2(SrLa)_2CuO_{6+\delta}$
AC	Alternating Current
DC	Direct Current
MPMS	Magnetic Property Measurement System
PPMS	Physical Property Measurement System

1 Preface

In 1908, H. Kamerlingh-Onnes succeeded in liquifying helium. This milestone achievement of cryogenics extended the accessible temperature range down to just a few Kelvin above absolute zero. Subsequent investigations of very pure mercury at low temperatures revealed an unexpected sudden drop in resistivity at 4.2 K to a value below the limit of instrument sensitivity [1]. A new state of matter was confirmed: Superconductivity. The dissipation-less charge transport, however, is only realized at sufficiently low temperatures and below some critical magnetic field. Twenty years later, W. Meissner and R. Ochsenfeld found that superconductors are not only ideal conductors, but also show perfect diamagnetism, *i.e.* they completely expel magnetic fields from the bulk [2]. It was not until 1957 that J. Bardeen, L.N. Cooper, and J.R. Schrieffer provided a microscopic description of superconductivity, the BCS theory [3], the essence of which is that electrons form pairs due to a weak net attraction.

Despite intense effort to synthesize compounds with a high transition temperature T_c, superconductivity remains a low-temperature phenomenon. In 1973, more than half a century after the discovery of superconductivity, a transition temperature of 23 K was found in Nb_3Ge. This record temperature was not superseded until 1986, when high-temperature superconductivity in the copper-oxide system Ba-La-Cu-O was found by J.G. Bednorz and K.A. Müller [4]. The collective name, cuprates, refers to the CuO_2 planes common to them. When the news of superconductivity in cuprates at the unexpected high temperature of 35 K spread around the world, a new field of research emerged, which has remained vigorously active since then. Within a few years, work on the cuprate systems resulted in transition temperatures as high as $T_c = 138$ K [5,6]. This development in itself emphasizes the importance of the discovery in 1986. Not only do the layered copper oxides show exotic superconductivity, they also host a large variety of solid-state phenomena, as illustrated, *e.g.* by the phase diagram (Fig. 1), which seems to be generic for cuprate superconductors. It is this complexity that hampers the progress in understanding the physics behind the exciting properties of the cuprates.

One of the systems in which high-temperature superconductivity was first detected was $La_{2-x}Sr_xCuO_4$ (LSCO), where x is the doping fraction. The maximum $T_c \approx 40$ K for this compound occurs for $x = 0.15$. Through doping with Sr, electrons are removed from the planes of the insulator parent compound, leaving behind holes that make the material conducting. At sufficiently low temperatures the compound becomes superconducting in a characteristic range of x. Other cuprate families have similar phase diagrams, such as YBCO ($YBa_2Cu_4O_8$ and $YBa_2Cu_3O_{7-\delta}$) and BSCCO ($Bi_2Sr_2Ca_nCu_{n+1}O_{4+2n+\delta}$, where $n + 1$=1, 2, 3 is the number of CuO_2 planes in the crystallographic unit cell and δ the oxygen deficiency). High temperature superconductivity in the cuprates requires doping with charge carriers, either intrinsically or extrinsically, of an antiferromagnetic parent compound. The transition temperature increases with doping, attaining a maximum value for a doping fraction known as optimal doping. In YBCO and BSCCO, doping is controlled through the oxygen deficiency δ or through partial chemical substitution of some specific ions. YBCO exhibits a maximum $T_c \approx 92$ K, and for BSCCO even a $T_c \approx 110$ K was reached. In Fig. 2 the crystal structures of some important cuprate superconductors are shown.

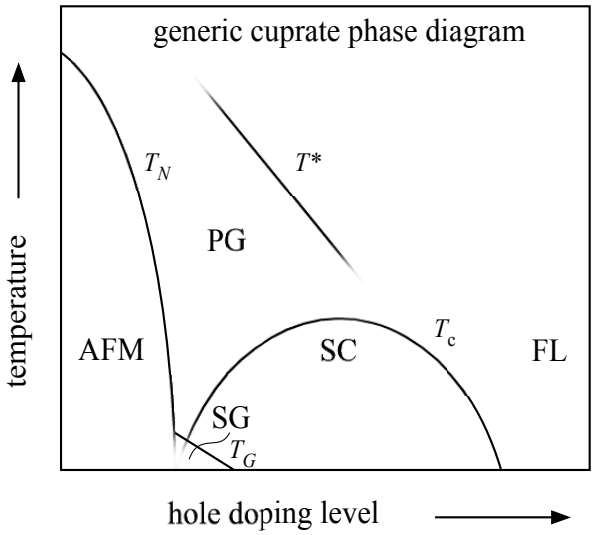

Figure 1: The schematic phase diagram, typical for cuprate superconductors, qualitatively showing the several phases depending on the number of holes per plane-copper atom (doping). The undoped parent compound is an antiferromagnetic (AFM) insulator. With increasing doping, the spin-glass (SG), the superconducting (SC), and the Fermi-liquid-like (FL) phases appear. In addition, the pseudogap (PG) phase is indicated. The corresponding characteristic temperatures for the AFM, SG, SC, and PG phases are T_{N}, T_{SG}, T_{c} and T^*, respectively.

The low energy physics of the quasi two-dimensional planes mentioned before is often simplified into a Hubbard model [7]. With one electron per copper site (half filling), a metal-to-insulator transition is observed. Essentially driven by strong Coulomb repulsion, this transition can be described within the framework of Mott physics. Due to the Coulomb interaction, double occupancy at a copper site is energetically not favorable, which is why the electrons become localized at half band filling. Below the Néel temperature T_{N}, the uncompensated spins of the copper $3d$ electron are arranged in antiferromagnetic order that is rapidly destroyed by only a few percent of hole doping (Fig. 1). For increasing doping, the dome of superconductivity reaches a maximum T_{c} for optimum hole doping. The regions to the left and and to the right of the dome maximum are called underdoped and overdoped respectively. Cuprates are not good metals, since the carrier concentration is about one or two orders of magnitude lower than for typical metals.

Cuprates behave in some respects like conventional superconductors. There is, though, no satisfactory theory for high-temperature superconductivity available at present, since the BCS theory does not comprise all of the physics involved. Meanwhile, photoemission and also de Haas-van Alphen oscillation experiments clearly evidence that cuprates possess a well-defined Fermi surface, at which a superconducting energy gap opens in the excitation spectrum. This gap, however, has a more complex nature compared with

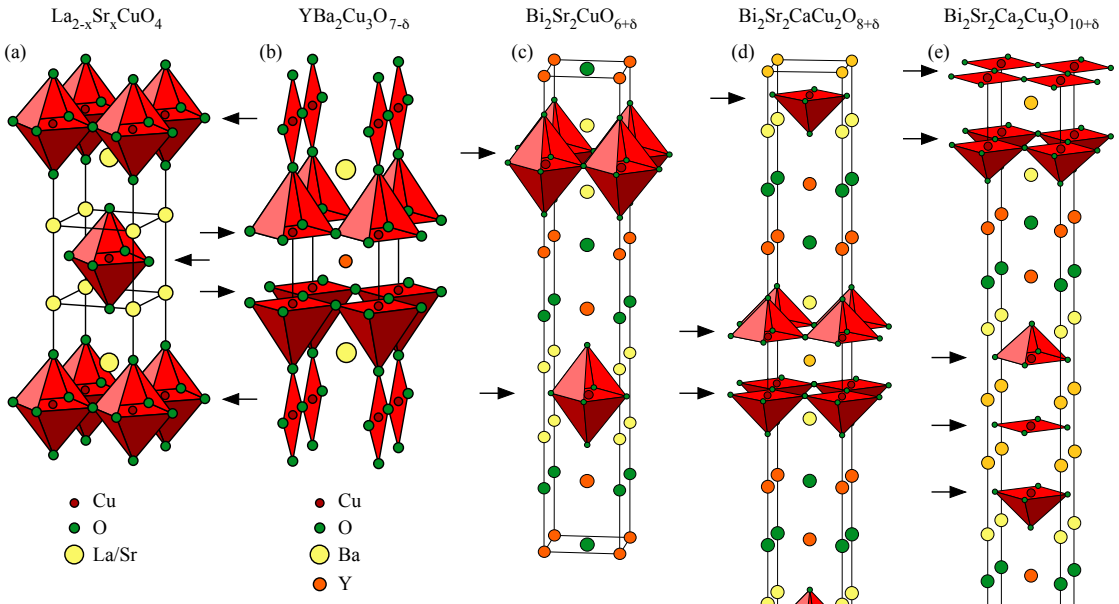

	T_c @ opt. doping
(a) LSCO	~ 40K
(b) YBCO	~ 92K
(c) Bi2201	~ 35K
(d) Bi2212	~ 93K
(e) Bi2223	~ 110K

Figure 2: Crystal structure of several cuprate families. Panel (a) shows the crystal structure of single-layer $La_{2-x}Sr_xCuO_4$ (LSCO), which exhibits a maximum $T_c \approx 40\,K$. (b) presents the double-layer $YBa_2Cu_3O_{7-\delta}$ having a $T_c \approx 91\,K$ at optimum doping. (c), (d), and (e) show the single-, double-, and tri-layer Bi-based cuprate superconductor with maximum $T_c \approx 35, 93, 110\,K$, respectively. The arrows indicate the CuO_2 planes.

the conventional superconductors. In addition, it has to be emphasized that in many cuprates a gap occurs at low doping levels even at elevated temperatures, sometimes far above T_c. This anomalous electronic feature is referred to as the pseudogap. The superconducting gap and the pseudogap, and their mutual relation, are under intense debate at the time of writing.

Although the physics responsible for high-temperature superconductivity is not yet well understood, the induced formation of hole pairs is evident from tunneling experiments. Using nuclear magnetic resonance (NMR), the spin susceptibility was found to decrease in the superconducting phase, which shows that the carriers condense in pair singlet states. For a sufficiently strong external magnetic field, vortices penetrate the bulk material as in conventional type-II superconductors. The magnetic field necessary to quench superconductivity, the upper critical field, is comparatively high, though. As for the very short coherence length, a measure of the spatial pair extension, cuprate superconductors are highly unconventional and show enhanced fluctuation effects. Furthermore, the cuprates show a much stronger anisotropy for basic superconductor properties than conventional superconductors do.

It is widely accepted that superconductivity mainly takes place in the CuO_2 planes. Depending on the actual composition, the cuprate unit cell contains a different number of planes (Fig. 2). The strong anisotropy of the cuprates manifests itself *e.g.* in the electronic transport properties, for which the in-plane conductivity is several orders of magnitude higher than perpendicular to the planes. This obvious two-dimensionality leads naturally to theoretical explanations focusing on the CuO_2 planes only. Still, the third dimension must not be neglected, since purely two-dimensional models do not accommodate all the physics necessary to explain many observed features, in particular not the high transition temperature T_c.

In conventional superconductors, the pairing of carriers is mediated through phonons. As of writing, the pairing mechanism in the cuprates is not well understood, in spite of the huge efforts undertaken, which illustrates again the highly complex physics involved. The defining property of a superconductor is the superconducting energy gap that opens at the Fermi surface. This gap can be investigated experimentally with several different techniques. Muon-spin rotation (μSR) experiments performed in external magnetic fields yield unambiguous information about bulk properties, *e.g.* the internal magnetic field distribution in the vortex state, thus allowing conclusions about the size and symmetry of the superconducting gap. A commercial physical property measurement system (PPMS) with an AC susceptibility insert, provides a convenient instrument for measuring the superconducting energy gap and resolving subtle isotope effects.

The metallic state in the underdoped regime shows exceptional properties, in the pseudogap phase above T_c, which presently are under intense study. The pseudogap is a partial gap that, like the superconducting energy gap, also affects the spectral weight close to the Fermi energy. Evidence for the pseudogap formation has been found in many experiments using different techniques, including NMR [8], tunneling microscopy [9], angle resolved photoemission spectroscopy (ARPES) [10], resistivity [11] and specific heat [12] measurements, and neutron crystal-field spectroscopy [13]. Much effort has been devoted to the investigation of the controversial connection between the superconducting phase and the pseudogap phase. Despite the large body of experimental data, though, a comprehensive understanding of the relation between these two phenomena is still missing. While ARPES offers a detailed picture of the pseudogap, see *e.g.* [14], it was NMR [8] and magnetic susceptibility experiments [15] that provided earliest indication of a normal-state gap. NMR enables investigation of the microscopic magnetic character of the copper oxides and does neither require big samples nor meticulously prepared surfaces. For nuclei with a quadrupole moment, also charge effects can be investigated. The power of NMR mainly comes from its highly local nature, allowing the influence of the surroundings on distinct atomic species to be studied, even with respect to their crystallographic site. NMR is therefore particularly useful for testing microscopic models proposed to explain the physics of cuprates.

Following this, we describe our NMR investigation of magnetism from so-called orbital currents, predicted by microscopic theories for the pseudogap phase. Our study results impose constraints on the orbital-current models. In addition, an NMR investigation of charge inhomogeneities in cuprates and their possible relation to the anomalous gap is presented, and qualitative evidence for charge effects from relaxation studies given. Moreover, the relevance of the pseudogap for the occurrence of superconductivity is ad-

dressed on the basis of μSR data. A comparison of our data with theoretical calculations based on ARPES results, suggests that the pseudogap and superconductivity are coexisting phases.

The latter part of this Thesis deals with fundamental properties of superconductivity. We present our investigations of lattice effects and superconductivity in the cuprates from investigations of the oxygen-isotope effect for the superconducting energy gap by means of AC susceptibility measurements. A novel oxygen-isotope effect was found, which scales linearly with the isotope effect for the transition temperature T_c. Finally, we discuss the multi-gap superconductivity in cuprate superconductors and present our related μSR results.

2 The energy gap of the pseudogap phase

In this chapter our work concerning the pseudo energy gap (pseudogap) using nuclear magnetic resonance and muon-spin rotation techniques is described.

The physics behind the pairing of charge carriers responsible for high-temperature superconductivity is presently not well understood. Magnetism is assumed to be crucial for the mutual binding of charge carriers. In a simplified picture, a charge carrier jumps from one copper site to the next in the copper-oxygen plane, thereby disturbing the antiferromagnetic order of the copper atomic spins. A second charge carrier contributes to restore the energetically favorable spin order and thus prevents spin frustration. Similar to the phonon-mediated interaction between carriers, the two carriers experience a net attraction, forming a bound state that eventually leads to superconductivity. The magnetic interaction is not discussed in detail here, since this would take us beyond the scope of this work. The reader is referred to the literature, *e.g.* [16]. Instead, we concentrate here on the so-called pseudogap phase.

Several theoretical models describe the pseudogap in terms of the orbital-current phase, which is a direct consequence of the Hubbard model. As indicated already by its name, the pseudogap is a peculiar phenomenon, observed in underdoped cuprate high-temperature superconductors but not encountered in common metals. It manifests itself as a partial gap in the electronic density of states at the Fermi surface, appearing in the normal conducting phase below a certain crossover temperature T^*. NMR work early on provided evidence for the pseudogap. Curro *et al.* measured the Knight shift ${}^{63}K$ of the copper nuclear spin in the CuO_2 plane of $YBa_2Cu_4O_8$ [18], finding a nearly temperature independent shift above 300 K and an onset of a decrease below. At ~ 80 K, the onset temperature for superconductivity in this compound, a loss of 80% of the room-temperature spin susceptibility was observed. Later NMR measurements on the similar $YBa_2Cu_3O_{6+x}$ by Alloul *et al.* showed that the characteristic temperature T^* depends on doping [19], and various other experiments confirmed their findings (see, *e.g.* [20–22]).

For sufficiently underdoped cuprates the pseudogap is much larger than the superconducting gap, gradually decreasing with increasing doping until it finally merges with the superconducting gap somewhere in the overdoped regime. Several techniques for probing the Fermi surface provide information about this exotic electronic property. In fact, the pseudogap is not only found in the cuprates, but the newly discovered pnictides also show properties which may be related to a pseudogap (see, *e.g.* [23, 24]). Using ARPES, a dependence of the pseudogap on the wave vector k was evidenced [14,25]. It was shown that the pseudogap develops gradually toward a maximum value in the anti-nodal region of the Fermi arc, *i.e.* along the copper-oxygen bonds in the plane, whereas it vanishes near the diagonal of the Cu-O bonds, *i.e.* the nodal direction.

In the pseudogap phase ($T^* > T > T_c$), a temperature independent anti-nodal gap with an entirely gapless Fermi arc in the near-nodal region appears. In contrast, the superconducting gap ($T < T_c$) has point nodes only (along the diagonal of the planar Cu-O bond) and shows a temperature dependent near-nodal gap [25].

Even two decades after the discovery of the pseudogap, its properties remain elusive. It has not yet been finally resolved for instance, whether a one-particle or a two-particle

interaction is responsible. Further, it is also not clear, whether an order parameter characterizes this phase. It therefore remains a key issue to clarify the interplay between the superconducting and the pseudogap phases.

Two main pseudogap scenarios have been suggested, see *e.g.* [26, 27] and references therein. In a so-called precursor scenario the pseudogap is assumed to evolve to become the superconducting gap as the temperature is lowered across T_c. Cooper pairs, preformed in the range $T^* > T > T_c$, gain long-range phase coherence below T_c and form the superconducting condensate. In other words, the pseudogap is the incoherent continuation of the superconducting gap above T_c, see *e.g.* [28, 29]. In a contrasting view, the pseudogap and the superconducting state are two distinct coexisting phases that even may compete. The latter is therefore known as the "competing" scenario. Quite a number of experiments indicate the existence of two independent phenomena, see *e.g.* [14, 20, 25, 30, 31], but the debate is still ongoing.

The concept of orbital currents was recently proposed in order to explain the properties of the pseudogap in a precursor scenario. Several specific current patterns have been suggested, all of which break time-reversal symmetry, but only a few translational symmetry. The distinguishing characteristic of any orbital-current pattern is the induced magnetic field signature. So far the magnetic moments associated with orbital currents were explored using neutron scattering and muon-spin rotation. Recent neutron scattering studies claim evidence for magnetism compatible with one of the proposed current patterns appearing below T^* in underdoped cuprates. Commensurate magnetic peaks for $T < T^*$ were reported for $YBa_2Cu_3O_{6+x}$ [32, 33] and $HgBa_2CuO_{4+\delta}$ [34]. Based on muon-spin rotation experiments, an upper limit for static, time-reversal breaking fields of 0.02 mT was reported [35]. It was pointed out [36], however, that the local fields may become reduced by screening due to the charge of the implanted muon.

In this work we add NMR to the list of methods by which the orbital-current state was investigated. NMR is a microscopic tool, sensitive to fluctuating as well as static internal magnetic fields. A major advantage of NMR is that the nuclear moments of the atoms act as probes, eliminating the need for introducing anything potentially disturbing. Fortunately, in the case of the cuprates all the important sites of the structure are amenable to NMR. Moreover, different sites of the same atomic species can be investigated separately since the electric field gradient and the local magnetic fields determine site-specific NMR parameters and their dependence on temperature and magnetic field. The interaction between the excited nuclei and their surroundings provides valuable information about the electronic system. We applied NMR in the search for the magnetic field arrangement produced by possible orbital currents, but no evidence was found. Instead, we provide upper limits for additional static and fluctuating fields, which constitute significant constraints on theoretical predictions.

Another open question is the relevance of stripes, or more generally, charge inhomogeneities in high-temperature superconductivity, see *e.g.* [37]. Nuclei with electric quadrupole moments, such as copper and oxygen, are directly sensitive to charge effects. Stripe formation is expected in the copper-oxygen planes, since the mobile charge carriers are believed to be mainly confined within the plane [38]. Very likely, charge inhomogeneity, like stripes, are dynamic and fluctuate, at least at elevated temperatures, at almost electronic frequencies. In order to search for possible charge effects, it

is worthwhile to investigate the temperature behavior of various NMR parameters, and to probe static and dynamic charge processes. As doping increases toward optimum, the long-range antiferromagnetism is rapidly destroyed. Short-range antiferromagnetic correlation between the copper atomic spins, however, persist. The nuclear spin-lattice relaxation of the copper nuclei in the CuO_2 plane is dominated by the strong fluctuations of the antiferromagnetically arranged copper atomic spins, whence the relaxation exhibits a predominant magnetic character. The nuclear spins of the oxygen atoms in the plane also relax mainly because of these fluctuations, although they cancel to a large extent for symmetry reasons. At low temperatures ($\sim 1\,\mathrm{K}$), however, a distinct spin-lattice relaxation rate maximum of quadrupolar nature has been detected for the copper nuclei [39]. Around 100 K the oxygen nuclei also show a small quadrupolar contribution to the spin-lattice relaxation [40], which may be related to the copper relaxation rate maximum.

We investigated charge effects by introducing a charge sensitive nucleus at the Y-site of YBCO, which is located between the copper-oxygen planes. A promising candidate was found in ^{139}La for which NMR and NQR signals in $LaBa_2Cu_3O_{7-\delta}$ were successfully detected, and the nuclear relaxation mechanisms studied.

Later in this chapter, we discuss the relevance of pseudogap formation for high-temperature superconductivity while considering muon-spin rotation experiments. A comparison of model calculations, using results of photoemission experiments, with μSR data suggests that in optimally doped $(BiPb)_2(SrLa)_2CuO_{6+\delta}$ the pseudogap phase and the superconducting phase are dominated by different parts of the Fermi surface. This finding indicates that the pseudogap state and the superconducting state constitute distinct coexisting properties of the electronic system.

2.1 NMR and NQR search for the orbital-current phase

2.1.1 Concept of nuclear magnetic resonance

Solid-state NMR offers the unique possibility of probing different nuclear species and atomic sites selectively. Nuclei with non-zero spin angular momentum $\hbar I$ possess magnetic dipole moments $\mu = \gamma\hbar\mathbf{I}$ that induce nuclear magnetism. Here γ denotes the gyromagnetic coupling constant. In fact, the weak coupling between the small moments reduces any observable magnetism to nuclear paramagnetism. The local magnetic field lifts the degeneracy the energy levels, which are populated according to the Boltzmann distribution (*i.e.* proportional to $\exp(-E_m/kT) = \exp(\gamma\hbar m B_0/kT)$, $m = -I$ to I). The net magnetization resulting from an external magnetic field $\mathbf{B_0}$ or an internal local magnetic field is essentially what we assess in NMR experiments. In absence of nuclear quadrupole moments, all $\Delta m = 1$ transitions between the equidistantly distributed energy levels are excited simultaneously through irradiation of the sample with radio-frequency pulses providing the energy required. For nuclei with a (not too strong) electrical quadrupole moment Q (*i.e.* $I > \frac{1}{2}$), the spectrum splits into a central and two or more satellite lines (Fig. 3) that may be investigated separately. In the following, the nuclear spin Hamiltonian, the magnetic shift, and the relaxation behavior of nuclear spins will be briefly described.

Hamiltonian

A nucleus interacts with its environment through its magnetic moment and its electric quadrupole moment. The Hamiltonian for the interactions of a nucleus with spin $\mathbf{I}$ and quadrupole moment Q in the presence of a static magnetic field $\mathbf{B_0}$ and an electric field gradient is given by the sum of a Zeeman part H_Z and a quadrupole part H_Q

$$H_0 = H_\mathrm{Z} + H_\mathrm{Q}, \tag{1}$$

where

$$H_\mathrm{Z} = -\hbar\gamma_n \mathbf{I}(1 + \mathbf{K}^\mathrm{tot})\mathbf{B_0} \tag{2}$$

and

$$H_\mathrm{Q} = \frac{eQV_{zz}}{4I(2I-1)}\left[3I_z^2 - \mathbf{I}^2 + \frac{\eta}{2}(I_+^2 + I_-^2)\right]. \tag{3}$$

Here γ_n denotes the nuclear gyromagnetic ratio, $\mathbf{K}^\mathrm{tot}$ the magnetic shift tensor, Q the nuclear quadrupole moment of the nucleus, V_{ii} the principal components of the electric field gradient at the nuclear site, and $\eta = (V_{xx} - V_{yy})/V_{zz}$, $0 \le \eta \le 1$, the asymmetry parameter. We use the convention $|V_{xx}| \le |V_{yy}| \le |V_{zz}|$. Figure 3 shows, as an example, a typical NMR spectrum for $I = 3/2$. On the left side of the term diagram a pure Zeeman interaction is depicted. For non-vanishing Q and a crystal symmetry lower than cubic, a quadrupole interaction has to be present; a pure quadrupole interaction is shown on the right side of Fig. 3. In the central part of the figure the two interactions are shown for the case of simultaneous presence.

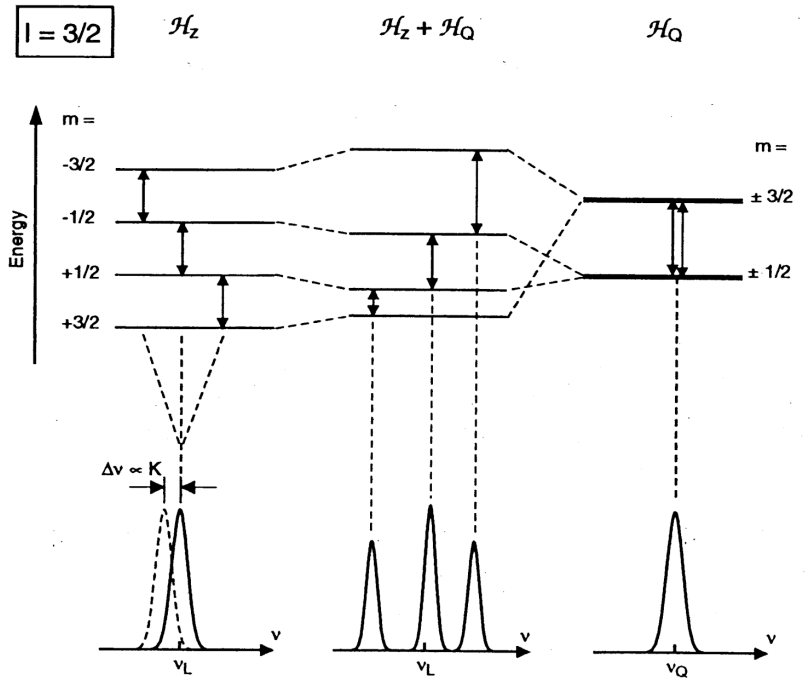

Figure 3: Typical nuclear energy level diagram for $I = 3/2$ in the presence of a magnetic field alone (on the left), in the presence of a magnetic field and an electric field gradient (in the middle), and in the presence of only an electric field gradient (on the right).

Magnetic shift

The magnetic coupling between the nuclear spin $\mathbf{I}$ and its electronic environment can be viewed as a coupling between the nuclear magnetic moment $\hbar\gamma_n\mathbf{I}$ with a (time dependent) hyperfine field generated locally at the site of the nucleus of species n, and the spin and the angular momentum of the conduction electrons. The static part of the hyperfine interaction leads to a shift of the Larmor frequency ${}^n\omega_{\mathrm{L}} = \gamma_n\mathbf{B_0}$. This magnetic shift may be anisotropic and is conveniently described by the magnetic shift tensor ${}^n\mathbf{K}$, which may be decomposed into a spin, an orbital, and a diamagnetic part

$$ {}^n\mathbf{K}_{\alpha\alpha} = {}^n\mathbf{K}^{\mathrm{spin}}_{\alpha\alpha} + {}^n\mathbf{K}^{\mathrm{orb}}_{\alpha\alpha} + {}^n\mathbf{K}^{\mathrm{dia}}_{\alpha\alpha}. \tag{4} $$

Here α stands for any of the three principal directions x, y, or z. In the literature ${}^n\mathbf{K}^{\mathrm{spin}}$ is known as the Knight shift, which originates from the interaction of the nuclear spin with the spins of delocalized and localized charge carriers. For a BCS superconductor, the Knight shift is constant in the normal conducting state. Below the critical temperature T_{c}, the spin shift decreases since the spins condense as spin-singlet pairs. ${}^n\mathbf{K}^{\mathrm{orb}}$ denotes the typically temperature independent orbital shift, which derives from the coupling of $\hbar\gamma_n\mathbf{I}$ and the electronic orbital moment. Finally, ${}^n\mathbf{K}^{\mathrm{dia}}$ is caused by diamagnetic effects. Note that one cannot easily monitor the variation of the spin shift across T_{c} because of the temperature dependent diamagnetic shielding in the superconducting state.

Considering separately the hyperfine interaction tensor and the static electronic spin susceptibility $\chi_{\alpha\alpha}$ (*i.e.* at zero wave vector and zero frequency), the following expressions

can be derived for the first two components of the magnetic shift tensor ${}^n\mathbf{K}_{\alpha\alpha}$:

$$ {}^n\mathbf{K}^{\text{spin}}_{\alpha\alpha} = \frac{1}{g\,\mu_B}\sum_j ({}^nA_j)_{\alpha\alpha}\,(\chi_j)_{\alpha\alpha}, \tag{5} $$

$$ {}^n\mathbf{K}^{\text{orb}}_{\alpha\alpha} = \frac{1}{\mu_{\text{B}}}{}^nO_{\alpha\alpha}\,\chi^{\text{orb}}_{\alpha\alpha}, \tag{6} $$

where g refers to the Landé factor and μ_{B} is the Bohr magneton. The Knight shift thus conveys information about both the static spin susceptibility and the hyperfine interactions.

Spin-lattice relaxation

Following a perturbation, the nuclear spin ensemble relaxes toward equilibrium with the lattice, *i.e.* its surrounding. The time constant T_1, characterizing the thermalization process, is known as the spin-lattice relaxation time. For nuclei, spontaneous emission of radio frequency is negligible within the NMR time window. Fluctuating magnetic fields and/or a fluctuating electric field gradient, however, couple the spin system to its surroundings, enabling nuclear spin-energy transfer to the lattice. Nearly all relevant mechanisms for spin-lattice relaxation in cuprates are based on electron-nucleus interactions. In general, the relaxations of Cu, O, and Y nuclei are well described by the Moriya formula [41, 42], which can be written as [43]

$$ {}^n(\frac{1}{T_1})_\alpha = \frac{\gamma_n^2\,k_{\text{B}}\,T}{2\mu_{\text{B}}^2}\sum_{\mathbf{q},\alpha\neq\alpha'} |{}^nA_{\alpha'\alpha'}(\mathbf{q})|^2\,\frac{\chi''_{\alpha'\alpha'}(\mathbf{q},{}^n\omega_{\text{L}}),T}{{}^n\omega_{\text{L}}} \tag{7} $$

$$ {}^nA_{\alpha\alpha}(\mathbf{q}) = \sum_j ({}^nA_j)_{\alpha\alpha}\,\exp(i\mathbf{q}\cdot\mathbf{r}_j). \tag{8} $$

Here α denotes the direction of the quantization axis, for NMR defined by the external magnetic field $\mathbf{B_0}$. For NQR, however, α denotes the direction along the major principal component V_{zz} of the electric field gradient and α' the direction perpendicular to α. χ'' denotes the imaginary part of the complex electron susceptibility, which depends on wave vector and energy. The hyperfine coupling tensors ${}^nA_j$ refer either to the on-site ($\mathbf{r}_j = 0$) or the transferred interaction ($\mathbf{r}_j \neq 0$). As may be seen from Eq. (7), measurements of the relaxation rate provide information about the average of the wave vector dependent imaginary spin susceptibility χ'', which may also be determined in neutron scattering experiments. The susceptibility shows a distinct peak for the antiferromagnetic wave vector $q_{\text{AF}} = (\pi/a, \pi/a)$ [44–49], where a denotes the lattice constant.

For most simple metals, the spin-lattice relaxation rate divided by temperature, $1/(T_1T)$, is proportional to the square of the density of states at the Fermi level [50]. The rate is related to the Knight shift through the Korringa relation

$$ \frac{1}{{}^nT_1T} = \frac{4\pi k_{\text{B}}}{\hbar}\left(\frac{\gamma_n}{\gamma_e}\right)^2 K^2. \tag{9} $$

The technique widely used for measuring the spin-lattice relaxation time is briefly described in the following. The sample resides in a coil oriented transversely to the quantization axis. Spin echoes are produced with radio-frequency (rf) pulse sequences feeding

the coil at chosen repetition rate. The leading rf pulse of the sequence inverts the nuclear magnetization that is assumed to be in equilibrium along the quantization axis[1], after which the spin system gradually recovers. In order to probe the state of the spin recovering system after a wait time t_w, the remaining magnetization parallel to the quantization axis is rotated by a second rf pulse of defined duration, thus producing a nuclear magnetization precessing in a plane perpendicular to the quantization axis, as the spins gradually dephase. After a delay time τ a refocusing pulse rotates the spin system trough 180° such that a spin echo appears after another time τ. The time constant T_1 is obtained from the decay of the spin-echo intensity with t_w. Generally, noise-averaging techniques have to be applied in order to achieve the necessary statistics. In addition, elaborate pulse sequence schemes are applied that suppress background noise by changing the phase of the pulses in a certain pattern.

Spin-spin relaxation

The spin-spin relaxation time T_2, also known as the transverse relaxation time, is a measure of the decay of the transverse nuclear magnetization relative to the quantization axis. In general, there are two ways to determine T_2, either directly from the free induction decay that develops after a short rf pulse, or from spin-echo experiments. Both of these techniques are influenced by homogenous broadening related to local spin-spin interactions, like *e.g.* the direct dipole-dipole interaction. The NMR/NQR spectrum is also affected by inhomogeneous broadening from field inhomogeneity or structural disorder, making the free induction decay difficult to observe. The spin-echo pulse sequence experiment, in contrast, does not necessarily suffer from these influences, and is thus often the preferred choice of method.

A typical spin-echo pulse sequence used for measuring the spin-spin relaxation is composed as follows: A leading rf pulse rotates the nuclear magnetization from its equilibrium position along the quantization axis, through an angle 90° into the plane perpendicular to the reference direction. This produces a precessing transverse magnetization from spins that gradually loose coherence as they dephase. After a delay τ, a second rf pulse causes the spins to refocus, such that an echo appears at time 2τ after the first pulse. T_2 is extracted from the decay of the spin-echo intensity with pulse spacing τ.

The time evolution of the spin-echo amplitude A can be expressed as:

$$A(2\tau) = A_0 \exp\left[-\frac{2\tau}{T_{2\mathrm{R}}} - \frac{1}{2}\left(\frac{2\tau}{T_{2\mathrm{G}}}\right)^2\right], \tag{10}$$

where $T_{2\mathrm{R}}$ is the Redfield term and $T_{2\mathrm{G}}$ the Gaussian component of the spin-spin relaxation process. The Redfield contribution refers to the decay rate of the echo amplitude due to spin-lattice relaxation [51]. The Gaussian component is caused by the nuclear dipole-dipole interaction, which includes the direct as well as the indirect interactions of the electronic system.

[1]Hence this procedure is named inversion-recovery method. Alternatively, a leading burst of several rf pulses is transmitted to saturate the spin system first (saturation method).

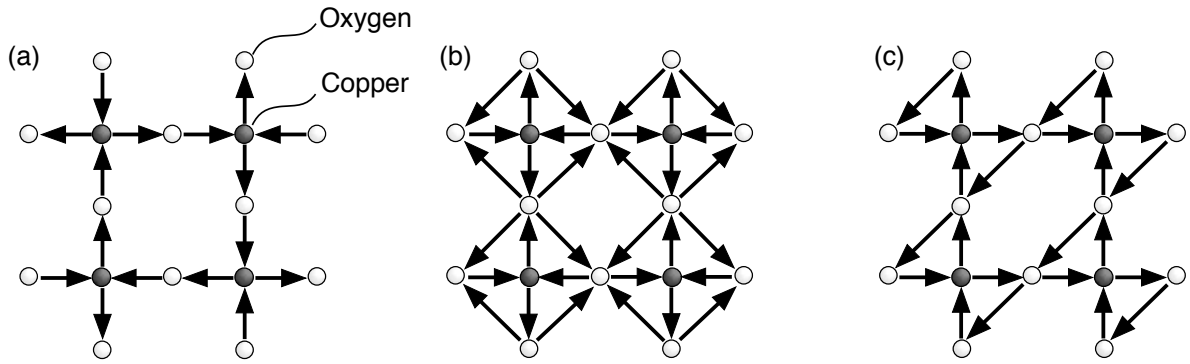

Figure 4: Some orbital-current patterns of circulating currents in the CuO_2 planes of cuprates (arrows indicate the direction of the current). (a) The currents in the d-density wave (DDW) pattern, after [52, 53]. The two circulating-current (CC) patterns are displayed in panels (b) and (c), after [54, 55].

2.1.2 Motivation

A comprehensive microscopic theory for cuprate superconductivity remains an important problem in condensed matter physics. The proposed orbital-current phase for explaining the physics of cuprates, in particular the pseudogap, has attracted much attention in recent years. The most prominent of the suggested orbital-current schemes are the d-density wave (DDW) phase [52, 53] and the circulating current (CC) phase [54, 55] for which some current patterns are depicted in Fig. 4. The amount of experimental data is still small compared to the theoretical efforts. Polarized neutron scattering studies on YBCO [32, 33] and $HgBa_2CuO_{4+\delta}$ [34] report magnetic features developping at a doping dependent temperature that appears to coincide with the pseudogap temperature T^*, determined from resistivity measurements. A Kerr effect study performed on YBCO, evidences breaking of the time-reversal symmetry near T^* [56] but at systematically lower temperatures. No indication of fields violating the time-reversal symmetry could, however, be found in μSR experiments [35]. As previously mentioned, it has been argued that the μSR investigation may be hampered by self-doping effects due to the charge of the muon, which could destroy the ordered state at the stopping site and thus reduce the local fields significantly [36].

NMR is a highly sensitive method suitable for the study of local magnetic fields, providing information about static as well as on fluctuating internal fields. Its ability to test the orbital-current models depends on the current-path and current strength. Static fields arising from the proposed current phases (DDW, CC) cannot be detected by NMR using nuclei of ions located in CuO_2 plane, since for symmetry reasons the fields cancel at these sites. Disregarding possible interplane interactions between the bi-layers of YBCO, the Y-ions are not situated at centers of symmetry for the DDW and the CC phases. As the nuclear spin of ^{89}Y is experimentally accessible through NMR, ^{89}Y NMR experiments should be sensitive to orbital-current effects. In fact, for all proposed current patterns the local fields generated at the Y-site are directed either parallel or perpendicular to the c-axis, also for the exotic proposal involving the apex oxygen (Fig. 5) [57].

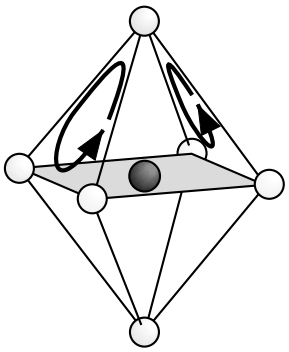

Figure 5: Cuprate oxygen octahedron with the CuO_2 plane indicated by shading and with a copper atom at the center. The arrows indicate the orbital-current path, after [57].

The bi-layer cuprate superconductor $Y_2Ba_4Cu_7O_{15-\delta}$ (Y247) was chosen for our investigation of the orbital-current phase. As Lee and Sha pointed out, the doping difference of neighboring planes rules out full cancellation of the single-plane magnetic fields at the Y-site between the two CuO_2 planes [7]. The Y-nucleus is a good candidate for investigation of magnetic effects in cuprates, since it has no quadrupole moment that would complicate the measurements if charge effects would be present.

2.1.3 Experimental details

Y247 consists of alternating $YBa_2Cu_3O_{7-\delta}$ (Y123) and $YBa_2Cu_4O_8$ (Y124) blocks (Fig. 6). As for the parent compounds, stoichiometric Y124 is inherently underdoped and shows a pronounced pseudogap, whereas Y123 is close to optimum doping, and shows no indication of a pseudogap above T_c. The main structural difference between Y123 and Y124 is that the latter possesses double chains without oxygen vacancies, in contrast to the single-chain Y123. The CuO_2 planes in Y247 form bi-layers separated by Y-ions as in Y124 and Y123. Unlike the parent compounds, as pointed out above, the adjacent planes in Y247 have different doping levels [59], which is a most important feature for our study.

The Y247 sample was prepared by a solid-state reaction technique described in detail elsewhere [58]. A Y247 sample with a phase-impurity level less than 0.5 % by volume was achieved. The sample exhibits a transition temperature $T_c = 95\,\mathrm{K}$ and a pseudogap phase above T_c [59]. Due to the anisotropic magnetic susceptibility, the powder can be oriented in an external static magnetic field. In order to preserve the orientation of the grains, the powder was cured in epoxy in a 9 T field. The sample thus has a high degree of c-axis alignment, allowing a study of the anisotropic properties of the sample. The a-axis and the b-axis of the crystallites remain randomly distributed in a plane perpendicular to the c-axis.

The ^{89}Y NMR experiments were carried out in a 9 T magnet equipped with a flow cryostat. A conventional phase-coherent pulse NMR spectrometer was used for the

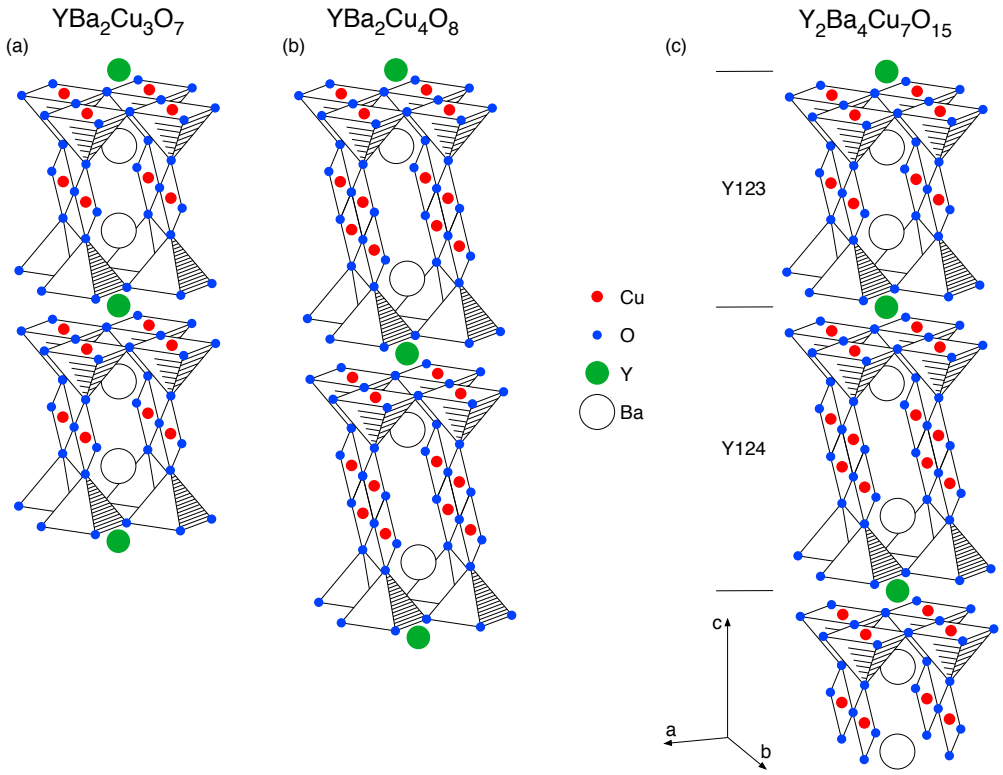

Figure 6: Crystal structure for some important YBCO compounds. (a) $YBa_2Cu_3O_{7-\delta}$ with $\delta = 0$. The doping level is determined by the oxygen deficiency δ, maximum $T_c \approx 93\,\mathrm{K}$. (b) Stoichiometric $YBa_2Cu_4O_8$ with $T_c \approx 82\,\mathrm{K}$. (c) $Y_2Ba_4Cu_7O_{15-\delta}$ consisting of alternating blocks of $YBa_2Cu_3O_7$ and $YBa_2Cu_4O_8$, $T_c \approx 95\,\mathrm{K}$.

measurements. The spin-lattice relaxation time was measured using a saturation-pulse sequence, and a phase alternating spin-echo accumulation technique. The NMR line width was obtained by complex Fourier transformation of the spin echo signal.

2.1.4 Results and Discussion

The magnetic signature discovered in neutron scattering data [33] for the normal conducting regime of cuprate superconductors, and found to be consistent with the current pattern displayed in Fig. 4c, appears to be static on the neutron scattering interaction time scale (10^{-11} s). The NMR time scale (temporal resolution) is three to four orders of magnitude slower, whence it has not been established whether static or fluctuating fields persist in a possible orbital-current state. In our analysis we therefore considered an entire range of correlation times, from static fields to fields fluctuating on the time scale of neutron scattering interactions.

Any additional static field at the site of a nuclear spin directed along the external field shifts the NMR frequency. Therefore, if orbital currents would appear as the temperature is lowered, the additional magnetic field shifts the frequency position in proportion. Due to the nature of the DDW current pattern (neighboring currents flow in opposite directions), not a shift of the ^{89}Y NMR line, but rather a splitting would be expected, which may be unresolved and may only appear as a broadening of the line.

In the case of a static CC pattern, the corresponding fields at the Y-sites would be directed perpendicular to the c-axis and originate from currents in correlated domains of given extension. Since we investigate an oriented powder sample for which the a- and b-axis are randomly distributed, a broadening and not a shift or a splitting of the ^{89}Y NMR line is expected.

Any such additional orbital-current fields at the Y-sites must directed either parallel or perpendicular to the c-axis. The frequency position of the NMR line is influenced only by small static fields parallel to the external field. Any additional local magnetic field perpendicular to the large external field can be neglected because of the difference in strength by orders of magnitude. Consequently, the anisotropy of the NMR line width must change if orbital currents appear.

It is believed that the current pattern stabilizes in the pseudogap phase at a temperature well below room temperature but still above T_c. We measured the normal state temperature dependence of the ^{89}Y NMR line width for two perpendicular field orientations: The external field either parallel to the c-axis or to the CuO_2 planes. Results for the full ^{89}Y line width at half height are presented in the inset of Fig. 7d. Examples of NMR lines measured for the two field orientations are shown in Fig. 7, panels (a) and (b), both showing characteristic asymmetric line shapes. This asymmetry of the lines originates in the doping inhomogeneity caused by the clustering of oxygen in the chain structure of the Y123 block of the Y247 structure. This may be qualitatively understood as follows: Since the frequency shift of the NMR intensity strongly depends on the local charge carrier density, which in turn depends on the local doping, the resulting NMR intensity reflects a local distribution of oxygen disorder. The local doping, though, cannot exceed the maximum possible doping determined by the fully oxygenated Y1237 structure, which has filled chains and is inherently slightly overdoped. Substantial un-

derdoping, however, is possible, from which follows that the doping distribution must be asymmetric, just as the concomitant charge density becoming evident in the observed line asymmetry.

In order to minimize the disturbing influence of doping inhomogeneity, we used the leading-edge line width (LEW) for evaluation of the symmetric orbital-current broadening effect discussed above. The temperature dependence of the LEW was measured for both field orientations and plotted in Fig. 7d. At high temperatures, the LEW for Y247 agrees within error bars with Y124 data. While cooling from 310 K to 100 K, the LEW increased for both field orientations by ~ 150 Hz compared with the high-temperature value of ~ 250 Hz. Taking conservatively this increase as being entirely caused by orbital currents, we finally arrive at a maximum estimated field amplitude at the Y-site in Y247 of $[\{(400\,\mathrm{Hz})^2 - (250\,\mathrm{Hz})^2\}/{}^{89}\gamma_n^2]^{\frac{1}{2}} \approx 0.15$ mT. This value was deduced, assuming, again conservatively, that the different effects contributing to the LEW add quadratically. Note that the temperature dependent line width increases for both field directions. We also determined the temperature dependence of the magnetic shift of the Y-line for both field directions. The results are shown in Fig. 7c. The decrease of the magnetic shift corresponds to the change in the density of states at the Fermi level and clearly evidences the presence of a pseudogap.

The bi-layer structure of Y247 may cause a reduction of the possible orbital-current fields at the Y-site, but only if there is an antiferromagnetic interplane interaction between the fields of the orbital currents of adjacent planes. In order to estimate a reliable maximum orbital-current field strength from a single CuO_2 plane only, we include in our analysis the possibility of cancellation and assume anti-phase circulation of orbital currents in neighboring planes. The carrier density in neighboring planes of Y247 differs by about $\sim 20\%$ [59]. The orbital-current strength is inversely proportional to the doping level [54, 60] and the field is expected to be proportional to the current strength. Opposite circulation of orbital currents in neighboring planes therefore increases our single layer field limit at the Y-site in Y247 by a factor of ~ 5 (~ 0.75 mT). Unless the actual current pattern is different from any of those proposed, a line-width broadening due to orbital currents is expected only for one of the field orientations investigated, which was found not to be the case. This suggests that our static orbital-current field strength limit is rather overestimated.

Fluctuating magnetic fields at the Y-site in Y247 were investigated in order to estimate the maximum fluctuating field amplitude that could be ascribed to orbital currents. The spin-lattice relaxation is sensitive to dynamic effects, since magnetic fields fluctuating perpendicular to the quantization axis influence the relaxation mechanism. The anisotropy of the spin-lattice relaxation rates is defined as $R = {}^{89}T_1^{\parallel}/{}^{89}T_1^{\perp}$, where ${}^{89}T_1^{\parallel}$ (${}^{89}T_1^{\perp}$) denotes the relaxation time for $\mathbf{B_0}$ parallel (perpendicular) to the c-axis. Fluctuating orbital currents give rise to magnetic fields that fluctuate either parallel or perpendicular to the c-axis. Thus R is expected to change for any non-static orbital current pattern appearing. We measured the temperature dependence of the ^{89}Y spin-lattice relaxation rate in the normal conducting phase up to room temperature for both field orientations. Results are shown in Fig. 8. The inset indicates the data quality for a measurement of the decaying normalized magnetization at 98 K. The relaxation of the normalized nuclear magnetization shows the expected single-exponential behavior.

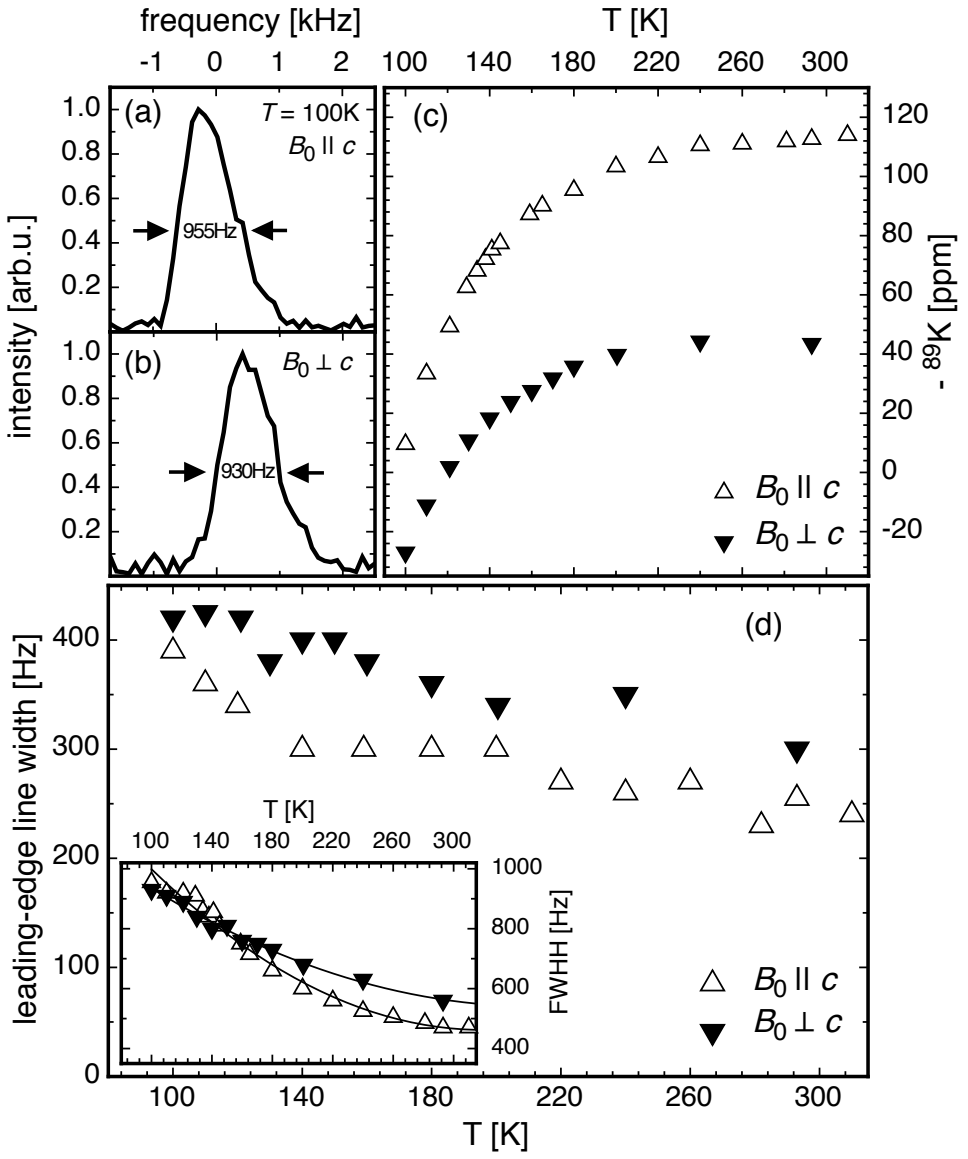

Figure 7: ^{89}Y NMR data from $Y_2Ba_4Cu_7O_{15}$ measured with $B_0 = 9\,\mathrm{T}$ for field orientations parallel ($\|$) and perpendicular ($\perp$) to the crystalline c-axis. Panels (a) and (b) show typical NMR lines relative to 18.86753 MHz at 100 K for both field orientations with a full width at half height (FWHH) of 955(50) kHz and 930(50) kHz respectively. Panel (c) displays the temperature dependence of the magnetic shift. In (d) the temperature dependence of the leading edge ^{89}Y NMR line width at half height (LEW) is shown. The insert shows the temperature dependence of the FWHH (solid lines are guides to the eye). After Paper **I** (Sec. 2.1.6).

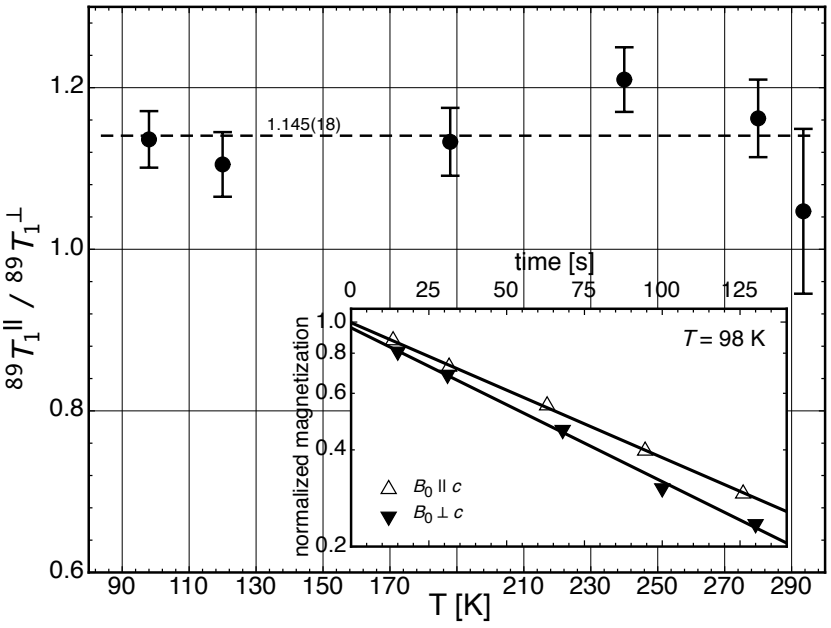

Figure 8: Temperature dependence of the ^{89}Y spin-lattice relaxation rate anisotropy measured in an oriented powder sample of $Y_2Ba_4Cu_7O_{15}$ for $B_0 = 9\,\mathrm{T}$. The dashed black line represents the weighted average $\bar{R} = 1.145(18)$. The inset shows the single-exponential decay of the normalized magnetization for both field orientations ($\mathbf{B_0} \parallel$ and $\perp c$) at 98 K, including the fits with corresponding values $^{89}T_1^{\parallel} = 103.4(2.0)\,\mathrm{s}$ and $^{89}T_1^{\perp} = 91.0(2.5)\,\mathrm{s}$.

The measured relaxation rate can be decomposed according to $1/^{89}T_1 = 1/^{89}T_1^{\mathrm{orb}} + 1/^{89}T_1'$, where the first term arises from possible orbital currents and the second contains all other relaxation mechanisms. The rate anisotropy R was found to be constant within error, having a weighted average $\bar{R} = 1.145(18)$, from which we conclude that the maximum contribution from orbital currents at the lowest temperature measured does not exceed 3%. In order to calculate the fluctuating field amplitude ΔB_{orb} due to orbital currents, we used the expression [51]

$$\frac{1}{^{89}T_1^{\mathrm{orb}}} \approx \overline{{}^{89}\gamma_n^2 \Delta B_{\mathrm{orb}}^2} \cdot \frac{\tau_{\mathrm{c}}}{1 + (\omega_{\mathrm{L}}\tau_{\mathrm{c}})^2}, \tag{11}$$

which relates the correlation time τ_{c}, associated with any fluctuating orbital currents, to the spin-lattice relaxation rate. Using the previously deduced maximum additional contribution of 3% to the spin-lattice relaxation rate due to possible orbital currents and

$$\Delta B_{\mathrm{orb}} = [(1 + (\omega_{\mathrm{L}}\tau_{\mathrm{c}})^2)/({}^{89}\gamma_n{}^2 \cdot T_1^{\mathrm{orb}} \cdot \tau_{\mathrm{c}})]^{\frac{1}{2}} \tag{12}$$

from Eq. (11), we may plot ΔB_{orb} versus τ_{c} (see solid line in Fig. 9). In order to estimate an upper limit for ΔB_{orb} we restrict τ_{c} at high and low frequencies. In the fast fluctuation regime, the lower limit $\tau_{\mathrm{c}} > 10^{-11}\,\mathrm{s}$ is given by a recent neutron measurement on YBCO [33] (see dotted line in Fig. 9). To determine an upper boundary for τ_{c}

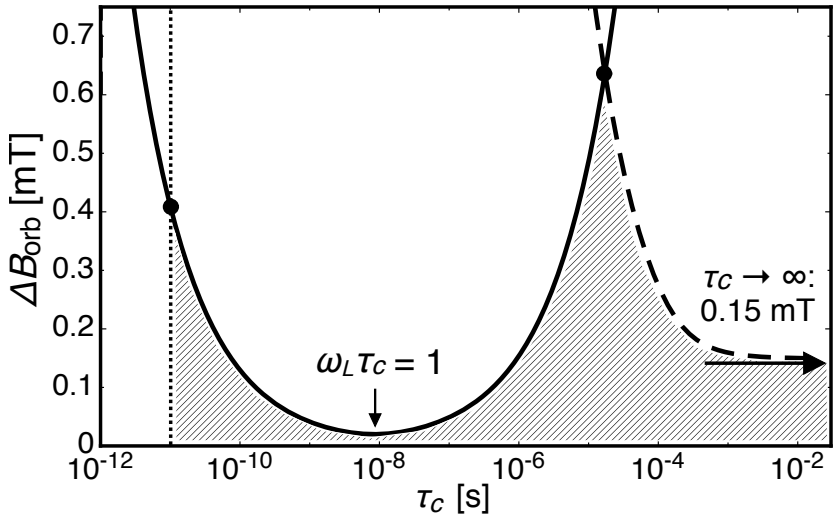

Figure 9: Possible orbital-current field amplitude $\Delta B_{\rm orb}$ as a function of the orbital-current correlation time $\tau_{\rm c}$ from ^{89}Y nuclear spin-lattice relaxation measurements in $Y_2Ba_4Cu_7O_{15-\delta}$ at 100 K (solid line, see text). The lower limit for $\tau_{\rm c}$ is taken from neutron scattering (dotted) [33] and the upper limit from our ^{89}Y line-width measurements (dashed line). The shaded area represents $\Delta B_{\rm orb}$ allowed by the ^{89}Y line width and nuclear spin-lattice relaxation measurements. The horizontal arrow indicates the maximum static field $\lesssim 0.15$ mT. After Paper **I** (Sec. 2.1.6).

we use the result of the line-width measurement and apply the formula for motional narrowing [50]

$$\delta\omega^2 = \delta\omega_{\rm r}^2 + (\delta\omega_{\rm static}^{\rm orb})^2 \cdot \frac{2}{\pi} \arctan(\alpha \cdot \delta\omega \cdot \tau_{\rm c}), \tag{13}$$

where $\delta\omega$ denotes the narrowed line width, $\delta\omega_{\rm static}^{\rm orb}$ the line width broadening from static orbital currents only, $\delta\omega_{\rm r}$ the line width at high temperatures for which the fast fluctuating orbital currents are averaged out on the line width, and α is a dimensionless factor of the order of unity. Reformulating Eq. (13) and substituting $\delta\omega_{\rm static}^{\rm orb} = 2 \cdot {}^{89}\gamma_n \, \Delta B_{\rm orb}$ (the factor of 2 is due to the two possible field directions) yields $\Delta B_{\rm orb} = \frac{1}{2 \cdot {}^{89}\gamma_n}[(\delta\omega^2 - \delta\omega_{\rm r}^2)\frac{\pi}{2}/\arctan(\alpha\tau_{\rm c}\delta\omega)]^{\frac{1}{2}}$. Taking twice the measured high temperature LEW of 250 Hz (Fig. 7) for $\delta\omega_{\rm r}/2\pi$ and twice the LEW of 400 Hz at 100 K for $\delta\omega/2\pi$ we were able to plot the corresponding $\Delta B_{\rm orb}$ as a function of $\tau_{\rm c}$ (dashed line in Fig. 9).

From Fig. 9 is obvious that our ^{89}Y NMR measurements defines a limit for the possible field amplitude at the Y-site in Y247 to $\Delta B_{\rm orb} \lesssim 0.7$ mT at 100 K. For putative oppositely circulating orbital currents in adjacent planes, as discussed above, this single-plane limit may have to be increased by a factor of ~ 5.

2.1.5 Conclusions

Our ^{89}Y NMR study of $Y_2Ba_4Cu_7O_{15-\delta}$ did not reveal any signature of orbital currents. Based on our experiments we provide an upper limit for fields at the Y-site. Static as well as dynamic field effects have been considered in the analysis and possible

interplane interactions in the bi-layer structure taken into account. We conclude that any additional static magnetic field at the Y-site in the normal conducting state below room temperature, would have to be $\lesssim 0.15\,\mathrm{mT}$. For the fluctuating field amplitude, an upper limit $\lesssim 0.7\,\mathrm{mT}$ was found. The limits established for fields that we would not be able to detect impose significant constraints on orbital-current models, since they are considerably smaller than the theoretical predictions for YBCO, which are in the range of several tens of mT.

2.1.6 Paper I: Lack of evidence for orbital-current effects in $Y_2Ba_4Cu_7O_{15-\delta}$ by NMR

This work is published in:

S. Strässle, J. Roos, M. Mali, T. Ohno, and H. Keller, *Lack of evidence for orbital-current effects in $Y_2Ba_4Cu_7O_{15-\delta}$ by NMR*, Physical Review Letters **101**, 237001 (2008).

Abstract

We have performed NMR measurements at the Y site on a *c*-axis oriented powder sample of the cuprate superconductor $Y_2Ba_4Cu_7O_{15-\delta}$ to search for the possible orbital-current phase. The temperature dependence of the Y line width and relaxation behavior in the normal conducting phase were studied down to 100 K. These measurements give upper limits for a static magnetic field and the amplitude of a fluctuating magnetic field at the Y site of $\lesssim 0.15$ mT and $\lesssim 0.7$ mT, respectively. These values provide significant constraints on possible static or quasi-static orbital currents.
DOI: 10.1103/PhysRevLett.101.237001
PACS numbers: 74.25.Nf, 75.40.Cx, 74.72.Bk, 76.60.Jx

Lack of Evidence for Orbital-Current Effects in the High-Temperature $Y_2Ba_4Cu_7O_{15-\delta}$ Superconductor using ^{89}Y Nuclear Magnetic Resonance

S. Strässle,* J. Roos, M. Mali, and H. Keller
Physik-Institut, Universität Zürich, CH-8057 Zürich, Switzerland

T. Ohno
Department of Physics, Faculty of Engineering, Tokushima University, Tokushima 770-8506, Japan
(Received 7 May 2008; published 1 December 2008)

We have performed NMR measurements at the Y site on a *c*-axis-oriented powder sample of the cuprate superconductor $Y_2Ba_4Cu_7O_{15-\delta}$ to search for the possible orbital-current phase. The temperature dependence of the Y linewidth and relaxation behavior in the normal-conducting phase were studied down to 100 K. These measurements give upper limits for a static magnetic field and the amplitude of a fluctuating magnetic field at the Y site of $\lesssim 0.15$ and $\lesssim 0.7$ mT, respectively. These values provide significant constraints on possible static or quasistatic orbital currents.

DOI: 10.1103/PhysRevLett.101.237001 PACS numbers: 74.25.Nf, 74.72.Bk, 75.40.Cx, 76.60.Jx

More than two decades after the discovery of high-T_c superconductivity, the understanding of the underlying mechanism still remains a key issue. Significant progress in experimental techniques has been made with respect to the cuprate problem, enabling deep insight into the nature of the phenomenon. Many theories and ideas to capture the physics of these oxides have been suggested, but there is yet no consensus on a theory of high-T_c superconductivity. Recent efforts [1–5] at explaining the exotic electronic properties of cuprates, in particular, the origin of the so-called pseudogap region, involve quantum critical fluctuations of orbital currents (OCs). These currents have been suggested to flow in the elementary O-Cu-O plaquettes within the CuO_2 planes and break time-reversal symmetry. Whether the translational invariance is violated depends on the suggested current pattern. The distinguishing characteristic of the formation of any such pattern is the resulting magnetic-field distribution.

So far, there is no agreement on the actual current path nor on its strength. Various experimental attempts to assess the orbital-current models have been made and provide evidence for breaking of time-reversal symmetry from observations of dichroism in angle-resolved photoemission spectroscopy (ARPES) measurements on $Bi_2Sr_2CaCu_2O_{8+\delta}$ [6]. However, it is possible that the observed effect is caused by superlattice modulations [7]. Introduction of Pb removes these structural distortions. Subsequent ARPES measurements on samples without this superstructure did not reveal any dichroism [8]. Translational symmetry is expected to be broken for the *d*-density wave (DDW) phase [1,3], since the corresponding unit cell doubles. In contrast to the DDW phase, a scenario of circulating currents (CCs) [5] preserves the translational symmetry. Recently reported neutron data [9] show qualitative consistency with one of the proposed patterns of CCs. The observed unusual long-range magnetic order in the pseudogap region of $YBa_2Cu_3O_{6+x}$ is static on the time scale of neutron scattering experiments, and the reported moments are of considerable strength (0.05–$0.1\,\mu_B$). A very recent zero-field muon-spin rotation experiment [10] on $La_{2-x}Sr_xCuO_4$ provides a rather low upper limit for static time-reversal violating local fields of 0.02 mT. However, according to Ref. [11] the magnetic field at the muon site, expected to be of several mT, is reduced by more than 2 orders of magnitude due to muon-related screening and finite-stiffness effects of the order parameter.

To our knowledge, there are no reports in the literature on a nuclear magnetic resonance (NMR) study dealing directly with current patterns confined to the copper plaquette in cuprates. NMR is a highly suitable method for studying magnetic fields using the noninvasive nuclear moments of the compounds' own atoms as microscopic probes. While NMR gives information on static as well as fluctuating internal fields, its ability to directly test the orbital-current models depends on the proposed current path and strength. Static fields arising from the proposed current phases (DDW and CC) cannot be seen directly in NMR measurements on nuclei of ions located in the CuO_2 plane, since the fields cancel at these sites for symmetry reasons. In YBCO compounds, the Y ions do not lie at centers of symmetry for the DDW and the CC phases, when considering just a single plane. As ^{89}Y is experimentally accessible through NMR, ^{89}Y NMR experiments should be sensitive to OC effects. Lee and Sha proposed such NMR measurements in the cuprate superconductor $Y_2Ba_4Cu_7O_{15-\delta}$ (Y247) [12]. This specific material exhibits a high transition temperature to superconductivity of $T_c = 95$ K and shows a clear pseudogap phase above T_c [13]. It consists of alternating $YBa_2Cu_3O_{7-\delta}$ (Y123) and $YBa_2Cu_4O_8$ (Y124) blocks. Pure Y124 is in the underdoped regime, featuring a pronounced pseudogap, whereas pure Y123 is close to optimal doping, showing no pseudogap features above T_c. The main structural difference

between Y123 and Y124 is that the latter possesses double chains with no oxygen vacancy, in contrast to single-chain Y123. As in Y124 and Y123, the CuO_2 planes in Y247 form bilayers separated by Y ions. Unlike the parent compounds, the adjacent planes in Y247 are unequally doped [13]. As was pointed out by Lee and Sha, this doping difference should to some extent prevent a possible cancellation of the staggered magnetic fields between bilayers [12].

In this Letter, we address the presence of OCs in Y247 by means of ^{89}Y NMR. With this method, and using the relation $^{89}\omega_L = {}^{89}\gamma_n B$ ($^{89}\gamma_n$ is the gyromagnetic ratio of the ^{89}Y nucleus) connecting the Larmor frequency ω_L with the magnetic field B, we are able to monitor the local magnetic field B at the single Y site accurately. Since ^{89}Y carries no quadrupole moment, the measured NMR linewidth (LW) and the nuclear spin-lattice relaxation (NSLR) are of purely magnetic origin. In our experiment, the observed field B is the sum of a large externally applied magnetic field B_0 and much smaller internal magnetic fields, part of the latter possibly stemming from OCs. Since the pseudogap is insensitive to large external magnetic fields [14], we conclude that B_0 should have a minor, if any, effect on the orbital currents. Note that if the internal fields are much smaller than B_0, then, in general, the internal static magnetic fields influence the NMR LW only when pointing along B_0. For the NSLR process of ^{89}Y, only magnetic fields fluctuating in a direction perpendicular to B_0 are relevant. We provide upper limits for static and dynamic field amplitudes created at the Y site in the normal-conducting phase.

The Y247 sample was prepared using solid-state techniques described elsewhere [15]. A pure Y247 phase with a phase-impurity level of less than 0.5% by volume was achieved. The powder was suspended in epoxy and oriented in a 9 T field in order to study anisotropic properties. This procedure yields samples with a high degree of c-axis alignment of its grains, whereas the a and b axes of the crystallites remain randomly distributed.

The NMR experiments were performed using a conventional phase-coherent pulse NMR spectrometer with an external field of $B_0 = 9$ T. The ^{89}Y NMR spectra were obtained by complex Fourier transformation of the spin echoes, which were recorded using a phase-alternating spin-echo accumulation technique. The NSLR time T_1 was measured using a saturation-pulse sequence. Temperatures in the range from 310 down to 100 K were controlled with a precision of better than 0.1 K.

Now we describe and discuss our results concerning static field effects originating from possible OCs. The formation of a static DDW or CC pattern in a plane, expected at $T_c < T < 310$ K, leads to a magnetic-field arrangement exhibiting additional static fields at the Y site. Because of the planar confinement of the currents, these fields are either directed perpendicular to the CuO_2 planes or lie parallel to them, depending on the type of pattern. In the case of CCs, the fields at all of the Y sites in a domain of correlated currents point in the same direction parallel to the plane. However, with B_0 applied parallel to the planes ($B_0 \perp c$), a symmetric broadening of the Y line, and not a shift, is expected for the following reasons: (i) The a- and b-axis directions of the crystallites in the c-axis-oriented powder are randomly distributed in a plane perpendicular to the c axis, and (ii) the domains of correlated CCs are of finite size. The DDW scenario, on the other hand, leads to antiferromagnetically arranged fields at neighboring Y sites within a particular domain, pointing perpendicular to the CuO_2 planes. Hence, a splitting of the absorption line should be observed when B_0 is applied perpendicular to the planes ($B_0 \parallel c$). However, this splitting may well be unresolved. In this case, an additional symmetric broadening of the Y line should still appear. Thus the temperature dependence of the ^{89}Y LW is directly influenced by the appearance of OCs, but in the discussed cases only for a particular direction of B_0.

The temperature dependence of the ^{89}Y NMR LW and frequency in the normal-conducting phase of Y247 from

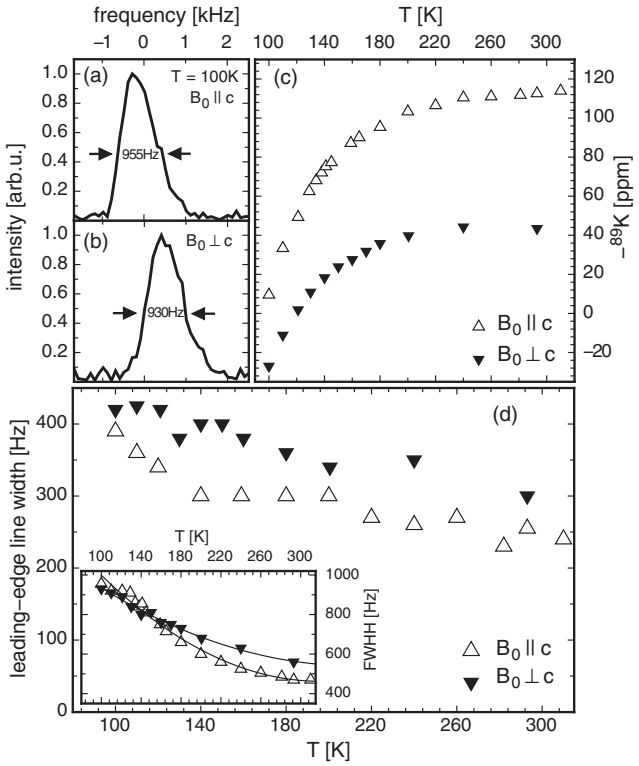

FIG. 1. ^{89}Y NMR data measured in $B_0 = 9$ T for field orientations parallel ($\parallel$) and perpendicular ($\perp$) to the crystalline c axis in oriented powder of $Y_2Ba_4Cu_7O_{15-\delta}$. Panels (a) and (b) show typical absorption lines relative to 18.867 53 MHz at 100 K for both field orientations with a FWHH of 955(50) and 930 (50) kHz, respectively. Panel (c) displays the temperature dependence of the magnetic shift. In (d), the temperature dependence of the leading-edge ^{89}Y NMR linewidth at half height is shown. The inset shows the temperature dependence of the FWHH (solid lines are guides to the eye).

room temperature down to 100 K were measured for both field orientations. The results are presented in Fig. 1. When cooling, a substantial drop of the measured ^{89}Y magnetic shift [Fig. 1(c)] was observed, which clearly demonstrates the presence of the pseudogap state in the sample. Figures 1(a) and 1(b) display typical examples of the measured ^{89}Y absorption lines at 100 K for both field orientations. In pure Y124, we obtained a Y absorption line, which has a symmetric shape for all temperatures from room temperature down to 100 K with a nearly constant width. This behavior implies that the Y LW of stoichiometric Y124 is mainly due to dipolar interactions. In contrast, Y247 exhibits an Y line asymmetry towards higher frequencies, which we attribute to doping inhomogeneity of the Y247 compound introduced by the Y123 blocks. It is known that in this temperature range the nonstoichiometric Y123 compounds exhibit oxygen clustering in the CuO chains which affects the homogeneity of the doping. The magnetic shift is strongly dependent on the mobile carrier density (doping). Thus, a variation in carrier density entails a distribution of the Y magnetic shift, leading to a broadening of the Y line. The magnetic line shift of Y arises mainly from two contributions: a negative carrier-related shift and a positive temperature-independent chemical shift [16]. Oxygen clustering in the single chains causes a carrier-density variation, which cannot exceed the density of Y1237 (filled chains, slightly overdoped) but can have values corresponding to substantial underdoping. Since the Y magnetic shift is negative, the broadening of the Y line is asymmetric towards higher frequencies. Upon cooling from room temperature, the Y magnetic shift decreases when the pseudogap opens [Fig. 1(c)]; the larger the magnitude of the pseudogap, the stronger the decrease. The magnitude of the pseudogap strongly depends on the doping level. Nearly optimally doped Y123 shows almost no temperature dependence of the plane copper shift, whereas underdoped Y124 with its substantial pseudogap shows a strong decrease of the plane copper shift in the investigated temperature range (see, e.g., Ref. [13]). Therefore, inhomogeneous doping should lead to a steady increase of the full Y LW in Y247, accompanied by a growing asymmetry of the line shape with decreasing temperature. This is indeed observed. The full Y LW (FWHH) [Fig. 1(d), inset] and its skewness increase for both field orientations when cooling. In addition, we detect a crossing of the two temperature dependences of the FWHH at $\sim$140 K. This is expected from doping inhomogeneity, since for measurements with $B_0 \parallel c$ the drop of the magnetic shift due to the pseudogap is more pronounced as compared to the one with $B_0 \perp c$ [Fig. 1(c)]. This difference causes a stronger line broadening for $B_0 \parallel c$ than $B_0 \perp c$, implying that the two curves for $B_0 \parallel c$ and $B_0 \perp c$ cross each other at $\sim$140 K [Fig. 1(d), inset].

In order to minimize the disturbing influence of doping inhomogeneity, we have focused on the leading-edge LW at half height (LEW) to detect the symmetric broadening due to possible OCs. The temperature dependence of the LEW for both field orientations is plotted in Fig. 1(d). The high-temperature limit of the LEW for Y247 agrees with that of Y124, within measurement uncertainties. For both field orientations at 100 K, an increase in the LEW of $\sim$150 Hz is obtained as compared to the 310 K value. Assuming this increase is caused entirely by static OC effects, the maximum field amplitude at the Y site in Y247 is $[\{(400\ \mathrm{Hz})^2 - (250\ \mathrm{Hz})^2\}/{}^{89}\gamma_n^2]^{(1/2)} \approx 0.15$ mT. This number was deduced under the conservative assumption that different effects contributing to the LEW add quadratically. Note that the LEW increases for both field orientations.

A bilayer structure possibly causes a cancellation of fields if there is an antiferromagnetic interplane interaction between OCs of neighboring planes. Although results from neutron measurements favor an in-phase OC circulation [9,17], we assume antiphase circulation because of the coupling between OCs from adjacent planes, which increases the upper limit of the single plane field. The carrier density in Y247 for planes from both blocks (Y123 and Y124) has been deduced, and a difference of $\sim$20% was determined [13]. We take the difference of the orbital-current strength j to be of the same order of magnitude, because j is inversely proportional to the doping level [4,18]. Therefore, in the case of antiphase circulation of OCs in neighboring planes, we may have to increase our single layer limit by a factor of $\sim$5 and end up with a maximum field of $\sim$0.75 mT at the Y site from OCs in a single CuO_2 plane. Unless the actual current pattern differs from the proposed ones, a LW broadening due to OCs is expected only for one orientation, which is not the case. Therefore, the estimated field amplitude due to OCs is rather strongly exaggerated.

Next, we describe and discuss the NSLR and LW experiments in the context of possible nonstatic OCs and provide an upper limit for the additional field amplitude at the Y site due to fluctuating OCs. For the NSLR rate $1/T_1$, the time-dependent local magnetic fields perpendicular to the quantization axis, given by B_0, are relevant. As stated before, OCs create fields that fluctuate either parallel or perpendicular to the CuO_2 planes. Consequently, the appearance of fluctuating OCs on varying the temperature should change the rate anisotropy $R = {}^{89}T_1^{\parallel}/{}^{89}T_1^{\perp}$. ${}^{89}T_1^{\parallel}$ (${}^{89}T_1^{\perp}$) denotes the relaxation time for B_0 parallel (perpendicular) to the c axis. The NSLR rate in the normal-conducting phase has been determined up to 300 K for both field orientations. The ^{89}Y magnetization relaxation shows the expected single-exponential relaxation behavior. At 100 K, we found ${}^{89}T_1^{\parallel} = 103.4(2.0)$ s and ${}^{89}T_1^{\perp} = 91.0(2.5)$ s. The measured NSLR rate can be written as a sum $1/{}^{89}T_1 = 1/{}^{89}T_1' + 1/{}^{89}T_1^{\mathrm{orb}}$, where the first term in the sum is the rate due to mechanisms not related to OCs and the second term is due to possible OCs. Within error, the measured R is constant from 100 to 300 K with a weighted average of $\bar{R} = 1.145(18)$. Taking twice the error of $\bar{R}$ as the upper limit of the change due to possible OCs at

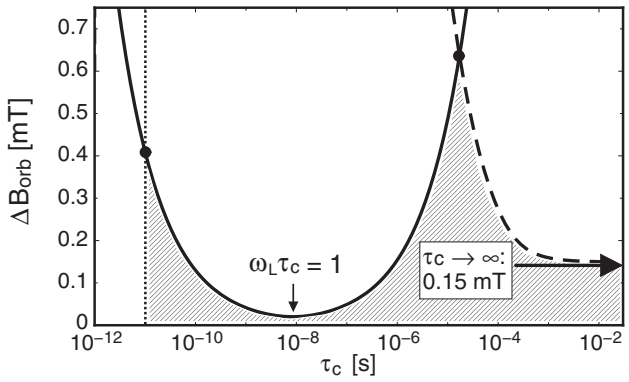

FIG. 2. Dependence of the possible OC field amplitude ΔB_{orb} on the OC correlation time τ_c from ^{89}Y NSLR measurements in Y247 at 100 K (solid line, see text). The lower limit of τ_c from neutron (dotted line) and the upper limit of τ_c from LW measurements (dashed line) are shown. The shaded area represents all ΔB_{orb} consistent with the ^{89}Y LW and NSLR measurements. The horizontal arrow indicates the maximum static field $\lesssim 0.15$ mT.

100 K, the maximum effect at the lowest temperature measured does not exceed 3%. Considering this possible change as being caused purely by fluctuating OCs, we deduce an upper limit for the corresponding fluctuating field amplitude. The relation between $^{89}T_1^{\mathrm{orb}}$, the fluctuating OC field amplitude ΔB_{orb}, and the associated correlation time for the fluctuating orbital-current pattern τ_c is given by [19]

$$\frac{1}{^{89}T_1^{\mathrm{orb}}} \approx \overline{^{89}\gamma_n^2 \Delta B_{\mathrm{orb}}^2} \frac{\tau_c}{1 + (\omega_L \tau_c)^2}. \quad (1)$$

Taking an additional contribution of 3% for the NSLR rate due to possible OCs (see above) and $\Delta B_{\mathrm{orb}} = \{[1 + (\omega_L \tau_c)^2]/(^{89}\gamma_n^2 T_1^{\mathrm{orb}} \tau_c)\}^{(1/2)}$ from Eq. (1), we plot ΔB_{orb} versus τ_c (see solid line in Fig. 2). To get an upper limit for ΔB_{orb}, we restrict τ_c at high and low frequency. In the fast fluctuation regime, the lower limit $\tau_c > 10^{-11}$ s is given by a recent neutron measurement on YBCO [9] (see dotted line in Fig. 2) [20]. To determine an upper boundary for τ_c, we use the result of the LW measurement and apply the formula for LW motional narrowing [21]

$$\delta\omega^2 = \delta\omega_r^2 + (\delta\omega_{\mathrm{static}}^{\mathrm{orb}})^2 \frac{2}{\pi} \arctan(\alpha \delta\omega \tau_c), \quad (2)$$

where $\delta\omega$ denotes the motionally narrowed LW, $\delta\omega_{\mathrm{static}}^{\mathrm{orb}}$ represents the LW broadened by static orbital-current effects only, $\delta\omega_r$ is the LW at high temperatures, where the fast fluctuating orbital-current effects on the LW are averaged out, and α is a dimensionless factor of the order of unity. Reformulating Eq. (2) and using $\delta\omega_{\mathrm{static}}^{\mathrm{orb}} = 2 \times {}^{89}\gamma_n \Delta B_{\mathrm{orb}}$ (the factor of 2 is due to the two possible field directions) yields $\Delta B_{\mathrm{orb}} = \frac{1}{2\,^{89}\gamma_n}[(\delta\omega^2 - \delta\omega_r^2)\frac{\pi}{2}/\arctan(\alpha\tau_c\delta\omega)]^{(1/2)}$. Taking twice the measured high-temperature LEW of 250 Hz [Fig. 1(d)] as $\delta\omega_r/2\pi$ and twice the LEW of 400 Hz at 100 K as $\delta\omega/2\pi$, we are able to plot the corresponding ΔB_{orb} as a function of τ_c (dashed line in Fig. 2). From Fig. 2, it is obvious that ^{89}Y NMR experiments set an upper limit for the OC field amplitude at the Y site in Y247 of $\Delta B_{\mathrm{orb}} \lesssim 0.7$ mT at 100 K. In the case that this field is the result of putative antiphase circulating OCs in the neighboring planes, then, as discussed before, the limit for the field coming from one plane only would have to be increased by a factor of ~ 5.

In summary, from our ^{89}Y NMR measurements in $Y_2Ba_4Cu_7O_{15-\delta}$ we conclude that any additional static magnetic field at the Y site, showing up in the normal-conducting state below room temperature, is smaller than 0.15 mT. For the fluctuating field amplitude, we find an upper limit $\lesssim 0.7$ mT. These values are considerably smaller than theoretical predictions for YBCO, which are in the range of several tens of mT; see, e.g., [11].

The authors appreciate discussion with M. V. Eremin, P. F. Meier, and B. Graneli. Financial support by the Swiss National Foundation is acknowledged.

*simon.straessle@physik.uzh.ch

[1] T. C. Hsu, J. B. Marston, and I. Affleck, Phys. Rev. B **43**, 2866 (1991).
[2] C. Nayak, Phys. Rev. B **62**, 4880 (2000).
[3] S. Chakravarty, R. B. Laughlin, D. K. Morr, and C. Nayak, Phys. Rev. B **63**, 094503 (2001).
[4] C. M. Varma, Phys. Rev. B **73**, 155113 (2006).
[5] V. Aji and C. M. Varma, Phys. Rev. Lett. **99**, 067003 (2007).
[6] A. Kaminski *et al.*, Nature (London) **416**, 610 (2002).
[7] J. P. Castellan *et al.*, Phys. Rev. B **73**, 174505 (2006).
[8] S. V. Borisenko *et al.*, Phys. Rev. Lett. **92**, 207001 (2004).
[9] B. Fauqué *et al.*, Phys. Rev. Lett. **96**, 197001 (2006).
[10] G. J. MacDougall *et al.*, arXiv:0801.2716.
[11] Arkady Shekhter *et al.*, arXiv:0802.2972.
[12] P. A. Lee and G. Sha, Solid State Commun. **126**, 71 (2003).
[13] R. Stern *et al.*, Phys. Rev. B **50**, 426 (1994).
[14] K. Gorny *et al.*, Phys. Rev. Lett. **82**, 177 (1999); Guo-qing Zheng *et al.*, Phys. Rev. B **60**, R9947 (1999).
[15] J.-Y. Genoud *et al.*, Physica (Amsterdam) **192C**, 137 (1992).
[16] H. Alloul, T. Ohno, and P. Mendels, Phys. Rev. Lett. **63**, 1700 (1989).
[17] Y. Sidis *et al.*, Physica (Amsterdam) **397B**, 1 (2007).
[18] M. V. Eremin, I. Eremin, and A. Terzi, Phys. Rev. B **66**, 104524 (2002).
[19] C. P. Slichter, *Principles of Magnetic Resonance* (Springer, Berlin, 1990).
[20] Since the orbital-current phase is thought of as a thermodynamic state with a well-defined transition, the energy scale of involved fluctuations must be well below the transition temperature to stabilize the phase. Considering this, energy arguments also end up with a correlation time similar to the one from neutron measurements.
[21] A. Abragam, *Principles of Nuclear Magnetism* (Clarendon, Oxford, 1961).

2.2 NMR investigations of $LaBa_2Cu_3O_{7-\delta}$

2.2.1 Motivation

The recent report of a checkerboard-like electronic lattice, first discovered by means of scanning tunneling microscopy in vortex cores of optimally doped $Bi_2Sr_2CaCu_2O_{8+\delta}$ [62], may stand for the present vivid discussion about electronic charge effects and cuprate superconductivity, see *e.g.* [61]. Likewise a recent tunneling study of La- and Pb-doped single-crystalline $(BiPb)_2(SrLa)_2CuO_{6+\delta}$ also revealed checkerboard-like features [37]. The observed charge modulation was found to be doping dependent and explained as originating from a static, energy independent charge density wave in the anti-nodal region. Due to the appearance of the charge density wave and the pseudogap at close temperatures, it has been suggested that the respective gaps actually may be one and the same. Since the experimental basis does not yet suffice to remove the ambiguity, further experiments sensitive to charge effects are highly desirable.

Features related to electronic charge may be investigated with nuclear resonance methods if nuclei with quadrupole moments are present. Since charge carriers in the cuprates are confined mainly to the CuO_2 planes, it is tempting to utilize the copper and oxygen nuclei. Below room temperature, however, these nuclei relax predominately through magnetic interaction with Cu atomic spins, which fluctuate strongly when the antiferromagnetic parent compound is doped with holes, see *e.g.* [63]. The doping thus reduces the long-range antiferromagnetic coherence such that only short-range correlations survive.

An alternative approach to assess the nature of charge effects in cuprates is to investigate bi-layer YBCO compounds. The Y-site is suitable for investigating charge features, since whatever remains of antiferromagnetism cancels for symmetry reasons. The remaining purely magnetic spin-lattice relaxation of the Y-nuclei is solely due to mobile carriers and consequently very weak. The Y-atom is located between two neighboring planes, but does not have the quadrupole moment required and therefore must be substituted for a suitable rare earth atom. It is noteworthy that replacing the Y-atom with another rare earth element does not alter the transition temperature, except for Pr and Ce. First we investigated $LuBa_2Cu_3O_{7-\delta}$ single crystals, but despite an extensive effort we failed to detect a ^{175}Lu NMR or NQR signal. Most probably the nuclear magnetization of Lu relaxes too fast for our spectrometer due to the huge quadrupole moment of Lu. Next, the efforts were directed toward high-quality $LaBa_2Cu_3O_{7-\delta}$ powder samples. ^{139}La has a nuclear spin $I = \frac{7}{2}$ and a quadrupole moment roughly an order of magnitude smaller than that of ^{175}Lu. We readily detected both the ^{139}La NMR and the ^{139}La NQR signals. With the ^{139}La as NMR probe, the temperature dependence of important NMR/NQR parameters, such as the nuclear spin-lattice and the nuclear spin-spin relaxation times, were investigated.

2.2.2 Experimental details

The $LaBa_2Cu_3O_{7-\delta}$ powder was prepared at the Paul Scherrer Institut by K. Conder and E. Pomjakushina with a solid-state reaction using La_2O_3, $BaCO_3$, and CuO of a minimum purity of 99.99%. The reagents were mixed and calcinated in air at temper-

atures between $800 - 920^o$ C during at least 80 h, with several intermediate grindings. Subsequent sample treatment was the same as described in Ref. [64] (Series 3). Optimal doping of the sample, *i.e.* a transition temperature of $T_c \approx 91$ K, was achieved after the final annealing procedure according to Ref. [65]. A subsequent X-ray diffraction analysis yielded an impurity content of $< 2\%$.

A fraction of the powder was oriented in epoxy resin, according to the same procedure as described in Sec. 2.1.3.

The ^{139}La NMR experiments were carried out in a 9 T magnet. For conceptual and technical details of NMR/NQR see Sec. 2.1.1. Temperatures were controlled using a flow cryostat. A conventional phase-coherent pulse spectrometer was employed. The spin-lattice relaxation time was measured applying an inversion-recovery pulse sequence and a phase-alternating spin-echo accumulation technique. The spin-spin relaxation was determined in the usual manner from the decay of the spin-echo intensity.

2.2.3 Results and discussion

From the NQR spectrum obtained at 100 K (Fig. 10) we determined the quadrupole frequency ν_Q of the La nucleus in $^{139}LaBa_2Cu_3O_{7-\delta}$ to be $^{139}\nu_Q = 4.295$ MHz. A further important parameter, the asymmetry parameter $\eta = (V_{xx} - V_{yy})/V_{zz}$, was found to be $\eta = 0.23$ for the La-site.

Using these results, we successfully simulated the recorded ^{139}La NMR spectrum of an oriented powder sample in a 9 T field applied parallel and perpendicular to the crystalline c-axis. Figure 11a shows a typical NMR spectrum. From the frequency position of the central line, the magnetic shift was determined to be $K = 300(30)$ ppm at 100 K. Within experimental error no anisotropy was found.

The mechanisms responsible for the La nuclear spin relaxation were subsequently studied. First we focused on the normal-conducting phase up to 350 K. The decay of the spin-echo intensity was measured, from which the relevant spin-spin relaxation time constant T_2 was extracted (Sec. 2.1.1). The temperature dependence of the spin-spin relaxation rate T_2^{-1} for both field orientations showed distinct steps and plateaus (Fig. 11b). The origin of this unexpected behavior could not conclusively be brought in connection with charge inhomogeneities related to superconductivity or the pseudogap. Extensive investigations revealed that these features cannot be exactly reproduced, but strongly depend on the thermal history of the sample. Slow dynamics, such as oxygen diffusion and clustering in the CuO chains, are assumed to be the source of the unexpected temperature behavior.

As a measure of the spin-lattice relaxation we choose the time T_{1e} needed by the nuclear magnetization to recover after saturation to its 1/e value. Further investigations are necessary, though, to elaborate on the character of the relaxation mechanism, which would allow us to apply the appropriate decay function to determine T_1. T_{1e}, however, still reflects the correct temperature dependence of the relaxation, which allows us to draw qualitative conclusions about the relaxation mechanism. The experimental results are shown in Fig. 12c. Our ^{139}La spin-lattice relaxation measurements revealed a thermally activated relaxation process above ~ 300 K, which we relate to the diffusion of oxygen ions in the chain structure. The activation energy of the oxygen diffusion was

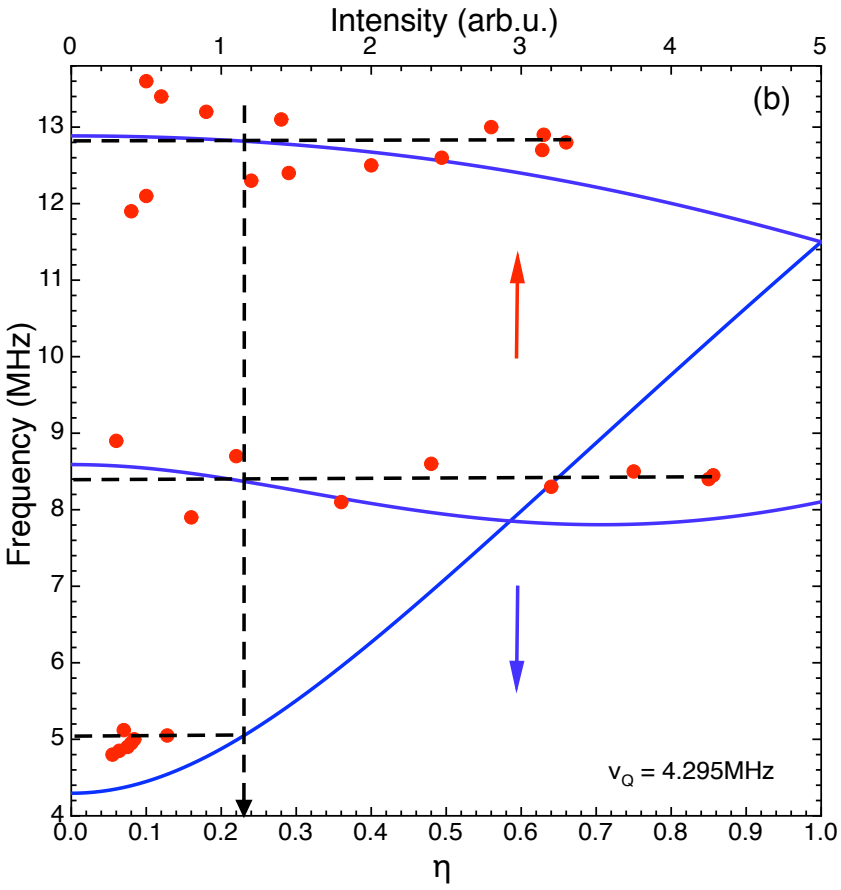

Figure 10: ^{139}La NQR spectrum measured at 100 K in a loose powder sample of $LaBa_2Cu_3O_{7-\delta}$ (red dots). The blue lines show the asymmetry parameter η for $^{139}\nu_Q = 4.295$ MHz, calculated by exact diagonalization of the Hamiltonian in Eq. (1).

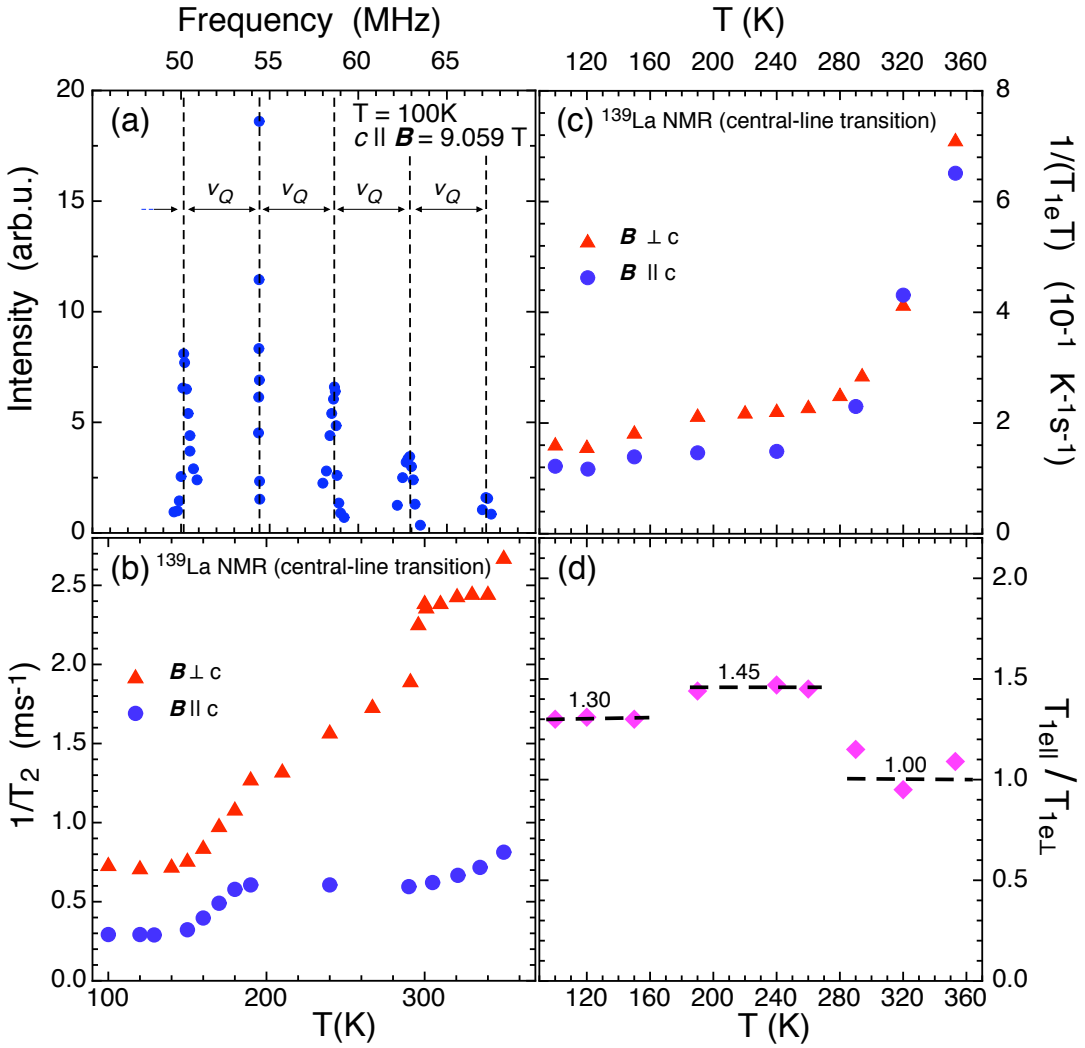

Figure 11: Normal state ^{139}La NMR parameters measured in an applied magnetic field of 9.01 T with a c-axis oriented powder sample of $LaBa_2Cu_3O_{7-\delta}$ ($T_c \approx 91$ K). Panel (a) shows the NMR spectrum recorded at 100 K for 9 T $\parallel$ c. Since ^{139}La has a nuclear spin $I = \frac{7}{2}$ the spectrum consists of a central line ($\frac{1}{2} \leftrightarrow \frac{1}{2}$) and 6 satellite lines. The two satellite lines lowest in frequency were not measured. (b) the temperature dependence of the spin-spin relaxation rate measured at the central-line transition is depicted for both field orientations. (c) the temperature dependence of the spin-lattice relaxation rate per temperature unit, measured for the central-line transition for both field orientations. (d) the temperature dependence of the spin-lattice relaxation rate anisotropy ratio.

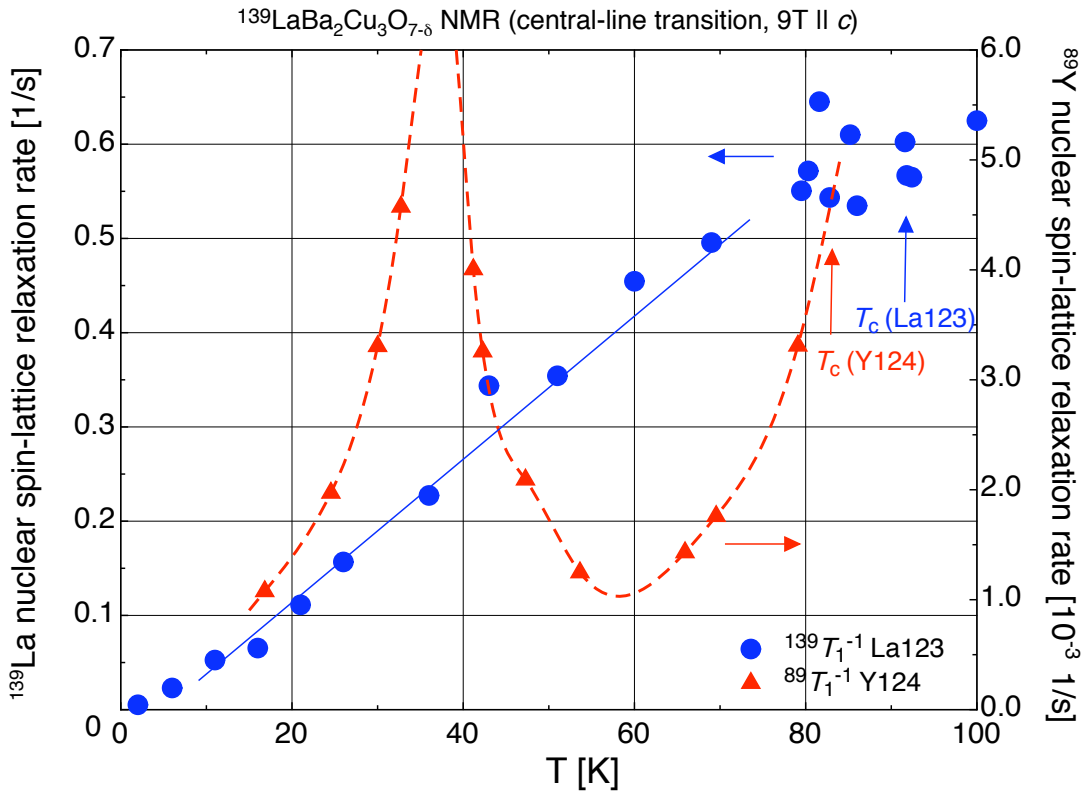

Figure 12: Blue dots (left axis) show the low-temperature dependence of the spin-lattice relaxation rate measured for the central-line transition of ^{139}La in a c-axis oriented powder sample of $LaBa_2Cu_3O_{7-\delta}$ (La123) for a 9 T field applied parallel to the c-axis. The red triangles (right axis) illustrate, for comparison, the temperature dependence of the ^{89}Y spin-lattice relaxation rate measured in $YBa_2Cu_4O_8$ (Y124) [66]. A distinct rate maximum due to interactions with vortices is present in the ^{89}Y data, which was not found in the ^{139}La relaxation of La123. The respective transition temperatures are indicated by vertical arrows. Lines are guides to the eye.

found to correspond to ~ 2000 K. The spin-lattice relaxation rate for temperatures where diffusion dominates is nearly isotropic, whereas the anisotropy ratio attains a value of 1.45 in the temperature range of $200-280$ K but decreases again below 200 K (Fig. 11d).

In the superconducting state, the ^{139}La NMR spin-lattice relaxation measurements show an unexpected temperature behavior (Fig. 12). In the similar compound $YBa_2Cu_4O_8$, the ^{89}Y nuclei relax so weakly, that the interaction with vortices manifests itself as a distinct maximum in the temperature dependence of the spin-lattice relaxation rate well below $T_c \approx 81$ K [66] (red triangles in Fig. 12). As expected for nuclei having spin $^{139}I = \frac{7}{2}$, the ^{139}La relaxation rate is much higher than for $^{89}I = \frac{1}{2}$. No rate maximum due to vortices was found. In contrast to the case for Y, the decrease of the relaxation rate with temperature below T_c is less pronounced for La, as can be seen in Fig. 12. This clearly indicates that charge effects influence the relaxation process of the nuclear magnetization of La in $LaBa_2Cu_3O_{7-\delta}$. Again, additional measurements are necessary in order to quantify these findings, in particular NQR relaxation studies may provide

valuable information about the nature of the fluctuations involved.

2.2.4 Conclusions

We determined the ^{139}La magnetic shift tensor, the quadrupole frequency, and the asymmetry parameter in $LaBa_2Cu_3O_{7-\delta}$. The present status of our ^{139}La NMR/NQR investigation does, however, not allow a conclusive statement about the role of charge inhomogeneity effects in the cuprates. The findings strongly depend on effects that are expected to be of minor relevance for superconductivity. In particular the unexpected and apparently complex behavior of the nuclear relaxation of the ^{139}La spin-spin relaxation needs to be better understood. From the temperature dependence of the ^{139}La spin-lattice relaxation, however, we have evidence that charge effects are indeed involved in the nuclear spin dynamics.

2.2.5 Paper II: ^{139}La NMR and NQR investigations of the superconductor $LaBa_2Cu_3O_{7-\delta}$

This work is published in:

S. Strässle, J. Roos, M. Mali, K. Conder, E. Pomjakushina, and H. Keller, *^{139}La NMR and NQR investigations of the superconductor $LaBa_2Cu_3O_{7-\delta}$*, Physica C **460-462**, 890 (2007).

Abstract

In cuprates charge inhomogeneities seem to exist as self-organized objects, which are possibly related to the appearance of the pseudo-gap. Since high-quality powder samples of $LaBa_2Cu_3O_{7-\delta}$ ($T_c = 91$K) have recently been synthesized, we were able to perform ^{139}La NMR/NQR investigations of $LaBa_2Cu_3O_{7-\delta}$. Our study includes measurements of ^{139}La spin-spin and spin-lattice relaxation in a field of 9T in the normal conducting phase at temperatures from 350 K to 100 K in oriented powder samples. Preliminary results show an unusual behavior of ^{139}La spin-lattice and spin-spin relaxation possibly related to charge inhomogeneity effects.

Keywords: NMR; NQR; $LaBa_2Cu_3O_{7-\delta}$

DOI: 10.1016/j.physc.2007.03.182

Available online at www.sciencedirect.com
ScienceDirect
Physica C 460–462 (2007) 890–891
PHYSICA C
www.elsevier.com/locate/physc

^{139}La NMR and NQR investigations of the superconductor $LaBa_2Cu_3O_{7-\delta}$

S. Strässle [a,*], J. Roos [a], M. Mali [a], K. Conder [b], E. Pomjakushina [b,c], H. Keller [a]

[a] Physik-Institut, Universität Zürich, CH-8057 Zürich, Switzerland
[b] Laboratory for Developments and Methods, Paul Scherrer Institut, CH-5232 Villigen PSI, Switzerland
[c] Laboratory for Neutron Scattering, ETH Zürich and Paul Scherrer Institut, CH-5232 Villigen PSI, Switzerland

Available online 28 March 2007

Abstract

In cuprates charge inhomogeneities seem to exist as self-organized objects, which are possibly related to the appearance of the pseudo-gap. Since high-quality powder samples of $LaBa_2Cu_3O_{7-\delta}$ ($T_c = 91$ K) have recently been synthesized, we were able to perform ^{139}La NMR/NQR investigations of $LaBa_2Cu_3O_{7-\delta}$. Our study includes measurements of ^{139}La spin–spin and spin–lattice relaxation in a field of 9 T in the normal conducting phase at temperatures from 350 K to 100 K in oriented powder samples. Preliminary results show an unusual behavior of ^{139}La spin–lattice and spin–spin relaxation possibly related to charge inhomogeneity effects.

Keywords: NMR; NQR; $LaBa_2Cu_3O_{7-\delta}$

1. Introduction

Over the past years in numerous papers evidence for mesoscopic dynamic and static electronic charge inhomogeneities in cuprates has been reported. These electronic inhomogeneities seem to show up in the form of self-organized objects possibly related to the appearance of the pseudo-gap. In NMR/NQR experiments static electronic inhomogeneities have been mainly detected in the underdoped LSCO systems (see, e.g. Refs. [1,2]), but not in YBCO compounds [3]. In the fully stoichiometric member of the YBCO family, $YBa_2Cu_4O_8$, dynamic charge inhomogeneities have been related to the observed quadrupolar contribution to the planar oxygen spin–lattice relaxation [4].

To better distinguish the effect of the charge inhomogeneities in the YBCO family we decided to study them at the Y site. Due to the Y site symmetry the strong magnetic-field fluctuations originating from the antiferromagnetically correlated Cu spins in adjacent CuO_2 planes cancel out in contrast to the charge effects. Therefore, NQR and NMR investigations of a nucleus at this site can much easier detect through electric quadrupole interaction with the onsite electric-field gradient the full charge effects. However, Y with a nuclear spin $I = 1/2$ is not suitable for such a study, because it carries no electric quadrupole moment and consequently shows no quadrupole interaction. Therefore, compounds where Y is replaced by nuclei ($I > 1/2$) with an electric quadrupole moment are needed.

Since high-quality powder samples of $LaBa_2Cu_3O_{7-\delta}$ have recently been synthesized successfully by Conder and Pomjakushina, we are able to perform ^{139}La ($I = 7/2$) NMR/NQR studies in $LaBa_2Cu_3O_{7-\delta}$. We report on preliminary results.

2. Sample preparation

The sample of $LaBa_2Cu_3O_{7-\delta}$ was synthesised by a solid-state reaction using La_2O_3, $BaCO_3$, and CuO of a minimum purity of 99.99%. The respective amounts of starting reagents were mixed and calcinated at temperatures 800–920 °C during at least 80 h in air, with several

* Corresponding author. Tel.: +41 (0) 44 635 5576; fax: +41 (0) 44 635 5704.
E-mail address: simon.straessle@physik.unizh.ch (S. Strässle).

0921-4534/$ - see front matter © 2007 Elsevier B.V. All rights reserved.
doi:10.1016/j.physc.2007.03.182

intermediate grindings. The sample was then treated following the procedure as described in Ref. [5] (Series 3). With final annealing according to Ref. [6] optimal doping of the sample was achieved. Conventional X-ray diffraction analysis yields an impurity content of <2% and unit cell parameters (space groups Pmmm): $a = 3.8939(2)$ Å, $b = 3.9429(4)$ Å, $c = 11.7939(7)$ Å.

3. Preliminary results and discussion

By means of NQR we have determined the quadrupole frequency of the ^{139}La nucleus in $LaBa_2Cu_3O_{7-\delta}$ at 100 K to be $\nu_Q = 4.295$ MHz. The asymmetry parameter at the La site was found to be $\eta = 0.23$. With these values we were able to simulate the ^{139}La NMR spectrum obtained from c-axis oriented powder samples at 100 K, yielding a magnetic shift with respect to a $LaCl_3$ reference solution $[\nu_L(B = 9\ \mathrm{T}) = 54.388950\ \mathrm{MHz}]$ of $K = 300(30)$ ppm. The shift is isotropic within experimental error.

At the central-line transition of the NMR spectrum we measured the nuclear spin–lattice relaxation (NSLR) rate of ^{139}La in $LaBa_2Cu_3O_{7-\delta}$. The nuclear magnetization showed no single exponential recovery behavior. As a measure of the spin–lattice relaxation we choose the time T_{1e} necessary for the nuclear magnetization to recover after saturation onto its 1/e equilibrium value. In an external field of 9 T the rate $(T_{1e})^{-1}$ was determined in a temperature range from 350 K down to 100 K for both field orientations, B parallel ($B\|c$) and perpendicular to the c-axis ($B\perp c$). ^{139}La shows a stronger relaxation behavior than expected from appropriate scaling of Y relaxation data (see, e.g. Ref. [7]) taking into account the different nuclear spins I and gyromagnetic ratios. Provided that there is no dramatic change of the magnetic-field fluctuation spectrum, this indicates, that for ^{139}La exists a quadrupolar relaxation channel not present for the Y nucleus. This additional relaxation is possibly related to charge dynamics in the planes or the chains of $LaBa_2Cu_3O_{7-\delta}$. To be sure that the relevant magnetic fluctuation at the Y site in $YBa_2Cu_3O_{7-\delta}$ are not changed essentially by the exchange of Y with La, the NSLR of the plane copper and the oxygen in $LaBa_2Cu_3O_{7-\delta}$ should be checked. Above 270 K $(^{139}T_{1e})^{-1}$ seems to be thermally activated with an activation energy of ≈2000 K. Within experimental error, no anisotropy of the rate is found above 300 K, whereas below 270 K the ratio $^{139}(T_{1e}^{\|}/T_{1e}^{\perp})$ yields 1.45. At temperatures below 200 K, this anisotropy seems to be reduced, below 150 K a value of 1.30 was obtained.

In addition, we have measured the temperature dependence of the nuclear spin–spin relaxation (NSSR) rate $(T_2)^{-1}$ at the central-line transition for both field directions, see inset Fig. 1. It shows a clear anisotropy in the whole temperature range. From 100 K up to 180 K this anisotropy has a constant decrease with increasing temperature.

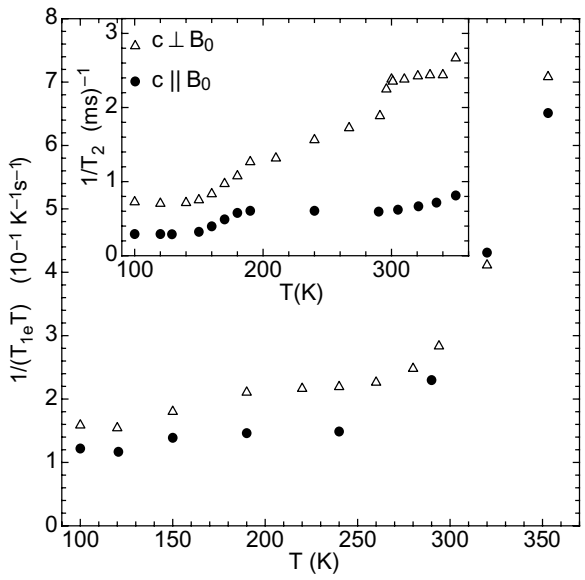

Fig. 1. ^{139}La nuclear spin–lattice relaxation rate per temperature unit vs. temperature for the magnetic-field direction parallel (circles) and perpendicular (triangles) to the c axis of the oriented $LaBa_2Cu_3O_{7-\delta}$ powder sample. The inset shows the nuclear spin–spin relaxation rate vs. temperature for $B\|c$ and $B\perp c$.

Whereas, from 180 K up to room temperature, the anisotropy ratio $(T_2^{\|}/T_2^{\perp})$ strongly increases. The NSSR rates $(T_2^{\|})^{-1}$ and $(T_2^{\perp})^{-1}$ are nearly temperature independent between 100 K and 150 K. In the temperature range from 150 K up to 200 K the rates increase with increasing temperature. At 200 K we found a doubling of the rates with respect to 150 K. Above 200 K $(T_2^{\|})^{-1}$ remains constant up to nearly room temperature, whereas $(T_2^{\perp})^{-1}$ further increases. At 290 K $(T_2^{\perp})^{-1}(T)$ exhibits a distinct step to higher rates.

To clarify the complex behavior of the NSLR and the NSSR further investigations are necessary.

Acknowledgements

We thank the Swiss National Science Foundation and the NCCR program MaNEP for partial support of this work.

References

[1] P.M. Singer et al., Phys. Rev. Lett. 88 (2002) 047602.
[2] J. Haase et al., J. Supercond. 15 (2002) 339.
[3] J. Bobroff et al., Phys. Rev. Lett. 89 (2002) 157002.
[4] A. Suter et al., Phys. Rev. Lett. 84 (2000) 4938.
[5] S.G. Brass, M.H. Ghandehari, Appl. Phys. Lett. 53 (1988) 22.
[6] M.S. Wu, T.T. Fang, J. Am. Ceram. Soc. 81 (1998) 1644–1654.
[7] M. Takigawa et al., Phys. Rev. Lett. 71 (1993) 2650.

2.3 The pseudogap and superconductivity

2.3.1 Concept of muon-spin rotation

Muon-spin rotation, μSR[2], is a well established method in condensed matter physics and ranks among the most powerful techniques for investigation of local magnetic fields in the bulk, *e.g.* the magnetic field distribution associated with the vortex state in a superconductor. A muon is a lepton with a rest mass 207 times that of the electron and a charge of the same magnitude, with either positive of negative sign. The spin of a muon is $I = \frac{1}{2}$ and the magnetic moment about three times larger than that of the proton. In condensed matter research μSR is most often using muons having charge $+e$.

The accelerator-based μSR research requires an intense primary beam of protons that is focused on a target of carbon or beryllium to produce pions. The pions stop just below the surface of the target and subsequently decay at rest, producing so-called surface muons with an approximate energy of $\sim 4\,\mathrm{MeV}$ and a magnetic moment antiparallel to the momentum. At the Paul Scherrer Institut (PSI), Villigen (Switzerland) the muon beam is produced with a high degree of spin polarization, since the muons to almost 100% come from pions decaying at rest.

The polarization of the spin of the muons can be rotated with a spin rotator. The muons are then guided to the sample, which is mounted in a cryostat in an external magnetic field. The muon thermalizes in the sample within typically 1 ns. Muons with positive charge stop at interstitial positions away from positively charged ions. The implantation depth depends on the momentum of the particle.

Depending on the accelerator employed, two different modes of muon spectrometry are available, known as the pulsed and the continuous beam method. In the pulsed technique, bunches of muons are simultaneously implanted in the sample, whereas in a continuous beam setup single muons are evaluated as separate events. Below we briefly describe the working principle of the continuous beam spectrometer operated at PSI (Fig. 13).

[2]Actually, R of the acronym can also stand for 'relaxation' or 'resonance'.

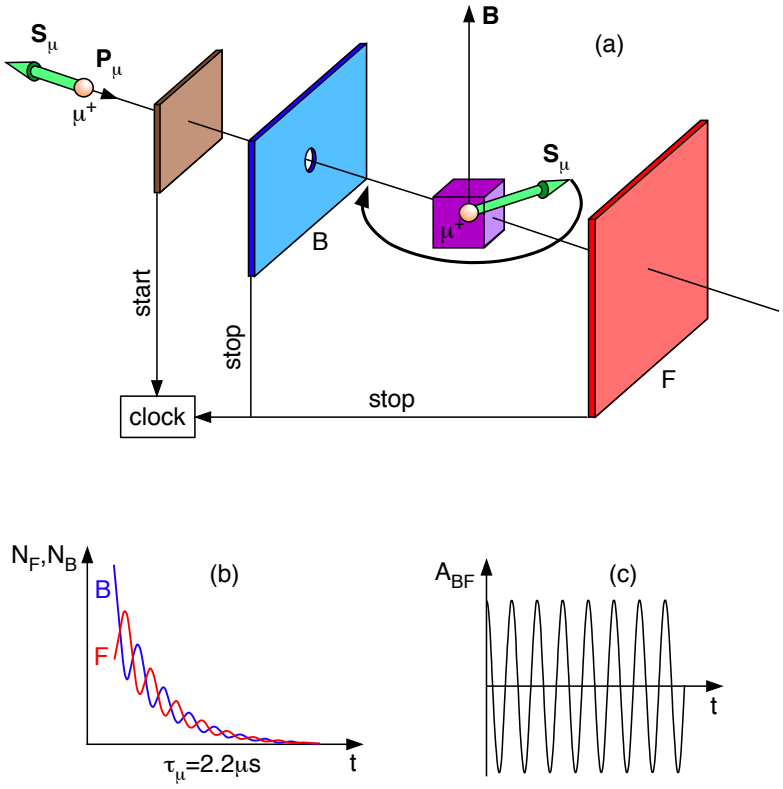

Figure 13: Principles of muon-spin rotation measurements. (a) overview of the experimental setup. Here the muon spin $\mathbf{S}_\mu$ is antiparallel to the momentum $\mathbf{P}_\mu$. The first positron detector constitutes a starting trigger, and produces, if necessary, a veto signal (see text). The backward and forward positron detectors are labeled B and F, respectively. (b) schematic diagram of the positron counts from the backward (N_B) and forward detector (N_F) as a function of time. (c) shows the asymmetry of this signal calculated according to $A_\mathrm{BF} = (N_\mathrm{F} - N_\mathrm{B})/(N_\mathrm{F} + N_\mathrm{B})$. Fourier transformation of the asymmetry signal yields the probability distribution of the internal magnetic field.

Spin-polarized muons are implanted one at a time. Often, a depolarizing degrader has to be used in standard μSR experiments to ensure maximum signal intensity from the sample. Before reaching the sample, the incident muon passes a positron detector that starts the instrument clock. Depending on the actual depolarization rate, an adequate time window has to be chosen. For measurements with cuprates in the mixed state (in low applied fields B), this window has a typical duration of 5 to 10 μs. If a second muon enters before the positron from the previous event is detected, the second event is rejected. To prevent too many vetoes, the muon rate must be optimized[3].

In the presence of a magnetic field, the moment of the implanted muon precesses with the Larmor frequency around the direction of the local magnetic field. The muon decays after a mean life time of $\tau_\mu \approx 2.2\,\mu$s, emitting a fast positron preferentially along its momentum direction, and two neutrinos. Before and behind the sample positron detectors are installed. As soon as one of the two detectors records an event, the clock is stopped and the time stored in a histogram memory for each detector separately. To accumulate the necessary statistics, many millions of positron events have to be recorded. Eventually, the histogram memory of each detector contains the number of events for the corresponding time channel, $N_\mathrm{F}(t)$ for the forward detector and $N_\mathrm{B}(t)$ for the backward detector.

Because the positron is preferentially emitted along the spin direction, the accumulated time signal oscillates with the Larmor frequency. In order to remove the exponential decay due to the finite life time of the muon, the so-called asymmetry signal $A(t)$ is calculated

$$A(t) = \frac{N_\mathrm{F}(t) - N_\mathrm{B}(t)}{N_\mathrm{F}(t) + N_\mathrm{B}(t)}. \tag{14}$$

The asymmetry signal depends on the distribution of the local fields.

μSR is routinely applied to the study of the internal field distribution associated with the vortex phase of type-II superconductors. An overview of schemes for treating μSR data and their limitations can be found in [67].

A superconductor is classified as type II, when $\kappa = \lambda/\xi > 1/\sqrt{2}$. Here κ denotes the so-called Ginzburg-Landau parameter, ξ the coherence length, and λ the magnetic penetration depth. The two characteristic lengths for superconductors will now be briefly introduced.

For a plane vacuum-to-superconductor interface with a magnetic field B applied parallel to the sample surface the magnetic penetration depth λ is defined as [68]

$$\lambda = \frac{1}{B} \int_0^\infty B(x)dx, \tag{15}$$

where B decreases with distance x from the surface into the bulk of the superconductor as the function $B(x)$, describing the exponentially decaying field due to screening effects in the bulk of a superconductor, possibly the most famous result of the London theory of superconductivity [69].

[3]For the general purpose spectrometer (GPS) @ PSI the optimum value is around 30'000 muons/ s for a 10 μs time window.

The London theory also relates the penetration depth λ to the superfluid density n_s as

$$\frac{1}{\lambda^2} = \mu_0\, e^2\, \frac{n_\mathrm{s}}{m^*}. \tag{16}$$

Here μ_0, e, and m^* denote the permeability of vacuum, the elementary electric charge, and the effective mass of the charge carrier respectively.

The coherence length ξ in the Ginzburg-Landau model [68, 70] is a measure of the distance from the surface over which the local density of superconducting charge carriers approaches its bulk value. The BCS theory [3] also yields a coherence length, defined as

$$\xi_\mathrm{BCS} = \frac{\hbar\, v_\mathrm{F}}{k_\mathrm{B} T_\mathrm{c}}. \tag{17}$$

The BCS coherence length ξ_BCS is a measure of the mean distance over which the electron-electron attraction is relevant, or in other words, it reflects the extension of a Cooper pair. It has been shown that in the limit where the coherence length is small compared to the mean free path and at low temperatures the coherence lengths in the Ginzburg-Landau theory and the BCS theory coincide [71]. The spatial variation of the internal magnetic field $B_z(x)$ and the superfluid density $n_\mathrm{s}(x)$ in the x-direction from the surface of a superconductor is shown in Fig. 14.

For a type-II superconductor it is energetically unfavorable to completely expel the

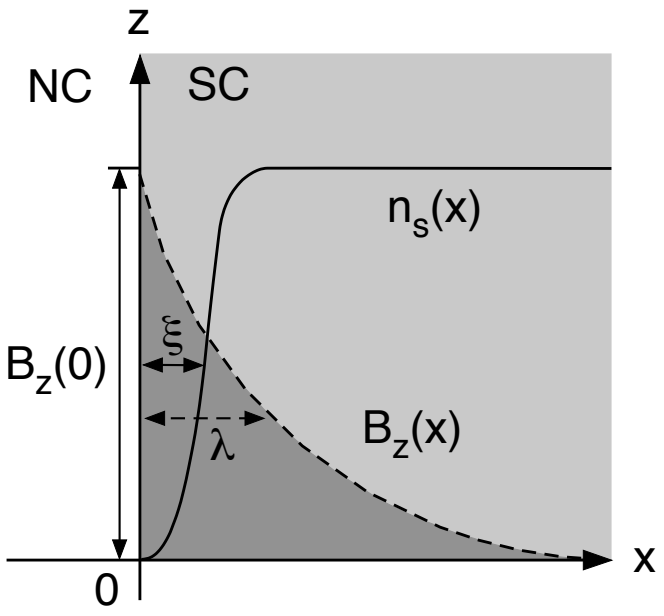

Figure 14: Sketch of the spatial variation of the superfluid density n_s and the magnetic field B_z near a normal conducting (NC) to superconducting (SC) interface at $x = 0$. The coherence length ξ and the magnetic penetration depth λ are the characteristic lengths for superconductivity.

magnetic field B from the bulk for $B_{\mathrm{c}2} > B > B_{\mathrm{c}1}$ ($B_{\mathrm{c}1}$ and $B_{\mathrm{c}2}$ denote the lower and

the upper critical field, respectively). In effect, the magnetic field penetrates the superconductor, not uniformly but in the form of vortices, each containing an elementary flux quantum $\Phi_0 = h/2e = 2.0678 \times 10^{-15}\,\mathrm{Tm}^2$ [72]. In a simplified physical picture this so-called mixed state may be described as follows: In general, for type-II superconductors ξ is much shorter than λ, meaning that from the surface of the superconductor the order parameter increases much faster (on the order of length ξ) than the magnetic field decreases (length λ). In the interface region the gain in pair condensation energy thus overcomes the screening energy, *i.e.* the surface energy is negative for type-II superconductors. The vortex formation is a consequence of the principle that the energy is minimized while the interface surface is maximized. The first vortex is created when the lower critical field is reached. As the field further increases more vortices penetrate the bulk until finally superconductivity breaks down at what is known as the upper critical field.

Vortices may be pinned, *i.e.* physically locked, to local imperfections of the crystal lattice. When the pinning forces involved are not too strong, the flux lines arrange in a triangular flux-line lattice, which in effect is a regular perforation of the superconductor with normal conducting regions that entails an internal magnetic field distribution. The actual functional form of the magnetic field distribution is characterized by λ and ξ, which is the essence of the μSR technique. These parameters may, under certain constraints, be extracted from the measured asymmetry signal, which contains information about the internal magnetic field distribution.

A distribution can be characterized by its moments. The nth moment of a distribution $P(x)$ with respect to x_0 is defined as $M_n = \int_{-\infty}^{+\infty}(x-x_0)^n P(x)dx$. A well-established procedure for extracting the magnetic penetration depth for type-II superconductors in the mixed state from measured μSR time signal is the so called second moment method. In order to implement this, the time domain signal is modeled with a set of Gaussian functions.

Let N Gaussian components describe the μSR time signal $P(t)$ due to muons stopped in the superconductor in the mixed state. A single component accounts for the background signal from muons being stopped anywhere but in the sample:

$$\begin{aligned} P(t) &= \sum_{i=1}^{N} A_i \exp(-\sigma_i^2\, t^2/2)\cos(\gamma_\mu B_i\, t + \phi) \\ &\quad + A_{\mathrm{bg}} \exp(-\sigma_{\mathrm{bg}}^2\, t^2/2)\cos(\gamma_\mu B_{\mathrm{bg}}\, t + \phi). \end{aligned} \tag{18}$$

A_i, σ_i, and B_i denote respectively the asymmetry, the depolarization rate, and the mean field of the ith Gaussian component. The index *bg* refers to the background values. The gyromagnetic ratio of the muon is $\gamma_\mu = 2\pi \times 135.5342\,\mathrm{MHz/T}$ and ϕ is the initial phase of the muon-spin ensemble.

From the time domain representation $P(t)$, the total local field distribution $P(B)$ is obtained after Fourier transforming the signal from the sample and normalizing the integral of the probability distribution to unity:

$$P(B) = \frac{\gamma_\mu}{\sqrt{2\pi}} \sum_{i=1}^{N} \frac{A_i}{\sigma_i \sum_{j=1}^{N} A_j} \exp\left(-\frac{\gamma_\mu^2 (B - B_i)^2}{2\sigma_i^2}\right). \tag{19}$$

We may now compute the first, the second, and if needed, also the third moment. The first moment represents the average field, the second moment contains information about the magnetic penetration depth λ, and the third moment may be used to determine the skewness of the distribution. The skewness yields information about the vortex lattice structure, and in particular, any change of the skewness parameter indicates structural modifications of the vortex lattice.

Calculating the first and the second moment of $P(B)$ results in respectively:

$$\langle B \rangle = \sum_{i=1}^{N} \frac{A_i B_i}{\sum_{j=1}^{N} A_j}, \tag{20}$$

and

$$\langle \Delta B^2 \rangle = \sum_{i=1}^{N} \frac{A_i}{\sum_{j=1}^{N} A_j} \left[(\sigma_i/\gamma_\mu)^2 + [B_i - \langle B \rangle]^2 \right]. \tag{21}$$

Nuclei with magnetic moments contribute $\sigma_{\rm nm}$ to the depolarization process of the muons. In order to extract from the total measured $P(B)$ the contribution $\sigma_{\rm sc}$ due to the vortex lattice alone, the additional broadening $\sigma_{\rm nm}$ is determined in the normal conducting state of the sample and subtracted according to

$$\sigma_{\rm sc} = \sqrt{\gamma_\mu^2 \langle \Delta B^2 \rangle - \sigma_{\rm nm}^2}. \tag{22}$$

From the expression for the depolarization rate due to the vortex lattice we then obtain the magnetic field penetration depth λ from [73]

$$\sigma_{\rm sc}[\mu{\rm s}^{-1}] = 4.83 \times 10^4 (1 - \langle B \rangle / B_{\rm c2})[1 + 3.9(1 - \langle B \rangle / B_{\rm c2})^2]^{\frac{1}{2}} \lambda^{-2}[{\rm nm}], \tag{23}$$

where $B_{\rm c2}$ is the upper critical field of the type-II superconductor. Eq. (23) is derived assuming an ideal hexagonal vortex lattice. A triangular vortex lattice is expected for YBCO at low fields, as was directly observed in small angle neutron scattering experiments on single crystals, see *e.g.* [74].

2.3.2 Motivation

The pseudogap is an important issue for the physics of high-temperature superconductivity. The generic phase diagram of cuprate superconductors (Fig. 1) is dominated by an antiferromagnetic, a pseudogap, and a superconducting phase, characterized by the transition temperatures $T_{\rm N}$, T^*, and $T_{\rm c}$. No consensus has been reached about the relation between the pseudogap and the superconducting state but two scenarios have been suggested. In the precursor scenario is assumed that Cooper pairs are preformed already below T^* but lack the long-range phase coherence that is established only below $T_{\rm c}$. It is further assumed that all electronic states at the Fermi surface (excluding states at the nodes but including those affected by the pseudogap) begin to form the superconducting condensate at $T_{\rm c}$. The other scenario proposes that the superconducting condensate is only due to the states that are not influenced by the opening of the pseudogap. The latter scenario thus presumes coexistence, *i.e.* that the the superconducting

and the pseudogap states are separate phenomena.

The magnetic penetration depth $\lambda(T)$ may be determined in μSR experiments. In the London model ($\lambda \gg \xi$) λ is related to the superfluid density ρ_s as $\lambda^{-2} \propto \rho_s \propto n_s/m^*$, where m^* and n_s denote the superconducting charge carrier mass and the superconducting charge carrier number density respectively. The temperature dependence of the penetration depth λ is determined by the amplitude of the superconducting energy gap and its temperature and angular dependence[4]. μSR data do not allow direct extraction of the amplitude and the exact angular dependence of the superconducting gap. By assuming d-wave superconductivity, and making an assumption about the temperature dependence of the gap, the $\lambda(T)$ can be reconstructed from a fitting procedure, which allows the gap amplitude to be obtained. For YBCO and LSCO, μSR results suggest an admixture of an s-wave component with the d-wave dominated in-plane superfluid density (Sec. 3.2). μSR experiments with $(BiPb)_2(SrLa)_2CuO_{6+\delta}$ (OP Bi2201, OP stands for optimally doped) did, however, not yield any clear evidence for multi-component superconductivity, which may well be related to the more two-dimensional nature of OP Bi2201. The OP Bi2201 μSR data was thus analyzed using a one-component superconducting d-wave order parameter.

The μSR data was also evaluated by taking the amplitude and angular dependence of the energy gap from a recent ARPES study of $(BiPb)_2(SrLa)_2CuO_{6+\delta}$, from which we calculated the expected temperature dependence of λ.

2.3.3 Experimental details

The μSR experiments were performed on single-crystalline $(BiPb)_2(SrLa)_2CuO_{6+\delta}$ with optimum doping ($T_c = 35\,K$, transition width $\sim 3\,K$). The sample growth technique is described elsewhere in detail [75]. The pseudogap in OP Bi2201 is roughly three times larger than the superconducting gap. A recent ARPES study on OP Bi2201 provides detailed information about the amplitude and the angular dependence of the energy gap [14]. Comparing these with our μSR data, we elaborate on whatever bearing the pseudogap my have on superconductivity.

The introduction of Pb atoms flattens the insulating BiO layer, which is important for ARPES studies [14]. The Pb substitution does not change T_c, but causes a decrease of the anisotropy by a factor ~ 10 to a value of 20, as torque measurements showed, meaning that the Pb substitution enhances the three-dimensional character of the compound.

The transverse-field μSR experiments were carried out using the general purpose spectrometer (GPS) at PSI. The sample was studied for temperatures down to 1.6 K and fields ranging from 5 to 640 mT, the maximum field that can be applied with the magnet at the GPS. The field was applied parallel to the c-axis of the crystals, thus probing the decay of the magnetic field in the ab-plane (λ_{ab}). The typical counting statistics were 15 to 18 million events per data point.

The μSR data were analyzed using the second-moment method with two Gaussian components, as described in Sec. 2.3.1.

[4]The superconducting energy gap is later discussed in detail (Sec. 3).

2.3.4 Results and discussion

The measured field dependence of the second moment of the local field distribution $P(B)$ is shown in Fig. 15. The solid black line was calculated using the model of Brandt [76], assuming an isotropic s-wave superconductor with $\lambda = 360$ nm and $\xi \simeq 2.6$ nm. The coherence length ξ was estimated from the upper critical field $\mu_0 H_{c2}(0) \simeq 50$ T [77]. For d-wave superconductivity, a field dependent correction of the superfluid density ρ_s due to the nonlinear response to an applied field has to be considered according to [78]

$$\frac{\rho_s(H)}{\rho_s(H=0)} = \frac{\sigma_{\rm sc}(H)}{\sigma_{\rm sc}(H=0)} = 1 - K\sqrt{H}. \tag{24}$$

Here the parameter K is a measure of the strength of the nonlinear response. Eq. (24) is valid only for $H \gg H_{c1}$, and thus only fields exceeding 40 mT were considered in the analysis. The result is shown as the red line in Fig. 15. It is evident that the observed $\sigma_{\rm sc}(\mu_0 H)$ is consistent with a leading d-wave gap.

The skewness parameter $\alpha_{\rm s}$ reflects the symmetry of the underlying vortex structure and is a sensitive measure of changes in the vortex lattice depending on the magnetic field or on the temperature [79]. From the calculated moments of the $P(B)$ distribution the skewness parameter can be derived according to $\alpha_{\rm s} = \langle \Delta B^3 \rangle^{\frac{1}{3}} \langle \Delta B^2 \rangle^{-\frac{1}{2}}$, where $\langle \Delta B^n \rangle$ is the $n^{\rm th}$ moment of $P(B)$. Compared with the expected value of 1.2 for a triangular vortex lattice with $\kappa \gg 1$, $\alpha_{\rm s}(1.6\,{\rm K}) = 0.84(2)$, *i.e.* rather much less than expected. Moreover, $\alpha_{\rm s}$ was found to be field independent within measurement uncertainty. The observed temperature independence of $\alpha_{\rm s}$ in the superconducting state indicates that for the investigated field range the symmetry of the vortex lattice does not change. The smaller than expected value of $\alpha_{\rm s}$ could be caused by microscopic field gradients due to the interaction of flux expulsion with pinning, by geometric factors due to the multi-crystal sample, or by spatial variation of λ [80].

The temperature dependence of the second moment of $P(B)$ for a field of 40 mT applied along the c-axis was also studied. The result is shown in Fig. 16. Below 20 K $\sigma_{\rm sc}(T)$ is linear, consistent with the presence of nodes in the superconducting energy gap of OP Bi2201. In order to assess possible changes in the symmetry of the vortex lattice with temperature, the temperature dependence of the skewness parameter $\alpha_{\rm s}$ was determined. It was found to be temperature independent for $T \lesssim 30$ K, from which was inferred that in this temperature range the depolarization rate $\sigma_{\rm sc}(T)$ reflects mainly $\lambda_{ab}(T)$. The sudden drop in the skewness parameter to zero above 30 K very likely indicates the melting transition of the vortex lattice.

The temperature dependence of λ can be calculated using [81]

$$\frac{\lambda_i^{-2}(T)}{\lambda_i^{-2}(0)} = 1 + \frac{1}{\pi} \int_0^{2\pi} \int_{\Delta_{\rm SC}(T,\varphi)}^{\infty} w(\varphi) \left(\frac{\partial f}{\partial E} \right) \frac{E\, dE\, d\varphi}{\sqrt{E^2 - \Delta_{\rm SC}(T,\varphi)^2}}, \tag{25}$$

with

$$\Delta_{\rm SC}(T,\varphi) = \Delta_{\rm SC}^0\, s(T/T_{\rm c})\, g(\varphi). \tag{26}$$

In Eq. (25) index i refers to any one of the crystallographic axes ($i = a, b, c$). Here $w(\varphi)$ is a non-uniform quasi-particle weight function on the Fermi surface (for a uniform quasi-particle weight: $w(\varphi) = 1$, $0 \le \varphi \le 2\pi$). In Eq. (25) $f = [\exp(E/k_{\rm B}T) + 1]^{-1}$ denotes

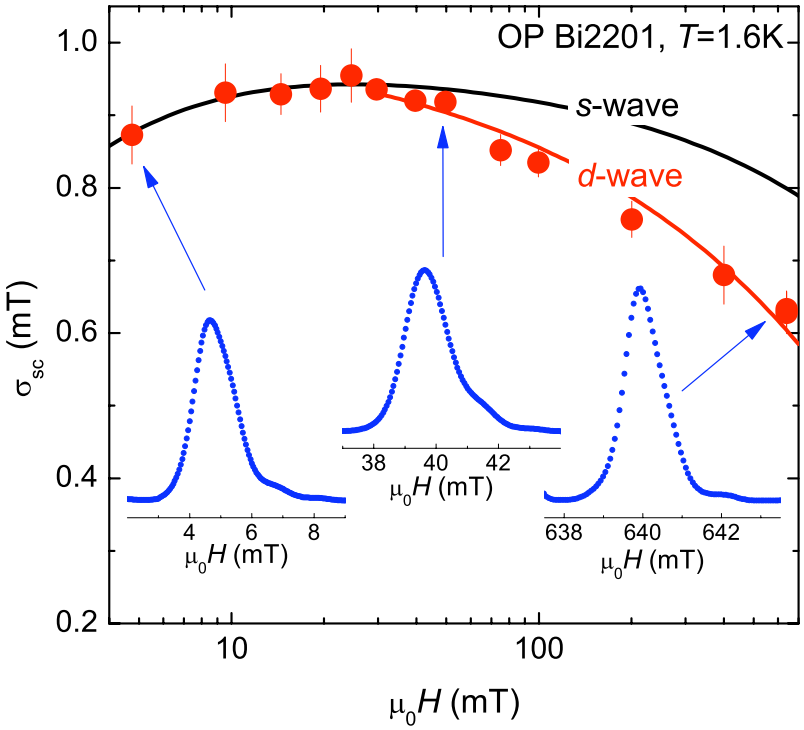

Figure 15: Magnetic field dependence of the in-plane depolarization rate σ_{sc} for optimally doped $(BiPb)_2(SrLa)_2CuO_{6+\delta}$ at 1.6 K. The solid black line results from numerical calculations using the model of Brandt [76], assuming an isotropic s-wave gap with $\lambda = 360$ nm and $\kappa = 140$. In the assumed case of d-wave superconductivity, the expected field dependence of σ_{sc} is shown by the solid red line, which takes the nonlinear response of the in-plane superfluid density into account (see text for details). Insets show examples of the local magnetic field distribution $P(B)$ are plotted for 5, 40, and 640 mT. After Paper **III** (Sec. 2.3.6).

the Fermi distribution function, and $\lambda_i(0)$ and Δ_{SC}^0 the zero-temperature values for the magnetic penetration depth and the superconducting gap respectively. In Eq. (26) $g(\varphi)$ describes the angular dependence of the gap, and $s(T/T_c)$ the temperature dependence.

The depolarization rate $\sigma_{sc}(T)$ was analyzed assuming d-wave symmetry for the superconducting gap, *i.e.* angular dependence $g(\varphi) = \cos(2\varphi)$, and a uniform quasiparticle weight at the Fermi surface $[w(\varphi) = 1]$. For the temperature dependence of the gap, $s(T/T_c) = \tanh(1.82[1.018(T_c/T - 1)^{0.51}])$ [82] was chosen. The use of the weak-coupling BCS formula for $s(T/T_c)$ is justified by direct gap measurements by means of ARPES [25] and tunneling spectroscopy [83]. Fitting $\sigma_{sc}(T)$ from Eq. (25) with $\sigma_{sc}^{-2}(T)/\sigma_{sc}^{-2}(0) = \lambda^{-2}(T)/\lambda^{-2}(0)$ yielded $\Delta_{SC}^0 = 9.7(1)$ meV $(2\Delta_{SC}^0/k_B T_c = 6.43(7))$. The amplitude and the angular dependence of the superconducting gap used in this approach are shown by the black line in Fig. 16b. Obviously $\lambda(T)$ is well described in this analysis, see the black line in Fig. 16a, but the gap behavior seems to be inconsistent with the ARPES measurements in Fig. 16b.

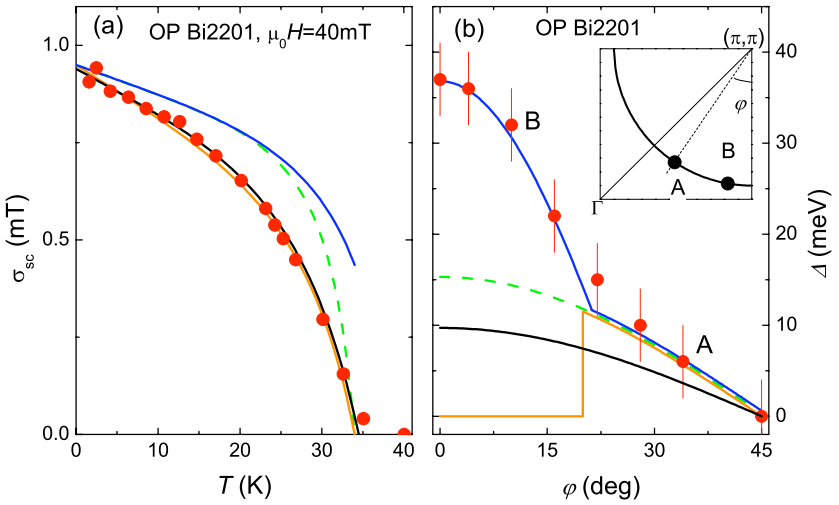

Figure 16: (a) shows the temperature dependence of the in-plane depolarization rate $\sigma_{\rm sc} \propto \lambda_{ab}^{-2}$ of $(BiPb)_2(SrLa)_2CuO_{6+\delta}$ for a field of 40 mT applied along the c-axis. The lines were obtained using Eq. (25) with various combinations of amplitudes $\Delta_{\rm SC}^0$ and angular functions $g(\varphi)$ for the energy gap [$g(\varphi) = \cos(2\varphi)$ with a uniform quasi-particle weight around the Fermi surface, and $\Delta_{\rm SC}^0 = 9.7(1)$ meV (solid black) and $\Delta_{\rm SC}^0 = 15$ meV (dashed green); $\Delta_{\rm SC}^0 = 15$ meV and $g(\varphi) = \cos(2\varphi)$ with partial suppression of the superfluid density (solid orange) and $g(\varphi) = \cos(2\varphi)$ in the nodal and $g(\varphi) = \cos(3.4\varphi)$ in the anti-nodal region (solid blue), see text for details]. (b) shows the amplitude and the angular dependence of the energy gap of OP Bi2201 as obtained from ARPES [14], and illustrates the different approaches used to analyze $\sigma_{\rm sc}(T)$ in the respective color. The inset in panel (b) shows schematically a part of the Fermi surface. The points A and B are in the near nodal and the near anti-nodal region, respectively. After Paper **IV** (Sec. 2.3.7).

We now turn to the evaluation of the μSR where we made direct use of the amplitude and the angular dependence of the energy gap determined in the ARPES measurements made on a similar sample of OP Bi2201 [14]. Three different approaches were investigated in an attempt to reproduce the in-plane $\sigma_{\rm sc}(T)$ (Fig. 16a and Fig. 16b).

(a) In the first approach, $\Delta_{\rm SC}(\varphi)$ in Eq. (25) was taken to be the dashed green line in Fig. 16b with a uniform quasi-particle weight ($w(\varphi) = 1$) assumed for the entire Fermi surface. For the green line a d-wave gap was assumed. The gap amplitude $\Delta_{\rm SC}^0$ for $T = 0$ was determined by fitting a d-wave gap expression [$g(\varphi) = \cos(2\varphi)$], using for the angular dependence of the energy gap only the ARPES data that are not affected by the pseudogap [14]. The dashed green line in Fig. 16b is thus given by $\Delta_{\rm SC}(T,\varphi) = 15\,{\rm meV} \times s(T/T_{\rm c}) \times \cos(2\varphi)$, which yields $2\Delta_{\rm SC}^0/k_{\rm B}T_{\rm c} = 9.95$. For the temperature dependence of the gap, $s(T/T_{\rm c}) = \tanh(1.82[1.018(T_{\rm c}/T - 1)^{0.51}])$ [82] was chosen. The $\sigma_{\rm sc}(T)$ calculated from this approach is shown as the dashed green line in Fig. 16a, which obviously cannot describe the μSR data consistently.

(b) In the second approach, $\Delta_{\rm SC}(\varphi)$ in Eq. (25) is taken to be the solid blue line in Fig. 16b, for which the weight function $w(\varphi) = 1$ was assumed. The blue line is an

analytical function consisting of two parts, one describing the near-nodal and the other the near anti-nodal region. For the near-nodal part $\Delta_{SC}^{0} = 15\,\mathrm{meV}$, $g(\varphi) = \cos(2\varphi)$, and $s(T/T_c)$ is the same as in the first approach. The near anti-nodal part was assumed to be temperature independent, as suggested by Raman-scattering experiments [84]. For the gap a value of $\Delta_{SC}^{0} = 36\,\mathrm{meV}$ and for $g(\varphi) = \cos(3.4\varphi)$ were used. The $\sigma_{sc}(T)$ calculated in this approach is shown as the solid blue line in Fig. 16a. It is evident that neither this approach describes the μSR data well.

(c) The third approach was identical to the first, except that now the superfluid density was assumed to be suppressed on part of the Fermi surface, as illustrated by the solid orange line in Fig. 16b. Formally, this suppression can be realized by adjusting $w(\varphi)$ according to:

$$w(\varphi) = \begin{cases} 1 & \text{if } (n \cdot 45^o - 25^o) \leq \varphi \leq n \cdot 45^o, \\ 0 & \text{else.} \end{cases}$$

where n is an integer ranging from 1 to 8. $\sigma_{sc}(T)$ calculated in this approach describes the μSR data fairly well as is seen by the solid orange line in Fig. 16a.

Fair consistency between bulk-sensitive μSR and surface-sensitive ARPES measurements is obtained in the approach, where a partial suppression of the quasi-particle weight was assumed. These findings therefore suggest that the pseudogap and the superconducting phase are dominated by different parts of the Fermi surface.

Note that both fitting procedures, the one assuming a superconducting d-wave gap with a uniform quasi-particle weight over the whole Fermi surface with $\Delta_{SC}^{0} = 9.7\,\mathrm{meV}$ (black line in Fig. 16a), and on the other using the ARPES results, assuming a superconducting d-wave gap with partial suppression of the quasi-particles on the Fermi surface and $\Delta_{SC}^{0} = 15\,\mathrm{meV}$ (orange line in Fig. 16a) describe our μSR data well.

2.3.5 Conclusions

From the field dependence of the μSR data it was found that the in-plane superfluid density shows a behavior that excludes pure isotropic s-wave superconductivity for $(BiPb)_2(SrLa)_2CuO_{6+\delta}$, but rather indicates superconductivity consistent with a dominant d-wave order parameter. The comparison of the measured temperature dependence of λ with calculations, using data from ARPES measurements suggests that the states affected by the pseudogap are not involved with the superfluid condensate. To further clarify this point, though, more experimental work is required.

2.3.6 Paper III: Evidence for competition between the superconducting and the pseudogap state in $(BiPb)_2(SrLa)_2CuO_{6+\delta}$ from muon-spin rotation experiments

This work is published in:

R. Khasanov, Takeshi Kondo, S. Strässle, D.O.G. Heron, A. Kaminski, H. Keller, S.L. Lee, and Tsunehiro Takeuchi, *Evidence for competition between the superconducting and the pseudogap state in $(BiPb)_2(SrLa)_2CuO_{6+\delta}$ from muon-spin rotation experiments*, Physical Review Letters **101**, 227002 (2008).

Abstract

The in-plane magnetic penetration depth lambdaab in optimally doped $(BiPb)_2(SrLa)_2CuO_{6+\delta}$ (OP Bi2201) was studied by means of muon-spin rotation. The measurements of $\lambda_{ab}^{-2}(T)$ are inconsistent with a simple model of a d-wave order parameter and a uniform quasiparticle weight around the Fermi surface. The data are well described assuming the angular gap symmetry obtained in ARPES experiments [Phys. Rev. Lett. 98, 267004 (2007)], which suggest that the superconducting gap in OP Bi2201 exists only in segments of the Fermi surface near the nodes. The remaining parts of the Fermi surface, which are strongly affected by the pseudogap state, do not contribute significantly to the superconducting condensate.

DOI: 10.1103/PhysRevLett.101.227002
PACS numbers: 74.72.Hs, 74.25.Jb, 76.75.+i

Evidence for a Competition between the Superconducting State and the Pseudogap State of $(BiPb)_2(SrLa)_2CuO_{6+\delta}$ from Muon Spin Rotation Experiments

R. Khasanov,[1,2,*] Takeshi Kondo,[3,4] S. Strässle,[2] D. O. G. Heron,[5] A. Kaminski,[3] H. Keller,[2] S. L. Lee,[5] and Tsunehiro Takeuchi[4,6]

[1]*Laboratory for Muon Spin Spectroscopy, Paul Scherrer Institut, CH-5232 Villigen PSI, Switzerland*
[2]*Physik-Institut der Universität Zürich, Winterthurerstrasse 190, CH-8057 Zürich, Switzerland*
[3]*Ames Laboratory and Department of Physics and Astronomy, Iowa State University, Ames, Iowa 50011, USA*
[4]*Department of Crystalline Materials Science, Nagoya University, Nagoya 464-8603, Japan*
[5]*School of Physics and Astronomy, University of St. Andrews, Fife, KY16 9SS, United Kingdom*
[6]*EcoTopia Science Institute, Nagoya University, Nagoya 464-8603, Japan*

(Received 11 June 2008; published 24 November 2008)

The in-plane magnetic penetration depth λ_{ab} in optimally doped $(BiPb)_2(SrLa)_2CuO_{6+\delta}$ (OP Bi2201) was studied by means of muon-spin rotation. The measurements of $\lambda_{ab}^{-2}(T)$ are inconsistent with a simple model of a *d*-wave order parameter and a uniform quasiparticle weight around the Fermi surface. The data are well described assuming the angular gap symmetry obtained in ARPES experiments [Phys. Rev. Lett. **98**, 267004 (2007)], which suggest that the superconducting gap in OP Bi2201 exists only in segments of the Fermi surface near the nodes. The remaining parts of the Fermi surface, which are strongly affected by the pseudogap state, do not contribute significantly to the superconducting condensate.

DOI: 10.1103/PhysRevLett.101.227002 PACS numbers: 74.72.Hs, 74.25.Jb, 76.75.+i

The relevance of the pseudogap phenomenon for superconductivity is an important open issue in the physics of high-temperature cuprate superconductors (HTS's). There are two main scenarios to be considered. In the first, the so-called ''precursor scenario'', the Cooper pairs are already formed at T^*, the temperature at which the pseudogap opens first, but long-range phase coherence is not established until the sample is cooled below the superconducting transition temperature T_c. In the second, the so-called ''two-gap'' scenario, the superconducting and the pseudogap state are not directly related with each other, and may even compete. Within this scenario the gaps in *k*-space, existing near the nodes and in the antinodal region of the Fermi surface, are due to the superconducting and the pseudogap states, respectively. This scenario gained support due to a number of recent experiments [1–5] which revealed that the antinodal gap remains unaffected as the temperature changes across T_c, and generally its magnitude increases significantly in the underdoped region, where T_c decreases. In contrast, the gap near the nodes scales with T_c and obeys a well-defined BCS temperature dependence [4]. This interpretation also agrees with recent results from scanning-tunneling-microscopy experiments [6], suggesting that the incoherent antinodal states are not responsible for the formation of phase-coherent Cooper pairs. Consequently, superconductivity is caused by the coherent part of the Fermi surface near the nodes.

Measurements of the magnetic penetration depth λ can be used to distinguish between the above described scenarios. The temperature dependence of λ is uniquely determined by the absolute maximum value of the superconducting energy gap and its angular and temperature dependence. In addition, within the London model, λ^{-2} is proportional to the superfluid density via $\lambda^{-2} \propto \rho_s \propto n_s/m^*$ and, in case where the supercarrier mass m^* is known, gives information on the supercarrier density n_s.

Here we report on a study of the in-plane magnetic penetration depth λ_{ab} in optimally doped $(BiPb)_2 \times (SrLa)_2CuO_{6+\delta}$ (OP Bi2201). This superconductor was chosen for the following reasons: (i) The angular dependence of the energy gap in similar OP Bi2201 samples was recently studied by Kondo *et al.* [3] by means of angular-resolved photoemission (ARPES); (ii) the maximum values of two spectral gaps, dominating different regions of the Fermi surface, are differ for more than a factor 3. Note that in OP Bi2212 those gaps were found to be almost the same [4]. Good agreement with the ARPES data was obtained within a model which assumes that the pseudogap affects the spectral density of the antinodal quasiparticle. Consequently, only carriers close to the nodes contribute to the superfluid density, while the weight of the coherent quasiparticle near the antinodes is negligible. This statement is also supported by comparing the zero-temperature value of $\lambda_{ab}^{-2}(0)$ for OP Bi2201 studied here with those of other OP HTS's, such as $Ca_{2-x}Na_xCuO_2Cl_2$ (OP Na-CCOC) [7] and $La_{2-x}Sr_xCuO_4$ (OP La214) [8], having similar transition temperatures. It was observed that in superconductors where the superconducting gap is developed only close to the nodes (OP Bi2201 and OP Na-CCOC) the superfluid density is more than 50% smaller than in OP La214 where the *d*-wave superconducting gap is detected on the whole Fermi surface [9].

Details on the sample preparation for OP Bi2201 single crystals can be found elsewhere [10]. The values of T_c and the width of the superconducting transition, as determined from magnetization measurements, are $\simeq$35 K and $\simeq$3 K,

respectively. The transverse-field μSR experiments were carried out at the πM3 beam line at the Paul Scherrer Institute (Villigen, Switzerland). The description of TF-μSR technique and its application to study HTS's can be found in Ref. [11]. Two OP Bi2201 single crystals with an approximate size of $4 \times 2 \times 0.1$ mm^3 were used. The sample was field cooled from above T_c to 1.6 K in a series of fields ranging from 5 to 640 mT. The magnetic field was applied parallel to the crystallographic c axis and transverse to the muon-spin polarization. The typical counting statistics were ~15–18 million muon detections per data point. In order to describe the asymmetric local magnetic field distribution $P(B)$ in the superconductor in the mixed state the analysis of the data was based on a two-component Gaussian fit of the μSR time spectra [12,13]:

$$P(t) = \sum_{i=1}^{2} A_i \exp(-\sigma_i^2 t^2/2) \cos(\gamma_\mu B_i t + \phi), \quad (1)$$

which corresponds to the field distribution:

$$P(B) = \gamma_\mu \sum_{i=1}^{2} \frac{A_i}{\sigma_i} \exp\left(-\frac{\gamma_\mu^2 (B - B_i)^2}{2\sigma_i^2}\right). \quad (2)$$

Here A_i, σ_i, and B_i are the asymmetry, the relaxation rate, and the mean field of the ith component, $\gamma_\mu = 2\pi \times 135.5342$ MHz/T denotes the muon gyromagnetic ratio, and ϕ is the initial phase of the muon-spin ensemble. The analysis was simplified to a single Gaussian line shape in the case when the two-Gaussian and the one-Gaussian fits result in comparable χ^2.

The magnetic field penetration depth λ was derived from the total second moment of $P(B)$:

$$\sigma_{\rm tot}^2 = \sum_{i=1}^{2} \frac{A_i}{A_1 + A_2} [\sigma_i^2 + \gamma_\mu^2 [B_i - \langle B \rangle]^2], \quad (3)$$

as $\lambda^{-4} \propto \sigma_{\rm tot}^2 - \sigma_{\rm nm}^2 = \sigma_{\rm sc}^2$. Here $\sigma_{\rm nm}$ is the nuclear moment contribution, $\sigma_{\rm sc}$ is the superconducting state contribution, and $\langle B \rangle$ is the first moment of $P(B)$ (see Ref. [12] for details). Since the magnetic field was applied along the crystallographic c axis, our experiments provide direct information on λ_{ab}.

Figure 1(a) shows the dependence of $\sigma_{\rm sc}$ on the applied magnetic field measured after field cooling the OP Bi2201 sample from $T > T_c$ down to 1.6 K. The $P(B)$ distributions were calculated using the maximum entropy Fourier-transform technique for $\mu_0 H = 5$, 40, and 640 mT [see Fig. 1(a)]. In the whole range of fields (5 mT $\leq \mu_0 H \leq$ 640 mT) $P(B)$ is asymmetric. The asymmetric shape of $P(B)$ is generally described by the skewness parameter $\alpha_s = \langle \Delta B^3 \rangle^{1/3} / \langle \Delta B^2 \rangle^{1/2}$ [$\langle \Delta B^n \rangle$ is the nth central moment of $P(B)$]. The variation of α_s reflects underlying changes in the vortex structure [14]. In the limit $\kappa \gg 1$ and for realistic measuring conditions $\alpha_s \simeq 1.2$ for an ideal triangular vortex lattice (VL). It is very sensitive to structural changes of the VL which can occur as a function of temperature and/or magnetic field [14,15]. Figure 1(b) implies that in

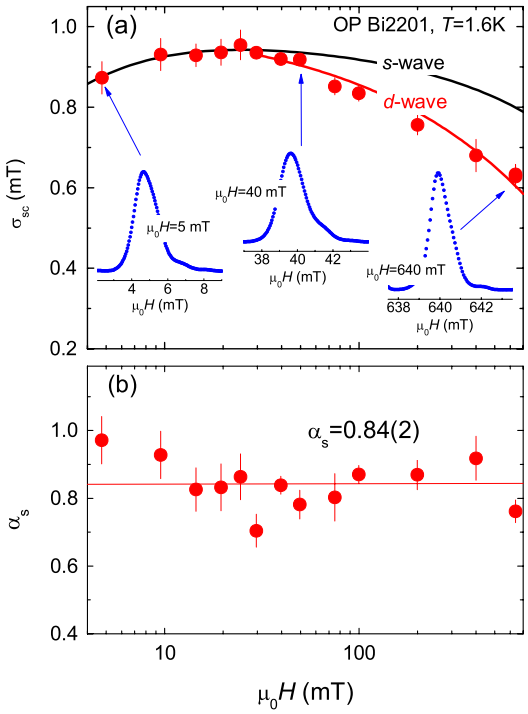

FIG. 1 (color online). (a) Dependence of $\sigma_{\rm sc}$ of OP Bi2201 on the applied magnetic field measured at $T = 1.6$ K. The black solid line corresponds to $\sigma_{\rm sc}(H)$ obtained by using the numerical calculations of Brandt [20] ($\lambda = 360$ nm, $\kappa = 140$) for a superconductor with an isotropic energy gap. The solid red line represents $\sigma_{\rm sc}(H)$ expected in case of a d-wave superconductor. The blue dotted curves show the local magnetic field distribution $P(B)$ calculated by means of the maximum entropy Fourier-transform technique at $T = 1.6$ K and $\mu_0 H = 5$, 40, and 640 mT. (b) Field dependence of the skewness parameter α_s. The solid line is the average value $\alpha_s = 0.84(2)$.

OP Bi2201 $\alpha_s(H)$ is almost constant [$\alpha_s = 0.84(2)$] and is smaller than the expected value of 1.2, which can be caused by microscopic field gradients due to interaction of flux expulsion with pinning, different geometric factors due to the range of crystal sizes and shapes, spatial variation in the penetration depth [16].

It should be noted here that addition of Pb does not change T_c and the in-plane superfluid density $\rho_s \propto \lambda_{ab}^{-2}$ [17], but makes OP Bi2201 *more* three dimensional. To estimate the anisotropy coefficient $\gamma_{c,ab} = \lambda_c / \lambda_{ab}$ (λ_c is the c-axis component of the penetration depth) we performed torque magnetization experiment on one of the crystals studied [18]. A value of $\gamma_{c,ab} \simeq 20$ was found, which is more than 10 times smaller than $\gamma_{c,ab} \simeq 200 - 400$ obtained on OP Bi2201 without Pb by Kawamata *et al.* [19].

Figure 1 indicates that $\sigma_{\rm sc}(H)$ is not monotonic: with increasing field $\sigma_{\rm sc}$ goes through the broad maximum at around 20 mT. The black solid line in Fig. 1(a), calculated within the model of Brandt [20], corresponds to $\sigma_{\rm sc}(H)$ for an isotropic s-wave superconductor with $\lambda = 360$ nm and $\kappa = \lambda / \xi \simeq 140$ ($\xi \simeq 2.6$ nm was obtained from the value of the second critical field $\mu_0 H_{c2}(0) \simeq 50$ T [21]). From

Fig. 1(a) we conclude that the experimental $\sigma_{sc}(H)$ depends much stronger on the magnetic field than expected for a fully gaped s-wave superconductor. As shown by Amin *et al.* [22] for a superconductor with nodes in the energy gap a field dependent correction to ρ_s arises from its nonlocal and nonlinear response to an applied magnetic field. The solid red line represents the result of the fit by means of the relation:

$$\frac{\rho_s(H)}{\rho_s(H=0)} = \frac{\sigma_{sc}(H)}{\sigma_{sc}(H=0)} = 1 - K\sqrt{H}, \qquad (4)$$

which takes the nonlinear correction to ρ_s for a superconductor with a d-wave energy gap into account [23]. Here the parameter K depends on the strength of the nonlinear effect. Since Eq. (4) is valid for intermediate fields $H_{c1} \ll H \ll H_{c2}$ (H_{c1} is the first critical field) only the data points above 40 mT were considered in the analysis.

We now discuss the T dependence of σ_{sc}. Figure 2 displays $\sigma_{sc}(T)$ measured at $\mu_0 H = 40$ mT. Below 20 K, σ_{sc} is linear in T as expected for a superconductor with nodes in the gap, consistent with the conclusion drawn from the analysis of the $\sigma_{sc}(H)$ data (see discussion above and Fig. 1). To ensure that $\sigma_{sc}(T)$ is determined primarily by the variance of the magnetic field within the VL we plot in Fig. 2(b) the corresponding $\alpha_s(T)$. It is constant from 1.6 K to $\simeq$27 K and drops to zero at $T \simeq 30$ K, where $P(B)$ becomes fully symmetric. A similarly sharp change of α_s with temperature was observed in Bi2212 and was explained by VL melting [14,15]. Correspondingly, we conclude that for temperatures $0 < T \lesssim 30$ K the T variation of σ_{sc} reflects the *intrinsic* behavior of the in-plane magnetic penetration depth λ_{ab}.

The T dependence of σ_{sc} was analyzed by assuming that the angular dependence of the energy gap in OP Bi2201 is similar to the one from recent ARPES experiments [3] [see Fig. 3(a)]. In analogy with Refs. [3,4] it was also assumed that the energy gap in the nodal region changes with temperature in accordance with the weak-coupling BCS prediction $\tilde{\Delta}(T/T_c) = \tanh\{1.82[1.018(T_c/T - 1)^{0.51}]\}$ [24], while the one near the antinodes is T independent [see the corresponding lines "A" and "B" in Fig. 3(b)]. The following cases were considered: (I) a monotonic d-wave gap $\Delta(T, \varphi) = 15\ \text{meV}\cos(2\varphi)\tilde{\Delta}(T/T_c)$ (green dashed line); (II) a monotonic d-wave gap with suppressed quasiparticle weight in the antinodal region (solid orange line); (III) an analytical function, which follows the monotonic d wave $15\ \text{meV}\cos(2\varphi)\tilde{\Delta}(T/T_c)$ in the nodal region and changes to a $36\ \text{meV}\cos(3.4\varphi)$ behavior close to the antinodes (solid blue line). The T dependence of λ_{ab}^{-2} was calculated within the local (London) approximation ($\lambda \gg \xi$) using the following equation [13]:

$$\frac{\sigma_{sc}(T)}{\sigma_{sc}(0)} = 1 + \frac{8}{\pi - 4\varphi_0}\int_{\varphi_0}^{\pi/4}\int_{\Delta(T,\varphi)}^{\infty}\left(\frac{\partial f}{\partial E}\right) \times \frac{E dE d\varphi}{\sqrt{E^2 - \Delta(T,\varphi)^2}}. \qquad (5)$$

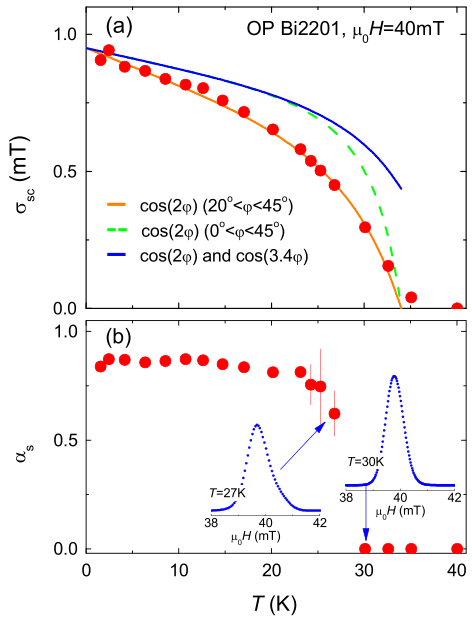

FIG. 2 (color online). (a) Dependence of σ_{sc} of OP Bi2201 on T measured at $\mu_0 H = 40$ mT. Lines represent the theoretical $\sigma_{sc}(T)$ curves obtained by assuming different symmetries of the superconducting energy gap [see Fig. 3(a)]. The errors in σ_{sc} are smaller than the size of data points. (b) Dependence of the skewness parameter α_s on T. The blue dotted curves represent $P(B)$ distributions below ($T = 27$ K) and above ($T = 30$ K) the VL melting temperature.

$f = [1 + \exp(E/k_B T)]^{-1}$ denotes the Fermi function. Here we also replace the prefactor $8/\pi$ of the integral with $8/(\pi - 4\varphi_0)$ to account for the case when the superconducting energy gap is developed only on a part of the

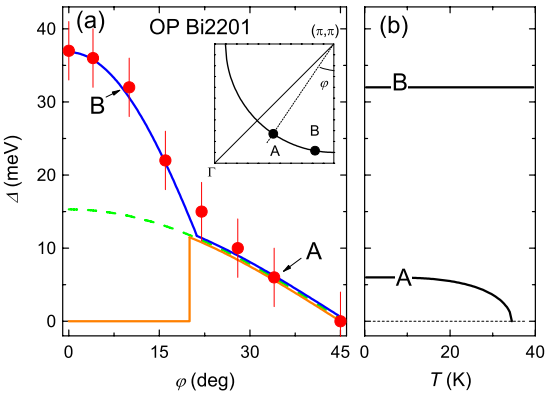

FIG. 3 (color online). (a) Angular dependence of the energy gap of OP Bi2201 obtained in ARPES experiments [3]. Lines represent the various models of the gap symmetries used to analyze the experimental $\sigma_{sc}(T)$ data [see Fig. 2(a)]. The inset shows schematically a part of the Fermi surface. The points "A" and "B" are close to the nodal ($\varphi \sim 45°$) and the antinodal ($\varphi \sim 0°$) region, respectively. (b) Temperature dependence of the energy gap in the nodal (curve A) and the antinodal (curve B) regions.

TABLE I. Transition temperature T_c, zero-temperature in-plane magnetic penetration depth $\lambda_{ab}^{-2}(0)$, and angular region where the superconducting d-wave gap is observed for OP Bi2201 (Ref. [3]), OP Na-CCOC (Refs. [6,7]), and OP La241 (Refs. [8,9]).

Compound	T_c (K)	$\lambda_{ab}^{-2}(0)$ (μm^{-2})	SC gap region
OP Bi2201	35	7.8(3)	$20° \lesssim \varphi < 45°$
OP Na-CCOC	28	10.0	$20° \lesssim \varphi < 45°$
OP La214	36	15.0	$0° \leq \varphi < 45°$

Fermi surface (in our case from φ_0 to $\pi/4$). The results of this analysis are presented in Fig. 2(a). The monotonic d-wave gap as well as the combined gap represented by the solid blue line in Fig. 3(a) cannot describe the experimental $\sigma_{sc}(T)$. Full consistency between ARPES and μSR data is obtained if one assumes a superconducting d-wave gap with only carriers in the region $20° \lesssim \varphi < 45°$ contributing to the superfluid [see Fig. 3(a)]. It should be noted here that the theoretical $\sigma_{sc}(T)$ curves in Fig. 2 were not fitted, but obtained directly by introducing the angular dependence of the gap measured in ARPES experiments into Eq. (5), describing the T dependence of the penetration depth within the London approach.

Next we compare the zero-temperature values of $\lambda_{ab}^{-2}(0) \propto n_s/m^*$ for various OP HTS's having comparable T_c values and for which the angular dependence of the superconducting gap was measured [3,6,9]. OP La214, which exhibits a fully developed superconducting gap, has an approximately 50% higher value of the superfluid density as compared to both OP Na-CCOC and OP Bi2201, having the superconducting gap opened only on a limited part of the Fermi surface (see Table I). Assuming that the supercarrier masses m^* are the same for all OP compounds listed in Table I (in analogy with $m^* \simeq 3 - 4m_e$ reported for La214 and $YBa_2Cu_3O_{7-\delta}$ families of HTS's [25]), the difference in the values of $\lambda_{ab}^{-2}(0)$ can be naturally explained by the different number of carriers condensed into the superfluid. In the case of OP Bi2201 and OP Na-CCOC, n_s is strongly reduced because of the fraction of the states is no more available for the superconducting condensate due to the pseudogap.

To conclude, the in-plane magnetic penetration depth λ_{ab} in optimally doped Bi2201 was studied by means of muon-spin rotation. By comparing the measured $\lambda_{ab}^{-2}(T)$ with the one calculated theoretically using a model consistent with ARPES measurement [3] we found that the superconducting gap in OP Bi2201 has d-wave symmetry, but only carriers from parts of the Fermi surface close to the node ($20° \lesssim \varphi \lesssim 45°$) contribute to the superfluid. This implies that the pseudogap affects the spectral density of the quasiparticles and, consequently, not all the states at the Fermi surface are available to participate in the superconducting condensate. Our results supports the scenario where the superconducting and pseudogap state are two distinct and competing phenomena. This statement is also consistent with the fact that the superfluid density in OP Bi2201 is strongly reduced in comparison with that in OP La214, where the superconducting gap and coherent quasiparticles are observed along the whole Fermi surface ($0° \leq \varphi < 45°$) [9].

This work was performed at the Swiss Muon Source (SμS), Paul Scherrer Institute (PSI, Switzerland). The authors are grateful to Y. J. Uemura and R. Prozorov for stimulating discussions, and S. Weyeneth for performing torque experiments. This work was supported by the K. Alex Müller Foundation and in part by the Swiss National Science Foundation. Work at the Ames Laboratory was supported by the Department of Energy-Basic Energy Sciences under Contract No. DE-AC02-07CH11358.

*rustem.khasanov@psi.ch

[1] M. Le Tacon *et al.*, Nature Phys. **2**, 537 (2006).
[2] K. Tanaka *et al.*, Science **314**, 1910 (2006).
[3] T. Kondo *et al.*, Phys. Rev. Lett. **98**, 267004 (2007).
[4] W. S. Lee *et al.*, Nature (London) **450**, 81 (2007).
[5] W. Guyard *et al.*, Phys. Rev. B **77**, 024524 (2008).
[6] T. Hanaguri *et al.*, Nature Phys. **3**, 865 (2007).
[7] R. Khasanov *et al.*, Phys. Rev. B **76**, 094505 (2007).
[8] C. Panagopoulos *et al.*, Phys. Rev. B **60**, 14617 (1999).
[9] M. Shi *et al.*, Phys. Rev. Lett. **101**, 047002 (2008).
[10] T. Kondo *et al.*, J. Electron Spectrosc. Relat. Phenom. **137–140**, 663 (2004); T. Kondo *et al.*, Phys. Rev. B **72**, 024533 (2005).
[11] J. E. Sonier, J. H. Brewer, and R. F. Kiefl, Rev. Mod. Phys. **72**, 769 (2000).
[12] R. Khasanov *et al.*, Phys. Rev. B **73**, 214528 (2006).
[13] R. Khasanov *et al.*, Phys. Rev. Lett. **98**, 057007 (2007).
[14] S. L. Lee *et al.*, Phys. Rev. Lett. **71**, 3862 (1993).
[15] C. M. Aegerter *et al.*, Phys. Rev. B **57**, 1253 (1998).
[16] T. M. Riseman *et al.*, Phys. Rev. B **52**, 10569 (1995).
[17] P. L. Russo *et al.*, Phys. Rev. B **75**, 054511 (2007).
[18] S. Weyeneth (to be published).
[19] S. Kawamata *et al.*, J. Low Temp. Phys. **117**, 891 (1999).
[20] E. H. Brandt, Phys. Rev. B **68**, 054506 (2003).
[21] Y. Wang *et al.*, Science **299**, 86 (2003).
[22] M. H. S. Amin, M. Franz, and I. Affleck, Phys. Rev. Lett. **84**, 5864 (2000).
[23] I. Vekhter, J. P. Carbotte, and E. J. Nicol, Phys. Rev. B **59**, 1417 (1999).
[24] A. Carrington and F. Manzano, Physica (Amsterdam) **385C**, 205 (2003).
[25] W. J. Padilla *et al.*, Phys. Rev. B **72**, 060511 (2005).

2.3.7 Paper IV: Superfluid density and angular dependence of the energy gap in optimally doped $(BiPb)_2(SrLa)_2CuO_{6+\delta}$

This work is published in:

S. Strässle, R. Khasanov, Takeshi Kondo, D.O.G. Heron, A. Kaminski, H. Keller, S.L. Lee, and Tsunehiro Takeuchi, *Superfluid density and angular dependence of the energy gap in optimally doped (BiPb)$_2$(SrLa)$_2$CuO$_{6+\delta}$*, accepted for publication in Journal of Superconductivity and Novel Magnetism.

Abstract

We present a muon-spin rotation study of the optimally doped cuprate superconductor $(BiPb)_2(SrLa)_2CuO_{6+\delta}$. The measured magnetic field dependence of the in-plane magnetic penetration λ_{ab} suggests superconductivity with a dominant d-wave order parameter. The comparison of the temperature dependence of λ_{ab} with calculations, assuming the angular gap symmetry as obtained from photoemission measurements, is consistent with a partial suppression of the quasi-particle weight toward the anti-nodal region of the Fermi surface. This suggests that the superconducting and the pseudogap state are dominated by different parts of the Fermi surface.

Keywords: muon-spin rotation experiments, cuprates, suppressed superfluid density, superconducting gap, pseudogap

DOI: 10.1007/s10948-008-0395-z

J Supercond Nov Magn
DOI 10.1007/s10948-008-0395-z

ORIGINAL PAPER

Superfluid Density and Angular Dependence of the Energy Gap in Optimally Doped $(BiPb)_2(SrLa)_2CuO_{6+\delta}$

S. Strässle · R. Khasanov · T. Kondo · D.O.G. Heron · A. Kaminski · H. Keller · S.L. Lee · T. Takeuchi

Received: 3 November 2008 / Accepted: 5 November 2008

Abstract We present a muon-spin rotation study of the optimally doped cuprate superconductor $(BiPb)_2(SrLa)_2CuO_{6+\delta}$. The measured magnetic field dependence of the in-plane magnetic penetration λ_{ab} suggests superconductivity with a dominant d-wave order parameter. The comparison of the temperature dependence of λ_{ab} with calculations, assuming the angular gap symmetry as obtained from photoemission measurements, is consistent with a partial suppression of the quasi-particle weight towards the anti-nodal region of the Fermi surface. This suggests that the superconducting and the pseudogap state are dominated by different parts of the Fermi surface.

S. Strässle (✉) · H. Keller
Physik–Institut der Universität Zürich, Universität Zürich, 8057 Zürich, Switzerland
e-mail: simon.straessle@physik.uzh.ch

R. Khasanov
Laboratory for Muon Spin Spectroscopy, Paul Scherrer Institut, 5232 Villigen PSI, Switzerland

T. Kondo · A. Kaminski
Ames Laboratory and Department of Physics and Astronomy, Iowa State University, Ames, IA 50011, USA

T. Kondo · T. Takeuchi
Department of Crystalline Materials Science, Nagoya University, Nagoya 464-8603, Japan

D.O.G. Heron · S.L. Lee
School of Physics and Astronomy, University of St. Andrews, Fife, KY16 9SS, UK

T. Takeuchi
EcoTopia Science Institute, Nagoya University, Nagoya 464-8603, Japan

Keywords Muon-spin rotation experiments · Cuprates · Suppressed superfluid density · Superconducting gap · Pseudogap

1 Introduction

An important open question in cuprate physics is the relevance of the pseudogap phenomenon for the occurrence of high-temperature superconductivity. The generic phase diagram of cuprate superconductors is determined by an antiferromagnetic, a pseudogap, and a superconducting phase, which are characterized by their respective transition temperatures T_N, T^*, and T_c. Below T^* the pseudogap state emerges and the density of states at the Fermi level is decreased. Below T_c the superconducting state appears. In the case that the pseudogap is a precursor phenomenon of superconductivity, long-range phase coherence will be established only below T_c and all electronic states, including those affected by the occurrence of the pseudogap, begin to form the superconducting condensate. In other words, all electronic states over the whole Fermi surface, except for those at the nodes, contribute to superconductivity. However, a second possible scenario is that the superconducting condensate is formed only by those states which are not influenced by the opening of the pseudogap.

Various experiments support the latter scenario [1–6]. Angle resolved photoemission spectroscopy (ARPES) [3, 4] reveals that the energy gap which opens at T_c exhibits point nodes along the diagonal of the Cu–O bond, consistent with dominant d-wave superconductivity. Furthermore, it was shown that the pseudogap appears below T^* and develops gradually to its maximum value towards the anti-nodal region of the Fermi arc, whereas it vanishes in a region near

Published online: 25 November 2008

the nodes. In recent Raman-scattering experiments, an almost temperature independent anti-nodal gap in underdoped cuprates was found below T^* [5]. In contrast to that, the energy gap in the near-nodal region opens below T_c and follows a well-defined BCS temperature dependence [4]. In addition, the near-nodal gap scales with T_c [4], whereas the anti-nodal gap size increases in general when lowering the doping in the underdoped regime [5]. These experimental observations suggest that the pseudogap and the superconducting state are coexisting phenomena, which may arise from different parts of the Fermi surface.

Muon-spin rotation (μSR) experiments allow to deduce the magnetic penetration depth λ, which is related to the superfluid density as $\lambda^{-2} \propto \rho_s \propto n_s/m^*$, where m^* and n_s denote the supercarrier mass and density, respectively. This relation is valid within the London model ($\lambda \gg \xi$). The temperature dependence of λ is determined by the amplitude of the superconducting energy gap and its temperature and angular dependence. It is not possible to reconstruct the amplitude and the exact angular dependence directly from μSR data. However, by assuming d-wave superconductivity, $\lambda(T)$ can be reconstructed. This reconstruction yields a gap value. ARPES measurements provide the amplitude and the angular dependence of the energy gap. By comparing bulk-sensitive μSR and surface-sensitive ARPES [3] experiments, different gap scenarios were tested. We find consistency between data of these two methods obtained for optimally doped $(BiPb)_2(SrLa)_2CuO_{6+\delta}$ by assuming that superconductivity is caused only by states from the near-nodal part of the Fermi surface, i.e. that the anti-nodal states affected by the pseudogap do not participate in the superconducting condensate. The main results of this contribution are published in [7].

2 Experimental Details

The μSR experiments were conducted on Pb- and Sr-doped single-crystalline $(BiPb)_2(SrLa)_2CuO_{6+\delta}$ at optimum doping (OP Bi2201) with $T_c = 35\,\mathrm{K}$ and a transition width $\sim 3\,\mathrm{K}$. The sample preparation is described elsewhere [8, 9]. Exchanging Bi partially for Pb does not change T_c, but removes partially the buckling of the insulating BiO layer, which is relevant for ARPES studies [3]. The doping level is controlled by the relative amount of Sr and La.

OP Bi2201 is an ideal compound to investigate the connection between the superconducting and the pseudogap phase by means of μSR for the following reasons. First, recent ARPES studies provide detailed information on the amplitude and the angular dependence of the energy gap of OP Bi2201 [3]. Furthermore, a large difference between the two involved energy scales is advantageous, and the pseudogap size in OP Bi2201 is roughly three times larger than the superconducting one.

The transverse-field μSR experiments were carried out at the Paul Scherrer Institute (Villigen, Switzerland). Technical details of this method can be found in [10]. Two OP Bi2201 crystals with an approximate size of $4 \times 2 \times 0.1\,\mathrm{mm}^3$ were field-cooled to 1.6 K in fields ranging from 5 to 640 mT. The field was applied along the c axis of the crystals, thus probing the decay of the magnetic field within the ab-plane (λ_{ab}). The μSR time spectra were analyzed by a two-component Gaussian approximation [7, 11, 12]:

$$P(t) = \sum_{i=1}^{2} A_i \exp\bigl(-\sigma_i^2 t^2/2\bigr) \cos(\gamma_\mu B_i t + \phi), \tag{1}$$

from which the internal magnetic field distribution $P(B)$ of the superconductor in the mixed state was obtained by Fourier transformation:

$$P(B) = \gamma_\mu \sum_{i=1}^{2} \frac{A_i}{\sigma_i} \exp\left(- \frac{\gamma_\mu^2 (B - B_i)^2}{2\sigma_i^2} \right). \tag{2}$$

A_i, σ_i, and B_i denote the asymmetry, the relaxation rate, and the mean field of the ith component, $\gamma_\mu = 2\pi \times 135.5342\,\mathrm{MHz/T}$ is the muon gyromagnetic ratio, and ϕ is the initial phase of the muon-spin ensemble.

λ_{ab} was derived from $P(B)$ within the second-moment model [7, 11, 12]:

$$\sigma_{\mathrm{tot}}^2 = \sum_{i=1}^{2} \frac{A_i}{A_1 + A_2} \bigl[\sigma_i^2 + \gamma_\mu^2 \bigl[B_i - \langle B \rangle\bigr]^2\bigr], \tag{3}$$

where $\lambda_{ab}^{-4} \propto \sigma_{\mathrm{tot}}^2 - \sigma_{\mathrm{nm}}^2 = \sigma_{\mathrm{sc}}^2$. σ_{nm} is the additional relaxation rate due to the nuclear moments, σ_{sc} is the superconducting state contribution, and $\langle B \rangle$ is the first moment of $P(B)$.

3 Results and Discussion

The field dependence of the second moment of $P(B)$ measured at 1.6 K is depicted in Fig. 1. The solid black line was calculated using the model of Brandt [13], assuming an isotropic s-wave superconductor with $\lambda = 360$ nm and $\xi \simeq 2.6$ nm. The coherence length ξ was estimated from the second critical field $\mu_0 H_{c2}(0) \simeq 50$ T [14]. In the case that the superconducting gap possesses nodes, a field dependent correction to the superfluid density ρ_s due to its nonlinear and nonlocal response to the applied field has to be taken into account [15]. The nonlinear response of a d-wave superconductor is given by [16, 17]

$$\frac{\rho_s(H)}{\rho_s(H=0)} = \frac{\sigma_{\mathrm{sc}}(H)}{\sigma_{\mathrm{sc}}(H=0)} = 1 - K\sqrt{H}. \tag{4}$$

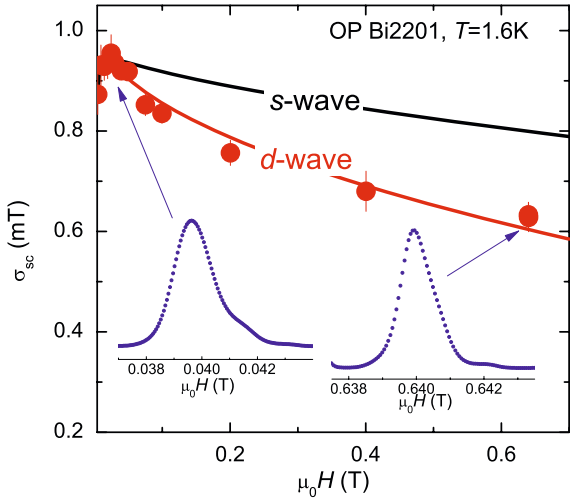

Fig. 1 (Color online) Magnetic field dependence of the in-plane $\sigma_{sc} \propto \lambda_{ab}^{-2}$ of $(BiPb)_2(SrLa)_2CuO_{6+\delta}$ at 1.6 K. The *solid black line* results from numerical calculations using the model of Brandt [13], assuming an isotropic s-wave gap and $\lambda = 360$ nm and $\xi = 2.6$ nm. For a d-wave superconductor the expected field dependence of σ_{sc} is represented by the *solid red line*, which includes a correction due to the nonlinear response of the in-plane superfluid density (see text). Examples of the asymmetric local magnetic field distribution $P(B)$ are plotted for 40 and 640 mT

The parameter K measures the strength of the nonlinear response. Since (4) is valid for $H \gg H_{c1}$, only fields exceeding 40 mT were considered in the fit, which is represented by the red line in Fig. 1. The skewness parameter is derived from the second and the third moment of $P(B)$ according to $\alpha_s = \langle \Delta B^3 \rangle^{\frac{1}{3}} \langle \Delta B^2 \rangle^{-\frac{1}{2}}$ [18] ($\langle \Delta B^n \rangle$ is the nth moment of $P(B)$). $\alpha_s(1.6\,\mathrm{K})$ was found to be field independent within error. Moreover, $\alpha_s = 0.84(2)$ is smaller than the expected value of 1.2 for a triangular vortex lattice and $\kappa \gg 1$ [7]. The field independence of α_s ensures that no symmetry change of the vortex lattice takes place in the investigated field range. The magnetic field dependence of the in-plane $\sigma_{sc} \propto \lambda_{ab}^{-2}$ shows consistency with a leading d-wave gap (see Fig. 1).

The temperature dependence of the second moment of $P(B)$ for a field of 40 mT applied along the c-axis was studied (see Fig. 2(a)). Note that, below 20 K, $\sigma_{sc}(T)$ shows a linear behavior, consistent with the previous finding that there exist nodes in the gap of OP Bi2201.

The temperature dependence of λ can be calculated using [12]

$$\frac{\lambda_i^{-2}(T)}{\lambda_i^{-2}(0)} = 1 + \frac{1}{\pi} \int_0^{2\pi} \int_{\Delta(T,\varphi)}^{\infty} w(\varphi) \times \left(\frac{\partial f}{\partial E} \right) \frac{E\, dE\, d\varphi}{\sqrt{E^2 - \Delta(T,\varphi)^2}}, \quad (5)$$

with

$$\Delta(T,\varphi) = \Delta^0 \times s(T/T_c) \times g(\varphi). \quad (6)$$

i refers to the crystallographic axis ($i = a, b, c$). With the quasi-particle weight function $w(\varphi)$ a non-uniform quasi-particle weight around the Fermi surface can be introduced (for a uniform quasi-particle weight: $w(\varphi) = 1$, $0 \le \varphi \le 2\pi$). $f = [\exp(E/k_BT) + 1]^{-1}$ denotes the Fermi distribution function, and $\lambda_i(0)$ and Δ^0 are the zero-temperature values of the magnetic penetration depth and the superconducting gap, respectively. In (6), $g(\varphi)$ describes the angular dependence of the gap, whereas $s(T/T_c)$ describes its temperature dependence.

First, $\sigma_{sc}(T)$ was analyzed assuming d-wave symmetry of the superconducting gap [$g(\varphi) = \cos(2\varphi)$] and a uniform quasi-particle weight around the Fermi surface [$w(\varphi) = 1$]. For the temperature dependence of the gap, $s(T/T_c) = \tanh(1.82[1.018(T_c/T - 1)^{0.51}])$ [19] was taken. To use the weak-coupling BCS formula for $s(T/T_c)$ is justified by direct gap measurements by means of ARPES [4] and tunneling spectroscopy [20]. By fitting the $\sigma_{sc}(T)$ using (5), $\Delta^0 = 9.7(1)$ meV was found [$2\Delta^0/k_BT_c = 6.43$]. The amplitude and the angular dependence of the superconducting gap used in this approach are illustrated by the black line in Fig. 2(b). Obviously, $\lambda(T)$ is well described by this analysis, see black line in Fig. 2(a), but the gap behavior seems to be inconsistent with the ARPES measurements shown in Fig. 2(b).

In a further step, we analyzed our μSR data by directly introducing the amplitude and the angular dependence of the energy gap from ARPES measurements (see Fig. 2(b)) on a similar sample of OP Bi2201 [3]. Three different approaches were evaluated to reproduce the in-plane $\sigma_{sc}(T)$ (see Fig. 2(a)) using the ARPES data (see Fig. 2(b)).

(a) In the first approach, $\Delta(\varphi)$ in (5) is given by the dashed green line in Fig. 2(b). Here, a uniform quasi-particle weight around the Fermi surface is assumed, i.e. $w(\varphi) = 1$. The green line assumes a d-wave gap. The gap amplitude Δ^0 is determined by fitting a d-wave gap expression [$g(\varphi) = \cos(2\varphi)$] considering only those ARPES data points of the energy gap's angular dependence, which are not affected by the pseudogap phenomenon [3]. Thus, $\Delta(T,\varphi) = 15\,\mathrm{meV} \times s(T/T_c) \times \cos(2\varphi)$ [$2\Delta^0/k_BT_c = 9.95$]. For the temperature dependence of the gap, $s(T/T_c) = \tanh(1.82[1.018(T_c/T - 1)^{0.51}])$ [19] was taken. $\sigma_{sc}(T)$ calculated within this approach is shown as a dashed green line in Fig. 2(a). Obviously, the dashed green line cannot describe the μSR data.

(b) In the second approach, $\Delta(\varphi)$ in (5) is given by the solid blue line in Fig. 2(b). $w(\varphi) = 1$ was assumed. The blue line is an analytical function consisting of two parts,

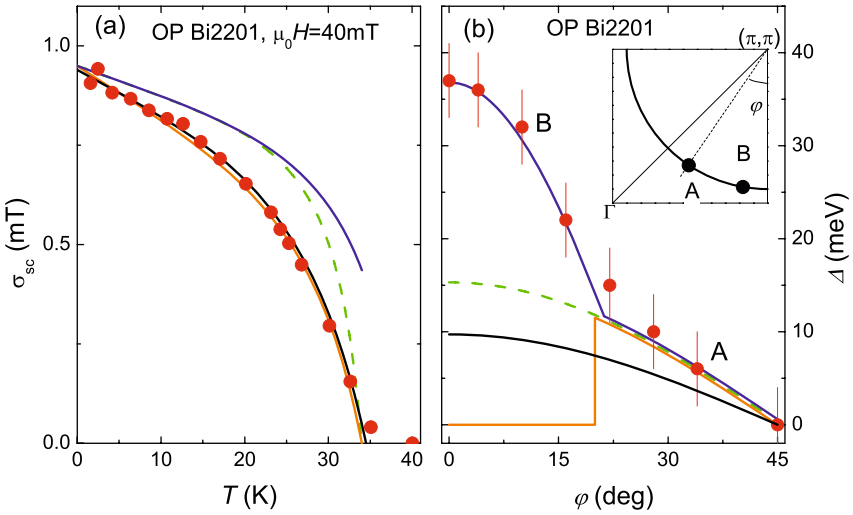

Fig. 2 (Color online) **a** Shows the temperature dependence of the in-plane $\sigma_{sc} \propto \lambda_{ab}^{-2}$ of $(BiPb)_2(SrLa)_2CuO_{6+\delta}$ for a field of 40 mT applied along the *c*-axis. The *lines* are obtained using (5) and different amplitude Δ^0 and angular dependence $g(\varphi)$ values of the energy gap [$g(\varphi) = \cos(2\varphi)$ with a uniform quasi-particle weight around the Fermi surface with $\Delta^0 = 9.7(1)$ meV (*solid black*) and $\Delta^0 = 15$ meV (*dashed green*), $g(\varphi) = \cos(2\varphi)$ with partial suppression of the superfluid density (*solid orange*), and $g(\varphi) = \cos(2\varphi)$ in the nodal and $g(\varphi) = \cos(3.4\varphi)$ in the anti-nodal region (*solid blue*), see text for more details]. **b** Shows the amplitude and the angular dependence of the energy gap of OP Bi2201 as obtained from ARPES [3], and illustrates the different approaches used to analyze $\sigma_{sc}(T)$ in the appropriate color. The *inset* in **b** shows schematically a part of the Fermi surface. The points A and B are in the near nodal and the near anti-nodal region, respectively

one describing the near-nodal and the other the near anti-nodal region. For the near-nodal part, $\Delta^0 = 15$ meV, $g(\varphi) = \cos(2\varphi)$, and $s(T/T_c) = \tanh(1.82[1.018(T_c/T - 1)^{0.51}])$ [19] was taken. The near anti-nodal part was assumed to be temperature independent, as suggested by Raman-scattering experiments [5]. Furthermore, $\Delta^0 = 36$ meV and $g(\varphi) = \cos(3.4\varphi)$ were taken. The $\sigma_{sc}(T)$ calculated within this approach is shown as a solid blue line in Fig. 2(a). It is evident that also this approach cannot describe the μSR data.

(c) The third approach is the same as approach (a), except that here the superfluid density is assumed to be suppressed on a part of the Fermi surface, and is illustrated by the solid orange line in Fig. 2(b). Technically, this suppression can be realized by adjusting $w(\varphi)$ according to:

$$w(\varphi) = \begin{cases} 1 & \text{if } (n \cdot 45^\circ - 25^\circ) \le \varphi \le n \cdot 45^\circ, \\ 0 & \text{else.} \end{cases}$$

Here, n is an integer ranging from 1 to 8. $\sigma_{sc}(T)$ calculated within this approach describes the μSR data rather well and is shown as a solid orange line in Fig. 2(a).

Full consistency between bulk-sensitive μSR and surface-sensitive ARPES measurements is obtained in the last approach (c), where a partial suppression of the quasi-particle weight was assumed. These findings therefore suggest that the pseudogap and the superconducting phase are dominated by different parts of the Fermi surface.

Note that both, the fitting procedure assuming a superconducting *d*-wave gap with a uniform quasi-particle weight over the whole Fermi surface with $\Delta^0 = 9.7$ meV (black line in Fig. 2(a)) and also the calculation using ARPES results assuming a superconducting *d*-wave gap with a partial suppression of the quasi-particles on the Fermi surface with $\Delta^0 = 15$ meV (orange line in Fig. 2(a)), describe our μSR data well.

4 Conclusions

From the field dependence of the μSR data it was found that the in-plane superfluid density shows a behavior which excludes isotropic *s*-wave superconductivity for $(BiPb)_2(SrLa)_2CuO_{6+\delta}$ but shows consistency with superconductivity with a dominant *d*-wave order parameter. The comparison of the measured temperature dependence of λ with calculation using recent ARPES measurements on a similar sample of the same compound suggests that the states affected by the pseudogap do not participate in the superfluid condensate. To further clarify this point, more experimental work is required.

Acknowledgements This work was performed at the Swiss Muon Source (SμS), Paul Scherrer Institute (Villigen, Switzerland). The authors are grateful to Y.J. Uemura and R. Prozorov for stimulating discussions. The support of the K. Alex Müller Foundation, the Swiss National Science Foundation, and the European CoMePhS Project

is acknowledged. Work at the Ames Laboratory was supported by the Department of Energy—Basic Energy Sciences under Contract No. DE-AC02-07CH11358.

References

1. Le Tacon, M., Sacuto, A., Georges, A., Kotliar, G., Gallais, Y., Colson, D., Forget, A.: Nat. Phys. **2**, 537 (2006)
2. Tanaka, K., Lee, W.S., Lu, D.H., Fujimori, A., Fujii, T., Risdiana, Terasaki, I., Scalapino, D.J., Devereaux, T.P., Hussain, Z., Shen, Z.-X.: Science **314**, 1910 (2006)
3. Kondo, T., Takeuchi, T., Kaminski, A., Tsuda, S., Shin, S.: Phys. Rev. Lett. **98**, 267004 (2007)
4. Lee, W.S., Vishik, I.M., Tanaka, K., Lu, D.H., Sasagawa, T., Nagaosa, N., Devereaux, T.P., Hussain, Z., Shen, Z.-X.: Nature (London) **450**, 81 (2007)
5. Guyard, W., Le Tacon, M., Cazayous, M., Sacuto, A., Georges, A., Colson, D., Forget, A.: Phys. Rev. B **77**, 024524 (2008)
6. Hanaguri, T., Kohsaka, Y., Davis, J.C., Lupien, C., Yamada, I., Azuma, M., Takano, M., Ohishi, K., Ono, M., Takagi, H.: Nat. Phys. **3**, 865 (2007)
7. Khasanov, R., Kondo, T., Strässle, S., Heron, D.O.G., Kaminski, A., Keller, H., Lee, S.L., Takeuchi, T.: Phys. Rev. Lett. (2008, accepted). arXiv:0806.1907
8. Kondo, T., Takeuchi, T., Yokoya, T., Tsuda, S., Shin, S., Mizutani, U.: J. Electron Spectrosc. Relat. Phenom. **137–140**, 663 (2004)
9. Kondo, T., Takeuchi, T., Mizutani, U., Yokoya, T., Tsuda, S., Shin, S.: Phys. Rev. B **72**, 024533 (2005)
10. Sonier, J.E., Brewer, J.H., Kiefl, R.F.: Rev. Mod. Phys. **72**, 769 (2000)
11. Khasanov, R., Landau, I.L., Baines, C., La Mattina, F., Maisuradze, A., Togano, K., Keller, H.: Phys. Rev. B **73**, 214528 (2006)
12. Khasanov, R., Shengelaya, A., Maisuradze, A., La Mattina, F., Bussmann-Holder, A., Keller, H., Müller, K.A.: Phys. Rev. Lett. **98**, 057007 (2007)
13. Brandt, E.H.: Phys. Rev. B **68**, 054506 (2003)
14. Wang, Y., Ono, S., Onose, Y., Gu, G., Ando, Y., Tokura, Y., Uchida, S., Ong, N.P.: Science **299**, 86 (2003)
15. Amin, M.H.S., Franz, M., Affleck, I.: Phys. Rev. Lett. **84**, 5864 (2000)
16. Vekhter, I., Carbotte, J.P., Nicol, E.J.: Phys. Rev. B **59**, 1417 (1999)
17. Won, H., Maki, K.: Europhys. Lett. **54**, 248 (2001)
18. Lee, S.L., Zimmermann, P., Keller, H., Warden, M., Savić, I.M., Schauwecker, R., Zech, D., Cubitt, R., Forgan, E.M., Kes, P.H., Li, T.W., Menovsky, A.A., Tarnawski, Z.: Phys. Rev. Lett. **71**, 3862 (1993)
19. Carrington, A., Manzano, F.: Physica C **385**, 205 (2003)
20. Ichimura, K., Nomura, K., Minami, F., Takekawa, S.: J. Phys.: Condens. Matter **2**, 9961 (1990)

3 The energy gap of the superconducting phase

In this chapter we describe investigations of the energy gap of the superconducting state using AC susceptibility and muon-spin rotation measurements.

In 1950, almost forty years after the discovery of superconductivity, it could eventually be shown that the presence of even a weak pair-binding electron-electron interaction in metals leads to a superconducting state at finite temperatures. Studies of isotope-effects, *e.g.* for the transition temperature, provided evidence that the electron-phonon interaction mediates the pairing in conventional superconductors (*e.g.* [68]). An electron traveling through a medium polarizes the lattice by attracting the positively charged ions. The distributed excess positive charge thus created in turn attracts a second electron, assuming the interaction is strong enough to overcome the screened Coulomb repulsion. The phase transition to this new state of matter involves the opening of a gap in the energy spectrum of the electrons. As a consequence, the electron pairs thus created, decouple from low-energy excitations, since they are not able to absorb energy in units smaller than that necessary to overcome the gap, *i.e.* the pair binding energy. Thus carriers in a superconductor can flow through the crystal lattice without energy loss due to ohmic resistance, which is related to *e.g.* excitation of lattice vibrations. After extensive search for a microscopic theory, the framework given in 1957 by Bardeen, Cooper, and Schrieffer (BCS) theory offered an adequate description of the phenomenon [3].

In 1986, G. Bednorz and K. A. Müller discovered the cuprate high-temperature superconductors [4] and finally shattered the long standing transition temperature record, today (2009), at 135 K [5, 85]. Different experimental tools were used not only to prove the existence of a gap in the cuprates, but also to determine the amplitude and the symmetry of the gap. The superconducting state of the cuprates, characterized by reduced dimensionality and low carrier concentration, do not strictly obey the BCS predictions and are therefore labeled as unconventional. In cuprates we find, *e.g.* an exotic dominating momentum dependence of the binding energy of a $d_{x^2-y^2}$ functional form, in contrast to the s-wave gap of the standard BCS theory. Compared with conventional superconductors, the coherence length of cuprates is approximately three orders of magnitude smaller, whereas the magnetic penetration depth is about one order of magnitude larger.

The magnitude of the gap in the cuprate superconductors depends on the oxygen isotope mass, which we confirmed using AC susceptibility measurements. A nontrivial linear relation between the isotope effect for the superconducting energy gap and for the superconducting transition temperature was found.

As is impressively demonstrated with the fairly simple binary compound MgB_2, systems exhibiting multi-band superconductivity do exist. MgB_2 possesses two distinct energy gaps, a large gap associated with the quasi two-dimensional σ-bands and a smaller due to the three-dimensional π-band (see *e.g.* [86–88]). As shown in this chapter, we found evidence for multi-gap superconductivity in cuprates using μSR. Also the newly discovered pnictides are believed to be multi-gap superconductors (see *e.g.* [89, 90]).

Next we turn briefly to the concept of a gap in the energy spectrum. Suppose we have a simple metal with a well-defined Fermi surface that undergoes a phase transition to superconductivity. Below the transition temperature, pairs of electrons are formed as a consequence of a net electron-electron attraction. States close to the Fermi energy are

forbidden, since an energy gap Δ_{SC} at the Fermi surface opens below T_{c}. In contrast to the case of a normal band gap structure, normal electronic conduction always remains possible since the superconducting gap Δ_{SC} appears at the Fermi surface. The energy necessary to break a pair into two free electrons amounts to $2\Delta_{\mathrm{SC}}$.

The first theoretical prediction of an energy gap at the Fermi level of a superconductor was given in the BCS framework, where the gap equation was found to be

$$1 = \lambda_{\mathrm{ep}} \int_0^{\hbar\omega_{\mathrm{D}}} d\epsilon \, \frac{1}{E} \tanh(\frac{E}{2k_{\mathrm{B}}T}), \tag{27}$$

with $E = \sqrt{\epsilon^2 + |\Delta_{\mathrm{SC}}|^2}$ and λ_{ep} the dimensionless electron-phonon coupling constant. It should be noted that Eq. (27) implicitly predicts the transition temperature T_{c} and the zero temperature energy gap Δ^0_{SC}. In the limit $\Delta_{\mathrm{SC}} \to 0$ it can be shown that

$$k_{\mathrm{B}}T_{\mathrm{c}} = 1.13\,\hbar\,\omega_{\mathrm{D}} \exp(-1/\lambda_{\mathrm{ep}}), \tag{28}$$

where ω_{D} is the characteristic phonon frequency. Evaluating the integral in Eq. (27) for $T = 0$ and comparing the result with Eq. (28) yields the famous BCS result

$$2\Delta^0_{\mathrm{SC}} = 3.52\,k_{\mathrm{B}}\,T_{\mathrm{c}}. \tag{29}$$

One of the first experimental verifications of the existence of an energy gap in a superconductor was provided by Tinkham and Glover [91] by means of infrared spectroscopy. A gap in the energy spectrum strongly affects the absorption of electromagnetic waves. Unlike the case of conventional superconductors, the magnitude of the gap $\Delta_{\mathbf{k}}$ can also depend on the wave vector $\mathbf{k}$ as was found for the cuprates (*e.g.* [14]):

$$\begin{aligned} &\Delta_{\mathrm{SC}}(\mathbf{k}) = \Delta_{\mathrm{SC}} && \text{(conventional superconductors, } s\text{−wave)} \\ &\Delta_{\mathrm{SC}}(\mathbf{k}) = \Delta_{\mathrm{SC}}(\cos(k_x a) - \cos(k_y a))/2 && \text{(cuprates, } d_{x^2-y^2}\text{−wave)} \end{aligned} \tag{30}$$

We focus next on the role of the lattice, *i.e.* the role of phonons for superconductivity in cuprates. A direct approach is to investigate the influence of phonons on specific parameters by altering the phonon spectrum, which is accomplished with isotope exchange. An alternative approach is to study the response to variations in physical or chemical pressure. Isotope exchange studies require careful sample treatment, in particular back-exchange experiments that confirm observed effects as depending on the isotope masses only.

3.1 Isotope effects and the superconducting energy gap

3.1.1 Concept of DC magnetization and AC susceptibility measurements

A sample exposed to a static external magnetic field shows an internal magnetization. In the DC magnetization measurements, the macroscopic magnetic moment m of the sample can be determined by moving the magnetized sample through a set of pick-up coils and observing the change in the magnetic flux Φ_m. According to Faraday's law, a voltage $U_{\mathrm{ind}} = -\mathrm{d}\Phi_m/\mathrm{d}t$ is induced in the coils, from which the magnetic moment m can be deduced, and the magnetization M calculated as $M = m/V$, where V is the volume of the sample.

In an AC susceptibility measurement, in contrast, not the sample is moving to create a varying flux, but a small alternating magnetic field with frequency $f = \omega/2\pi$ is superimposed on the large static field. In this case the slope of the magnetization curve, not the absolute magnetic moment is measured. As a consequence the AC measurement is sensitive to dynamic effects. At sufficiently high frequencies the magnetization will lag behind the superimposed alternating field with a relative phase shift φ. The susceptibility χ is conveniently interpreted as consisting of a real (or in-phase) component $\chi^{'}$ and an imaginary (or out-of-phase) component $\chi^{''}$. The real part is a measure of the time average of the magnetic energy stored in the sample, while the imaginary part of χ is related to dissipative processes in the sample.

3.1.2 Motivation

In many conventional superconductors isotope exchange reveals a dependence of T_{c} on the isotope mass m that can be expressed as $T_{\mathrm{c}} \propto m^{-\alpha}$. In general, the isotope dependence of a quantity $F(m)$ is characterized by the isotope exponent α, defined as

$$\alpha = -\partial \log(F)/\partial \log(m). \tag{31}$$

Isotope experiments with mercury established a relation between the isotope mass and T_{c} with $\alpha \approx 0.5$ [92, 93]. These studies paved the way for a successful microscopic theory that delineates the importance of crystal lattice excitations for superconductivity. Phonons were theoretically implicated as responsible for superconductivity for the first time by Fröhlich [94] and Bardeen [95], ideas that eventually led to the development of the BCS theory [3]. As a matter of curiosity, it is interesting to note here that phonon interactions are also responsible for conventional ohmic resistance. In the BCS formula (Eq. (28)), it is the phonon frequency ω_{D} that governs the isotope effect. In the harmonic approximation of lattice vibrations $\omega_{\mathrm{D}} \propto m^{-0.5}$, and accordingly $\alpha = 0.5$. Subsequent measurements on various conventional superconductors showed that α can deviate substantially from 0.5. The BCS theory was developed in the framework of weak coupling, *i.e.* the electron-phonon coupling constant λ_{ep} is assumed to be small. This assumption is not strictly valid for a superconductor, *i.e.* in the strong-coupling regime, where deviations from $\alpha = 0.5$ may be found. Eliashberg worked out a formalism in order to extend the BCS theory for any value of λ_{ep} [96, 97]. Later, McMillan [98] included the screened Coulomb repulsion μ^* between electrons, which is put to use in

the McMillan-Allen-Dynes equation, where T_c may be expressed through [99].

$$k_B T_c = \frac{\hbar\omega_m}{1.2} \exp\left[-\frac{1.04(1+\lambda_{ep})}{\lambda_{ep} - \mu^*(1+0.62\lambda_{ep})}\right], \tag{32}$$

with ω_m the average phonon frequency. Using this formula, the less pronounced isotope effect found in conventional superconductors can be explained.

The unconventional cuprate superconductors show an isotope effect for T_c, as well as for the magnetic penetration depth λ, see *e.g.* [100–104]. Both isotope effects depend on the doping level, which is neither expected from the conventional BCS theory, nor from the more general Eliashberg equations. In the underdoped regime, a linear correlation between the two isotope effects was observed [100] and both decrease toward optimum doping to a value close to zero. Previously, the small isotope effect at optimum doping was erroneously taken as evidence that the lattice does not play a significant role for the pairing mechanism in cuprates. The BCS theory relates T_c directly to Δ_{SC} according to Eq. (29). The cuprates are known not to be BCS superconductors though, and it is not clear how Δ_{SC} is influenced by isotope exchange, and if so, whether the isotope effect depends on doping. Using low-field magnetization measurements in oxygen-isotope ($^{16}O/^{18}O$) substituted $Y_{1-x}Pr_xBa_2Cu_3O_{7-\delta}$ (x=0.0, 0.2, 0.3, 0.45) samples, we addressed this issue and found a novel isotope effect for the zero temperature superconducting energy gap Δ_{SC}^0 that scales with the effects for T_c and for λ.

3.1.3 Experimental details

Replacing Y in $YBa_2Cu_3O_{7-\delta}$ with Pr gradually lowers T_c. For $x = 0.0, 0.2, 0.3$, and 0.45 in $Y_{1-x}Pr_xBa_2Cu_3O_{7-\delta}$, we find $T_c = 93.2, 70.0, 55.5$, and 33.0 K, respectively. The polycrystalline samples were prepared using a solid-state reaction technique described in detail elsewhere [105]. After grinding, the powder was passed through a 10 μm sieve in order to obtain the fine mesh necessary for the determination of the magnetic penetration depth λ from low-field magnetization measurements. The oxygen-isotope ($^{16}O/^{18}O$) exchange process was performed by annealing the samples in a $^{18}O_2$ atmosphere. A consistent thermal history of the samples was affirmed through identical treatment. While annealing the substituted ^{18}O sample, the original ^{16}O sample was simultaneously heated in $^{16}O_2$ gas. According to the gravimetric analysis, the $^{18}O_2$ content of the substituted sample corresponds to a 90(2)% exchange. Samples for the back-exchange experiment were prepared, *i.e.* the ^{18}O (^{16}O) samples were again annealed in a ^{16}O (^{18}O) atmosphere. The back-exchange experiments are indispensable, since they ensure that any compositional deviation or preparation errors can be excluded from the data analysis. The samples containing Pr were then cast in epoxy and magnetically oriented, while curing in a 9 T field, as described in Sec. 2.1.3.

The magnetization measurements were performed with Quantum Design magnetometers (MPMS and PPMS). At 10 K the separation of the powder grains and the absence of weak links were confirmed by the linear relation between magnetization and the applied field [106]. The non-oriented samples containing no Pr were studied in a DC-field of 0.5 mT, whereas the oriented samples were measured in a 0.3 mT AC-field with frequency 333 Hz applied parallel to the c-axis. The samples containing Pr showed a

paramagnetic behavior that was measured in the normal-conducting regime and subsequently subtracted as a background signal from the diamagnetic magnetization in the superconducting phase.

Assuming spherical shape of the grains we applied the Shoenberg formula [107] in order to extract the temperature dependence of the magnetic penetration depth $\lambda(T)$ from the measured temperature dependence of the magnetic susceptibility $\chi(T)$,

$$\chi(T) = \frac{3}{2}\left[1 - \frac{3\lambda(T)}{R}\coth\left(\frac{R}{\lambda(T)}\right) + \frac{3\lambda^2(T)}{R^2}\right], \tag{33}$$

where R denotes the unknown average grain size. Since the screening currents flow in the ab-plane and decay over a distance λ_{ab} from the grain surface, we determined λ_{ab} with a small magnetic field parallel to the c-axis of the oriented sample. Only in non-oriented powders, an effective penetration depth λ_{eff} would be measured. For anisotropic cuprate superconductors, however, λ_{ab} is determined by the relation $\lambda_{\mathit{eff}} = 1.3\,\lambda_{ab}$ [108]. To account for the unknown grain size R, $\lambda_{ab}(2\,\mathrm{K})$ for the ^{16}O sample was normalized to the value obtained from μSR measurements [109]. Note that the absolute value of λ_{ab} depends on the absolute value of the magnetization and on R, whereas the temperature dependence of λ_{ab} is completely determined by the temperature dependence of χ [106], which justifies our approach.

3.1.4 Results and discussion

The data were analyzed using Eq. (25) with $w(\varphi) = 1$ and assuming a d-wave gap [$g(\varphi) = \cos(2\varphi)$]. To obtain the temperature dependence of the superconducting gap the approximate formula $s(T/T_\mathrm{c}) = \tanh(1.82[1.018(T_\mathrm{c}/T - 1)^{0.51}])$ [82] was used. The transition temperature T_c and the zero-temperature superconducting energy gap Δ^0_SC were determined from the analysis of $\lambda_{ab}^{-2}(T)$. The relative isotope effect for T_c and for Δ^0_SC was defined as $\delta X/X = (^{18}X - {}^{16}X)/{}^{16}X$ with X being either T_c or Δ^0_SC. The results were corrected for the incomplete isotope exchange of 90% in the ^{18}O samples, and are in agreement with literature data (see Ref. [110] and references therein).

Figure 17 displays the resulting Δ^0_SC versus the transition temperature T_c. Note that the analysis as outlined above is valid in the weak-coupling BCS theory, and not necessarily applicable to cuprates, for which the gap-to-T_c ratio is substantially larger. This can be seen in Fig. 17, where the dashed line represents the universal BCS value $2\Delta^0_\mathrm{SC}/k_\mathrm{B}T_c$=3.52, whereas the solid line corresponds to the strong-coupling value $2\Delta^0_\mathrm{SC}/k_\mathrm{B}T_\mathrm{c}$=5.34 predicted by a polaronic model [111]. Gap values for different high-temperature superconductors measured with various techniques are compared in Fig. 17. The overall agreement with our data is evident, and confirms the approach. Note that we do not address the issue of the complex nature of the superconducting energy gap, but only investigate the relative influence of isotope substitution on the gap. A calculation of the relative isotope effect for the superconducting gap of $Y_{1-x}Pr_xBa_2Cu_3O_{7-\delta}$ with different Pr-substitution fraction x, reveals an evident doping dependence. The doping behavior features a sign reversal of the isotope effect in the vicinity of optimum doping. Figure 18 shows the doping dependence of the relative oxygen-isotope effect in

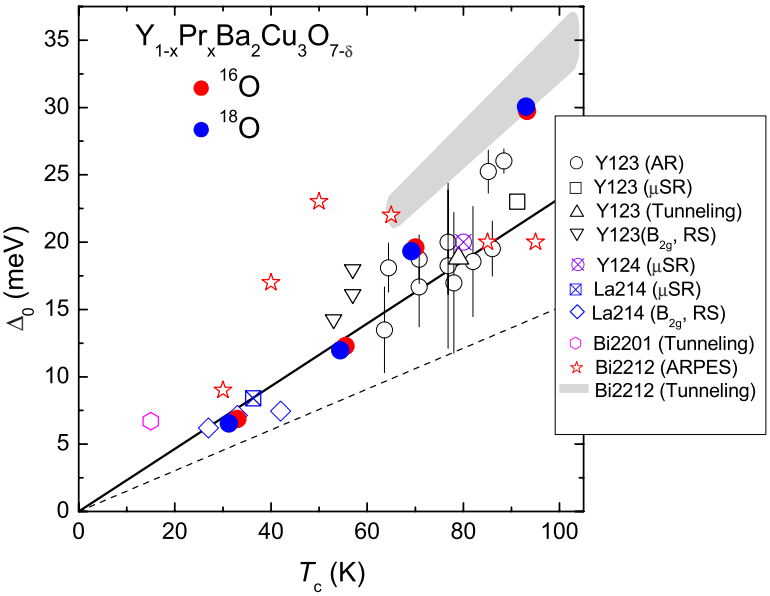

Figure 17: The zero-temperature superconducting gap versus the transition temperature T_c for $^{16}O/^{18}O$ substituted $Y_{1-x}Pr_xBa_2Cu_3O_{7-\delta}$ investigated with magnetization measurements, and for various hole-doped high-temperature superconductors studied by means of Andreev reflection (AR) [112], muon-spin rotation (μSR) [81, 113, 114], tunneling [115–117], Raman scattering (RS) [118], and angle-resolved photoemission (ARPES) [30] techniques. The solid red and blue circles are the $Y_{1-x}Pr_xBa_2Cu_3O_{7-\delta}$ data obtained in the present work. The open circles, the square, and the triangles are data for $YBa_2Cu_3O_{7-\delta}$ [112, 113] and $Y_{1-y}Ca_yBa_2Cu_3O_{7-\delta}$ [115] (Y123). The circled cross is the sole data point for $YBa_2Cu_4O_8$ (Y124) from [113]. The open diamonds and the squared cross are the data for $La_{2-x}Sr_xCuO_4$ (La214) from [81, 118]. The open hexagon corresponds to Pb doped $Bi_2Sr_2CuO_{6+x}$ (Bi2201) [116] and the asterisks represent the data for $Bi_2Sr_2Ca_{1x}Y_xCu_2O_8$ (Bi2212) [30]. The shaded grey area is reproduced from Ref. [117] where $2\Delta^0_{SC}/k_BT_c$=7.9(5) for Bi2212. The solid line corresponds to $2\Delta^0_{SC}/k_BT_c$=5.34, which was predicted theoretically using a two-component model with polaronic coupling [111]. The dashed line represents the universal BCS value $2\Delta^0_{SC}/k_BT_c$=3.52. After Paper **V** (Sec. 3.1.6).

Pr-substituted $Y_{1-x}Pr_xBa_2Cu_3O_{7-\delta}$ for $x = 0.0, 0.2, 0.3$, and 0.45 with sign reversed.

3.1.5 Conclusions

From low-field magnetization measurements on $Y_{1-x}Pr_xBa_2Cu_3O_{7-\delta}$ ($x = 0.0, 0.2, 0.3$, and 0.45) the oxygen-isotope effect of the zero-temperature superconducting energy gap was determined in this work for the first time. A non-trivial linear relation between the isotope effect for the energy gap and for T_c was found. The isotope effect is more pronounced in the underdoped regime, then decreases toward optimum doping and even-

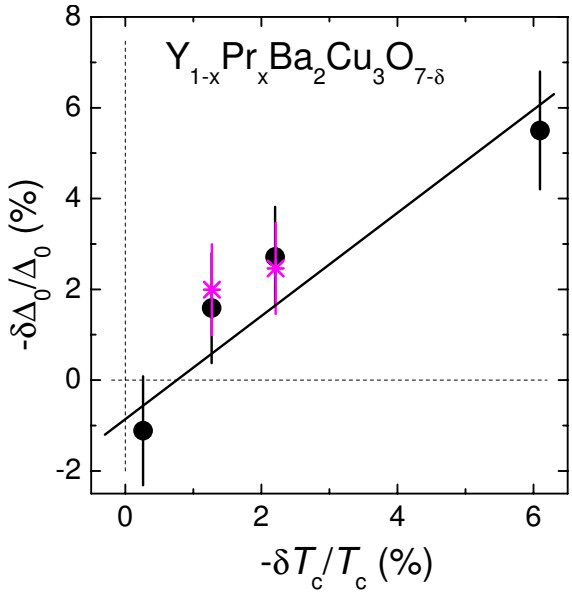

Figure 18: Oxygen-isotope shift of the zero-temperature superconducting gap $\Delta^0_{\rm SC}$ versus the oxygen-isotope effect on the transition temperature $T_{\rm c}$ for $Y_{1-x}Pr_xBa_2Cu_3O_{7-\delta}$ (x=0.0, 0.2, 0.3, 0.45). The solid line was obtained by model calculations as described in [111]. The results of the back-exchange experiments are included as asterisks. After Paper **V** (Sec. 3.1.6).

tually reverses sign close to optimum doping. This doping dependence, including the sign reversal, was predicted by model calculations based on polaron formation [111] and cannot be explained by present purely electronic mechanisms. The presence of a substantial isotope effect clearly indicates the importance of lattice effects for the physics of high-temperature superconductivity in the cuprates.

3.1.6 Paper V: Universal correlations of isotope effects in $\mathbf{Y_{1-x}Pr_xBa_2Cu_3O_{7-\delta}}$

This work is published in:

R. Khasanov, S. Strässle, K. Conder, E. Pomjakushina, A. Bussmann-Holder, and H. Keller, *Universal correlations of isotope effects in $Y_{1-x}Pr_xBa_2Cu_3O_{7-\delta}$*, Physical Review B **77**, 104530 (2008).

Abstract

The oxygen-isotope (^{16}O/^{18}O) effect on the zero-temperature superconducting energy gap Δ_0 is studied for a series of $Y_{1-x}Pr_xBa_2Cu_3O_{7-\delta}$ samples ($0.0 \leq x \leq 0.45$). In analogy to the isotope effect on the superconducting transition temperature, the isotope effect on Δ_0 increases with decreasing gap magnitude. A generic correlation between both isotope effects is established, which has been predicted from a polaronic model.

DOI:10.1103/PhysRevB.77.104530
PACS numbers : 74.72.Bk, 74.20.Mn, 82.20.Tr

Universal correlations of isotope effects in $Y_{1-x}Pr_xBa_2Cu_3O_{7-\delta}$

R. Khasanov,[1,2] S. Strässle,[2] K. Conder,[3] E. Pomjakushina,[3,4] A. Bussmann-Holder,[5] and H. Keller[2]
[1]*Laboratory for Muon Spin Spectroscopy, Paul Scherrer Institut, CH-5232 Villigen PSI, Switzerland*
[2]*Physik-Institut der Universität Zürich, Winterthurerstrasse 190, CH-8057 Zürich, Switzerland*
[3]*Laboratory for Developments and Methods, Paul Scherrer Institute, CH-5232 Villigen PSI, Switzerland*
[4]*Laboratory for Neutron Scattering, Paul Scherrer Institute and ETH Zurich, CH-5232 Villigen PSI, Switzerland*
[5]*Max-Planck-Institut für Festkörperforschung, Heisenbergstrasse 1, D-70569 Stuttgart, Germany*
(Received 22 January 2008; published 28 March 2008)

The oxygen-isotope ($^{16}O/^{18}O$) effect on the zero-temperature superconducting energy gap Δ_0 is studied for a series of $Y_{1-x}Pr_xBa_2Cu_3O_{7-\delta}$ samples ($0.0 \leqslant x \leqslant 0.45$). In analogy to the isotope effect on the superconducting transition temperature, the isotope effect on Δ_0 increases with decreasing gap magnitude. A generic correlation between both isotope effects is established, which has been predicted from a polaronic model.

DOI: 10.1103/PhysRevB.77.104530 PACS number(s): 74.72.Bk, 74.20.Mn, 82.20.Tr

I. INTRODUCTION

The microscopic pairing mechanism of high-temperature cuprate superconductors (HTSs) remains unknown even more than 20 years after their discovery. While for conventional superconductors the isotope effect on T_c has provided convincing evidence for a phonon-mediated pairing mechanism, the situation in HTSs is more complex, since the isotope effect is strongly doping dependent.[1–6] Especially, it is vanishingly small close to optimum doping.[1,2] This observation has frequently been taken as evidence that the lattice is inactive in the pairing mechanism. However, with decreasing doping and decreasing T_c, the isotope effect recovers and even exceeds the BCS value of 0.5 considerably.[1,4–6] While in conventional superconductors the isotope effect on T_c and the zero-temperature superconducting energy gap Δ_0 are intrinsically correlated, similar conclusions cannot be drawn for HTSs, especially in view of the complexity of the phase diagram and the order parameter. Thus, a systematic investigation of an isotope effect on Δ_0 can contribute to the understanding of these intricate materials.

In this paper, we report a study of the oxygen-isotope ($^{16}O/^{18}O$) effect (OIE) on Δ_0 in the cuprate superconductor $Y_{1-x}Pr_xBa_2Cu_3O_{7-\delta}$. A linear relation between Δ_0 and T_c is found as predicted theoretically. The isotope effect on Δ_0 scales linearly with the one on T_c and reverses sign around optimum doping, as anticipated from model calculations. Different doping levels of the isotope exchanged samples can be ruled out by performing careful back-exchange experiments.

II. EXPERIMENTAL DETAILS

Polycrystalline samples of $Y_{1-x}Pr_xBa_2Cu_3O_{7-\delta}$ ($x=0.0,0.2,0.3,0.45$) were prepared by standard solid state reaction.[7] In order to obtain fine grains needed for the determination of the magnetic field penetration depth λ by low field magnetization measurements, the ceramic samples were first grounded for approximately 20 min in air and then passed through 10 μm sieves. The oxygen-isotope exchange was performed by heating the samples in $^{18}O_2$ gas. In order to ensure the same thermal history of the substituted (^{18}O) and not substituted (^{16}O) samples, both annealings (in $^{16}O_2$ and $^{18}O_2$ gases) were always performed simultaneously. The ^{18}O content was determined from the weight change and corresponds to a 90(2)% exchange. The samples containing Pr were *c*-axis oriented in a field of 9 T, whereas samples with no Pr remained in nonoriented powder form.

ac and dc magnetization experiments were carried through in the temperature range 2–100 K by using Quantum Design magnetometers (MPMS and PPMS). The samples with no Pr were studied in dc experiments with a dc field amplitude of 0.5 mT. The oriented samples containing Pr were investigated with the ac field (field amplitude 0.3 mT and field frequency 333 Hz) applied parallel to the *c* axis. The separation of the grains and the absence of weak links were tested by confirming the linear relation between the magnetization and the field at $T=10$ K.[8] The dc field variation ranged from 0.5 to 1.5 mT, and the ac fields from 0.1 to 1 mT with frequencies between 49 and 599 Hz. The magnetization data were corrected by subtracting the paramagnetic background.

In Fig. 1, the magnetic susceptibility normalized to that of an ideal superconductor of spherical shape $\chi(T)/\chi_{id}$ is shown for the *c*-axis aligned ^{16}O and ^{18}O samples with $x=0.2$. Since the ratio $\chi(T)/\chi_{id}$ is substantially smaller than 1, it is ensured that the average size of the grains is comparable to λ. This strong reduction in $\chi(T)/\chi_{id}$ is a consequence of the surface-field penetration in each individual grain. In addition, in the whole temperature range, $\chi(T)$ is systematically larger in the ^{16}O samples than in the ^{18}O samples confirming that the penetration depth is reduced in the former samples as compared to the latter ones, in agreement with previous observations.[3–6,9,10]

In order to analyze the experimental data, we assume that the powder particles have a spherical shape and apply the Shoenberg formula[12]

$$\chi(T) = \frac{3}{2}\left[1 - \frac{3\lambda(T)}{R}\coth\frac{R}{\lambda(T)} + \frac{3\lambda^2(T)}{R^2}\right], \qquad (1)$$

which relates the measured susceptibility χ to the magnetic penetration depth λ. Here, R is the average grain-size radius.

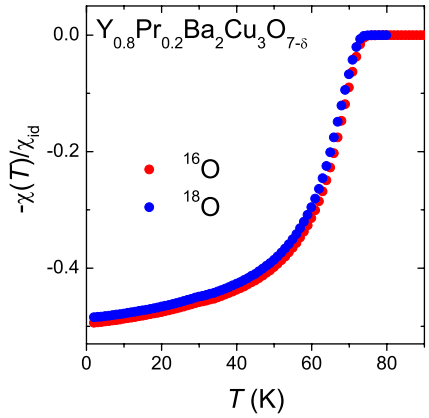

FIG. 1. (Color online) The temperature dependences of the magnetic susceptibility normalized to that for an ideal superconductor of spherical shape $\chi(T)/\chi_{id}$ for $^{16}O/^{18}O$ substituted $Y_{0.8}Pr_{0.2}Ba_2Cu_3O_{7-\delta}$.

The following issues are important for the interpretation of the experimental data: (i) When a small magnetic field is applied along the c axis, the screening currents flow in the ab plane, decaying on the distance λ_{ab} from the grain surface. Thus experiments on c-axis oriented samples provide direct information on λ_{ab}. (ii) From experiments on nonoriented powders, an effective averaged penetration depth λ_{eff} can be extracted. However, in highly anisotropic extreme type-II superconductors (as HTSs), this can—in turn—be related to the in-plane penetration depth through the relation $\lambda_{eff} \simeq 1.3\lambda_{ab}$.[13] (iii) The absolute value of λ_{ab} depends on the value of the susceptibility χ and the average grain-size radius R [see Eq. (1)], whereas the temperature dependence is independent of the grain size and entirely given by $\chi(T)$.[8]

III. EXPERIMENTAL RESULTS

The experimental results for the in-plane magnetic field penetration depth λ_{ab} for $^{16}O/^{18}O$ substituted $Y_{1-x}Pr_xBa_2Cu_3O_{7-\delta}$ with $x=0.0, 0.2, 0.3, 0.45$ are shown in Fig. 2(a). In order to account for the undetermined average grain radius R, the values of $\lambda_{ab}^{-2}(2\ \mathrm{K})$ for the ^{16}O samples were normalized to those obtained from muon-spin rotation (μSR) experiments.[14] To ensure that for the ^{16}O and ^{18}O substituted samples the doping level remained the same, back-exchange experiments were performed for two representative compositions [see Fig. 2(b)]. It is important to note here that these back-exchange experiments are absolutely essential since they guarantee that any compositional deviations or preparation errors are excluded. Only in this way can *real* isotope effects be observed in contrast to *marginal* ones caused by different doping levels.[15]

In the local (London) approximation ($\lambda \gg \xi$, ξ is the coherence length), the magnetic penetration depth in an anisotropic superconductor can be calculated via[16]

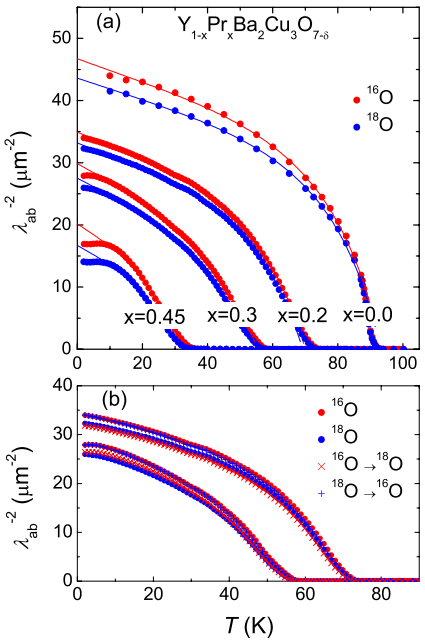

FIG. 2. (Color online) (a) Temperature dependences of the inverse-squared in-plane magnetic field penetration depth λ_{ab}^{-2} for $^{16}O/^{18}O$ substituted $Y_{1-x}Pr_xBa_2Cu_3O_{7-\delta}$ ($x=0.0, 0.2, 0.3, 0.45$) samples. The solid lines are results from a numerical analysis as described in the text. (b) $\lambda_{ab}^{-2}(T)$ for back-exchanged ($^{16}O \rightarrow ^{18}O$, $^{18}O \rightarrow ^{16}O$) $Y_{1-x}Pr_xBa_2Cu_3O_{7-\delta}$ ($x=0.2, 0.3$), showing that the doping level for the $^{16}O/^{18}O$ samples is unchanged.

$$\lambda_i^{-2}(T) = \frac{\mu_0 e^2}{4\pi^3\hbar} \oint \mathrm{d}S_F \frac{\vec{v}_i \cdot \vec{v}_i}{v_i} \left[1 + 2\int_{\Delta_k}^{\infty} \left(\frac{\partial f}{\partial E} \right) \frac{E\mathrm{d}E}{\sqrt{E^2 - \Delta_k^2}} \right]. \tag{2}$$

The index i refers to the principal crystallographic axes a, b, and c, v_i is the corresponding ith component of the Fermi velocity, $f=[1+\exp(E/k_BT)]^{-1}$ is the Fermi function, Δ_k is the value of the superconducting energy gap along k, and dS_F is the Fermi surface element. The second term in Eq. (2), which is negative, describes the decrease of $\lambda_i^{-2}(T)$ caused by the thermal population of Bogoliubov quasiparticle levels with energy E. It is this quantity where the anisotropy and the magnitude of the energy gap enter. By assuming that the Fermi velocity is constant, Eq. (2) can be reduced to[17]

$$\frac{\lambda_i^{-2}(T)}{\lambda_i^{-2}(0)} = 1 + \frac{1}{\pi}\int_0^{2\pi} \int_{\Delta(T,\varphi)}^{\infty} \left(\frac{\partial f}{\partial E} \right) \frac{E\mathrm{d}E\mathrm{d}\varphi}{\sqrt{E^2 - \Delta(T,\varphi)^2}}, \tag{3}$$

where $\lambda_i^{-2}(0)$ is the zero-temperature value of the magnetic penetration depth and $\Delta(T,\varphi)=\Delta_0 s(T/T_c)g(\varphi)$. The function $g(\varphi)$ describes the angular dependence of the gap, and Δ_0 is the maximum gap value at $T=0$. The temperature dependence of the gap $[s(T/T_c)]$ can either be obtained within the framework of the BCS theory extended to account for a d-wave superconductor, or by using the tabulated gap values,[18] or by applying the approximate equation[17]

TABLE I. Values of T_c and Δ_0 for the $^{16}O/^{18}O$ substituted $Y_{1-x}Pr_xBa_2Cu_3O_{7-\delta}$ samples investigated in this work. The relative isotope shifts of these quantities ($\delta T_c/T_c$ and $\delta\Delta_0/\Delta_0$) are given in the last two columns of the table. The values of $\delta T_c/T_c$ and $\delta\Delta_0/\Delta_0$ are corrected for the incomplete isotope exchange in the ^{18}O samples, where the ^{18}O exchange rate corresponds to 90%.

	^{16}O		^{18}O			
Sample	T_c (K)	Δ_0 (meV)	T_c (K)	Δ_0 (meV)	$\delta T_c/T_c$ (%)	$\delta\Delta_0/\Delta_0$ (%)
$YBa_2Cu_3O_{7-\delta}$	93.23(7)	29.75(22)	93.01(6)	30.06(24)	−0.26(11)	1.2(1.2)
$Y_{0.8}Pr_{0.2}Ba_2Cu_3O_{7-\delta}$	70.02(6)	19.61(14)	69.22(8)	19.33(13)	−1.27(16)	−1.6(1.1)
$Y_{0.7}Pr_{0.3}Ba_2Cu_3O_{7-\delta}$	55.50(8)	12.28(9)	54.40(8)	11.98(11)	−2.20(23)	−2.7(1.3)
$Y_{0.55}Pr_{0.45}Ba_2Cu_3O_{7-\delta}$	33.01(8)	6.87(5)	31.20(7)	6.53(5)	−6.09(37)	−5.5(1.2)
$Y_{0.8}Pr_{0.2}Ba_2Cu_3O_{7-\delta}$	69.80(6)[a]	19.54(12)[a]	69.02(7)[b]	19.19(13)[b]	−1.24(14)	−2.0(1.0)
$Y_{0.7}Pr_{0.3}Ba_2Cu_3O_{7-\delta}$	55.41(8)[a]	12.21(8)[a]	54.30(7)[b]	11.94(8)[b]	−2.23(22)	−2.5(1.0)

[a]Results for back-exchanged $^{18}O \rightarrow {}^{16}O$ samples.
[b]Results for back-exchanged $^{16}O \rightarrow {}^{18}O$ samples.

$$\Delta(T/T_c) = \Delta_0 \tanh\{1.82[1.018(T_c/T-1)^{0.51}]\}. \quad (4)$$

We emphasize here that the temperature dependence of the gap in HTSs was found to follow the weak-coupling BCS prediction.[19–21]

The result of the analysis of the experimental data by means of Eq. (3), with $\Delta(T/T_c)$ described by Eq. (4) and $g(\varphi)=|\cos(2\varphi)|$ for a d-wave gap,[22] are shown in Fig. 2 by solid lines. For $T>10$ K, all experimental data are consistently described by this approach with a nearly linear temperature dependence up to $T\approx 0.5T_c$. Below 10 K, the experimental data saturate in contrast to the calculated ones which continue to increase. This deviance between experiment and theory can be a consequence of impurity scattering,[23] chemical and/or structural defects,[24] or may be due to the above mentioned simplifying assumption that the gap is of d-wave symmetry only. From the data, neither of these sources can be identified unambiguously. The values of T_c and Δ_0 obtained from the analysis of the $\lambda_{ab}^{-2}(T)$ data are summarized in Table I. The relative isotope shifts of T_c and Δ_0 were determined from their relative percentage change with isotope substitution. The values of $\delta T_c/T_c$ and $\delta\Delta_0/\Delta_0$ ($\delta X/X=[^{18}X-{}^{16}X]/{}^{16}X$, $X=T_c$ or Δ_0), corrected for the incomplete isotope exchange in the ^{18}O samples, are also given in Table I. The results for the OIE on T_c are in accord with already published data.[1,2,4–6,10,11]

In Fig. 3, the values of the zero-temperature gap Δ_0, as determined in this study, are shown as a function of their corresponding values of T_c. In order to demonstrate their consistency with previously reported gap values, data for different HTSs, as obtained by a variety of different methods,[25–33] are included together with theoretical results discussed below.[34–36] The good agreement between the Δ_0 values of the present study with those reported in the literature implies that the above described procedure allows us to accurately determine the gap values from the measured $\lambda^{-2}(T)$. It is important to mention that even though our values of Δ_0 were derived indirectly and display some scattering (see Fig. 3), the OIE on the gap is *independent* of this methodology, since eventual errors in the absolute values of Δ_0 are systematic due to the same analysis of the data sets of ^{16}O and ^{18}O samples.

It should be outlined here that the use of Eqs. (3) and (4) in analyzing the experimental data is valid only for the case of weakly coupled BCS superconductors and does not necessarily hold for HTSs. However, the good agreement between the theoretically derived curves and the experimental ones for $T>10$ K (see Fig. 2), as well as a good correspondence of the previously reported Δ_0 values with those observed in the present study (see Fig. 3), justifies our approach.

IV. DISCUSSION

The data presented in Fig. 3 follow a general trend, namely, Δ_0 scales almost linearly with T_c. The linear relation between Δ_0 and T_c is absolutely nontrivial, since competing and coexisting energy scales dominate the phase diagram of HTSs. Especially, the pseudogap, which is in many experiments undistinguishable from the superconducting gap, has given rise to statements controverse to our findings, i.e., that Δ_0 increases with decreasing T_c (see, e.g., Ref. 37 and references therein). The linear relation between Δ_0 and T_c was predicted by BCS theory with a value of $2\Delta_0/k_BT_c=3.52$, smaller than observed here (see Fig. 3), which can be attributed to the d-wave gap. This linear relation obviously requires that an isotope effect on T_c results in the same isotope effect on the superconducting energy gap. However, as was outlined above, the complex symmetry of Δ_0 and the unidentified pairing mechanism do not admit any conclusions on the doping dependence of the isotope effect on the gap.

The OIE on Δ_0 is compared to the one on T_c in Fig. 4, together with theoretically derived results.[34] Interestingly, the same linear relation between both is observed in consistency with a model, where polaronic renormalizations of the single-particle energies were introduced.[34–36] Of fundamental importance is the observation of a sign reversal of the isotope effect around optimum doping, as predicted in Refs. 34–36, which provides evidence that polaronic effects may control the physics of HTSs.

The theoretical model considers two components where the doped holes lead to the formation of metallic regions in the otherwise insulating antiferromagnetic matrix (for details, see Refs. 34–36). These holes couple strongly to the ionic displacements to form polarons with variable spatial extent. Since these metallic polaronic clusters carry huge strain fields, a self-organization into patterns (stripes) takes place which lowers the strain energy and induces interactions between the matrix and the "polaron stripes."[34] The locally strong electron-lattice interaction within the metallic regions causes an *s*-wave order parameter, in contrast to the embedding matrix with a *d*-wave order parameter. Interband interactions between both subsystems guarantee a single transition temperature together with coupled gaps which were calculated self-consistently. The important effect of the polaron formation is an exponential renormalization of the bandwidth which carries an isotope effect, and an isotope independent level shift. Principally, all hopping integrals are renormalized by the polaron formation, but they contribute in a very different way to the isotope effect.[36] By varying the polaronic coupling, both coupled gaps, Δ_s and Δ_d, are calculated self-consistently for each coupling from which the average gap $\Delta_0=\sqrt{\Delta_s^2+\Delta_d^2}$ is obtained as a function of the corresponding T_c yielding $2\Delta_0/k_BT_c=5.34$. These results are included in Fig. 3 as a straight line together with experimental data obtained by different techniques.[25–33] The calculated oxygen-isotope shift of the average gap Δ_0 vs the one on T_c is compared to the present data of $Y_{1-x}Pr_xBa_2Cu_3O_{7-\delta}$ in Fig. 4. The observed good agreement between experiment and theory is in support of polaron formation. Here, it is worth mentioning that the isotope effect on the individual gaps, i.e., Δ_s and Δ_d, is of the same order of magnitude for both gaps, but always slightly enhanced for the *d*-wave gap as compared to the *s*-wave one.[34] It is important to emphasize that even though our approach resembles formally the two-band BCS theory, we do not consider conventional electron-phonon coupling as the pairing interaction, but local polaron formation. This has, besides the above mentioned important band renormalizations, the additional effect of reducing the Coulomb repulsion considerably which can even become attractive. A further relevant point to mention is that the calculated isotope effect is a consequence of the renormalization of only the second and interplanar hopping integrals whereas the direct hopping integral yields the wrong tendency of the isotope effect. From these results, conclusions about the relevant displacement which causes the isotope effect can be drawn.[34–36]

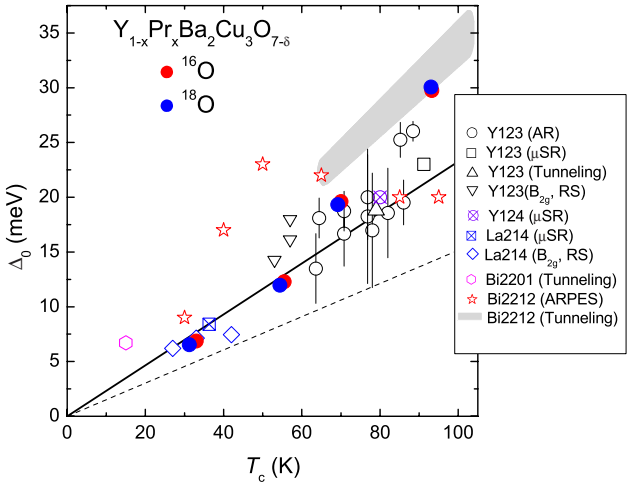

FIG. 3. (Color online) The zero-temperature superconducting gap Δ_0 vs the superconducting transition temperature T_c for $^{16}O/^{18}O$ substituted $Y_{1-x}Pr_xBa_2Cu_3O_{7-\delta}$ samples studied in the present work and various hole-doped HTSs studied by means of Andreev reflection (AR) (Ref. 25) muon-spin rotation (μSR) (Refs. 26–28), tunneling (Refs. 29–31), Raman scattering (RS) (Ref. 32) and angle-resolved photoemission spectroscopy (ARPES) (Ref. 33) techniques. Solid red and blue circles are the $Y_{1-x}Pr_xBa_2Cu_3O_{7-\delta}$ data obtained in the present study (see Table I). Open circles, square, and up and down triangles are the data for $YBa_2Cu_3O_{7-\delta}$ (Refs. 25 and 28) and $Y_{1-y}Ca_yBa_2Cu_3O_{7-\delta}$ (Ref. 29) (Y123). The crossed circle is the data point for $YBa_2Cu_4O_8$ (Y124) from Ref. 27. Open diamonds and the crossed square are the data for $La_{2-x}Sr_xCuO_4$ (La214) from Refs. 26 and 32. The open hexagon corresponds to Pb doped $Bi_2Sr_2CuO_{6+x}$ (Bi2201) (Ref. 30) and the stars represent the data for $Bi_2Sr_2Ca_{(1-x)}Y_xCu_2O_8$ (Bi2212) (Ref. 33). The shaded gray area has been extracted from Ref. 31 where $2\Delta_0/k_BT_c=7.9(5)$ was observed for Bi2212. The solid line corresponding to $2\Delta_0/k_BT_c=5.34$ has been predicted theoretically by using a two-component model with polaronic coupling (Ref. 34). The dashed line corresponds to the BCS value $2\Delta_0/k_BT_c=3.52$.

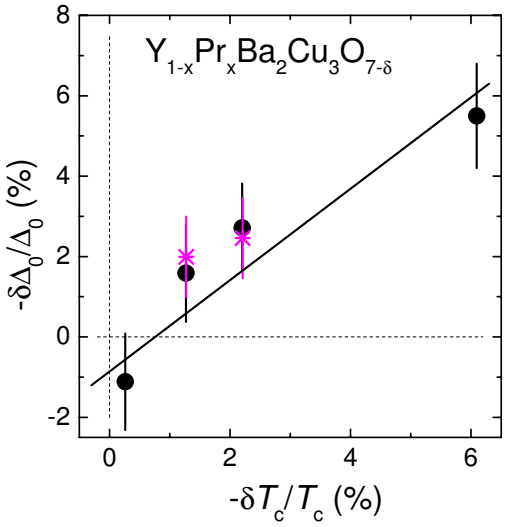

FIG. 4. (Color online) Comparison of the oxygen-isotope shift on the superconducting gap Δ_0 with the one on the transition temperature T_c for $Y_{1-x}Pr_xBa_2Cu_3O_{7-\delta}$ ($x=0.0,0.2,0.3,0.45$). The circles refer to the present experiments, and the solid line was obtained from model calculations as described in Refs. 34–36. The stars refer to the back-exchange data.

V. CONCLUSIONS

In summary, from measurements of the in-plane magnetic field penetration depth the zero-temperature superconducting energy gaps Δ_0 for $Y_{1-x}Pr_xBa_2Cu_3O_{7-\delta}$ ($0.0\leqslant x\leqslant 0.45$) were determined. A nontrivial linear relation between Δ_0 and T_c was found as predicted theoretically. The OIE on the super-

conducting gap Δ_0 scales linearly with the one on T_c and reverses sign around optimum doping. This sign reversal is in agreement with predictions from model calculations and unexpected from theories based on purely electronic mechanisms. Different doping levels of the isotope exchanged samples were ruled out by performing careful back-exchange experiments. The experimental results together with their theoretical analysis suggest that unconventional electron-lattice interactions play an important role in the physics of high-temperature superconductivity.

ACKNOWLEDGMENTS

The authors are grateful to K. Alex Müller for many stimulating discussions. This work was supported by the Swiss National Science Foundation, by the K. Alex Müller Foundation, and in part by the EU Project CoMePhS and the NCCR program *Materials with Novel Electronic Properties* (MaNEP) sponsored by the Swiss National Science Foundation.

[1] J. P. Franck, J. Jung, M. A.-K. Mohamed, S. Gygax, and G. I. Sproule, Phys. Rev. B **44**, 5318 (1991); J. P. Franck, in *Physical Properties of High Temperature Superconductors IV*, edited by D. M. Ginsberg (World Scientific, Singapore, 1994), p. 189.

[2] D. Zech, H. Keller, K. Conder, E. Kaldis, E. Liarokapis, N. Poulakis, and K. A. Müller, Nature (London) **371**, 681 (1994).

[3] G.-M. Zhao, M. B. Hunt, H. Keller, and K. A. Müller, Nature (London) **385**, 236 (1997).

[4] G.-M. Zhao, H. Keller, and K. Conder, J. Phys.: Condens. Matter **13**, R569 (2001).

[5] R. Khasanov, A. Shengelaya, E. Morenzoni, K. Conder, I. M. Savić, and H. Keller, J. Phys.: Condens. Matter **16**, S4439 (2004).

[6] H. Keller, in *Superconductivity in Complex Systems*, edited by K. A. Müller and A. Bussmann-Holder (Springer, Berlin, 2005), p. 143.

[7] K. Conder, Mater. Sci. Eng., R. **32**, 41 (2001).

[8] C. Panagopoulos, J. R. Cooper, G. B. Peacock, I. Gameson, P. P. Edwards, W. Schmidbauer, and J. W. Hodby, Phys. Rev. B **53**, R2999 (1996).

[9] J. Hofer, K. Conder, T. Sasagawa, G.-M. Zhao, M. Willemin, H. Keller, and K. Kishio, Phys. Rev. Lett. **84**, 4192 (2000).

[10] R. Khasanov, A. Shengelaya, E. Morenzoni, M. Angst, K. Conder, I. M. Savić, D. Lampakis, E. Liarokapis, A. Tatsi, and H. Keller, Phys. Rev. B **68**, 220506(R) (2003).

[11] R. Khasanov, D. G. Eshchenko, H. Luetkens, E. Morenzoni, T. Prokscha, A. Suter, N. Garifianov, M. Mali, J. Roos, K. Conder, and H. Keller, Phys. Rev. Lett. **92**, 057602 (2004).

[12] D. Shoenberg, Proc. R. Soc. London, Ser. A **175**, 49 (1940).

[13] V. I. Fesenko, V. N. Gorbunov, and V. P. Smilga, Physica C **176**, 551 (1991).

[14] C. L. Seaman, J. J. Neumeier, M. B. Maple, L. P. Le, G. M. Luke, B. J. Sternlieb, Y. J. Uemura, J. H. Brewer, R. Kadono, R. F. Kiefl, S. R. Krietzman, and T. M. Riseman, Phys. Rev. B **42**, 6801 (1990).

[15] A. R. Bishop, A. Bussmann-Holder, O. V. Dolgov, A. Furrer, H. Kamimura, H. Keller, R. Khasanov, R. K. Kremer, D. Manske, K. A. Müller, and A. Simon, J. Supercond. Novel Magn. **20**, 393 (2007).

[16] B. S. Chandrasekhar and D. Einzel, Ann. Phys. **505**, 535 (1993).

[17] A. Carrington and F. Manzano, Physica C **385**, 205 (2003).

[18] B. Mühlschlegel, Z. Phys. **155**, 313 (1959).

[19] K. Ichimura, K. Nomura, F. Minami, and S. Takekawa, J. Phys.: Condens. Matter **2**, 9961 (1990).

[20] M. Suzuki, T. Watanabe, and A. Matsuda, Phys. Rev. Lett. **82**, 5361 (1999).

[21] W. S. Lee, I. M. Vishik, K. Tanaka, D. H. Lu, T. Sasagawa, N. Nagaosa, T. P. Devereaux, Z. Hussain, and Z.-X. Shen, Nature (London) **50**, 81 (2007).

[22] G. Deutscher, Rev. Mod. Phys. **77**, 109 (2005).

[23] P. J. Hirschfeld and N. Goldenfeld, Phys. Rev. B **48**, 4219 (1993).

[24] C. Panagopoulos, W. Zhou, N. Athanassopoulou, and J. R. Cooper, Physica C **269**, 157 (1996).

[25] A. Kohen, G. Leibovitch, and G. Deutscher, Phys. Rev. Lett. **90**, 207005 (2003).

[26] R. Khasanov, A. Shengelaya, A. Maisuradze, F. La Mattina, A. Bussmann-Holder, H. Keller, and K. A. Müller, Phys. Rev. Lett. **98**, 057007 (2007).

[27] R. Khasanov, A. Shengelaya, A. Bussmann-Holder, J. Karpinski, H. Keller, and K. A. Müller, J. Supercond. Novel Magn. **21**, 81 (2008).

[28] R. Khasanov, S. Strässle, D. Di Castro, T. Masui, S. Miyasaka, S. Tajima, A. Bussmann-Holder, and H. Keller, Phys. Rev. Lett. **99**, 237601 (2007).

[29] N.-C. Yeh, C.-T. Chen, G. Hammerl, J. Mannhart, A. Schmehl, C. W. Schneider, R. R. Schulz, S. Tajima, K. Yoshida, D. Garrigus, and M. Strasik, Phys. Rev. Lett. **87**, 087003 (2001).

[30] M. C. Boyer, W. D. Wise, K. Chatterjee, M. Yi, T. Kondo, T. Takeuchi, H. Ikuta, and E. W. Hudson, Nat. Phys. **3**, 802 (2007).

[31] K. K. Gomes, A. N. Pasupathy, A. Pushp, S. Ono, Y. Ando, and A. Yazdani, Nature (London) **447**, 569 (2007).

[32] S. Sugai, H. Suzuki, Y. Takayanagi, T. Hosokawa, and N. Hayamizu, Phys. Rev. B **68**, 184504 (2003).

[33] K. Tanaka, W. S. Lee, D. H. Lu, A. Fujimori, T. Fujii, Risdiana, I. Terasaki, D. J. Scalapino, T. P. Devereaux, Z. Hussain, and Z.-X. Shen, Science **314**, 1910 (2006).

[34] A. Bussmann-Holder and H. Keller, in *Polarons in Advanced Materials*, Springer Series in Materials Science Vol. 103, edited by A. S. Alexandrov (Springer, New York, 2007), p. 599.

[35] A. Bussmann-Holder, H. Keller, A. R. Bishop, A. Simon, R. Micnas, and K. A. Müller, Europhys. Lett. **72**, 423 (2005).

[36] A. Bussmann-Holder and H. Keller, Eur. Phys. J. B **44**, 487 (2005).

[37] Ø. Fischer, M. Kugler, I. Maggio-Aprile, C. Berthod, and C. Renner, Rev. Mod. Phys. **79**, 353 (2007).

3.2 Multi-band superconductivity

3.2.1 Motivation

The superconducting gap opens in the conduction band at the Fermi energy as the temperature decreases below the transition temperature T_c. If there is a second band crossing the Fermi energy, it is possible that a multi-gap structure is present. As was realized only two years after the presentation of the BCS formalism in 1957 [3], a multiple order parameter can substantially enhance the transition temperature [119]. The two bands may interact through, *e.g.* band-scattering [120], such that superconductivity appears in both electronic subsystems at the same temperature. Inter-band interaction may even be a key element of high-temperature superconductivity. After the first experimental proof of two-gap superconductivity for Nb-doped $SrTiO_3$ in 1980 [121], one of the most prominent examples of two-band superconductivity was found in MgB_2. In this compound the sp^2-hybridization of the s-, p_x-, and the p_y-orbitals leads to the two-dimensional σ-band, whereas the p_z-orbitals form the so-called three-dimensional π-band. Both bands exhibit a superconducting gap with magnitudes of 7.1 meV and 2.8 meV respectively, and both open at the same transition temperature, ~ 38 K [122]. Compared with oxide superconductors, MgB_2 is a fairly simple binary compound that may be well described using first-principle calculations [123]. We performed the first nuclear magnetic resonance measurements on a small MgB_2 single crystal (mass $\sim 70\,\mu$g), focussing on the normal-conducting phase of the superconductor (see Sec. 3.2.6). Our findings are in good agreement with theoretical predictions.

The concept of multiple superconducting gaps is pursued here in order to explain the persistence of superconductivity in cuprates at high temperatures, see [124] (and references therein). Mainly based on tunneling data, it was argued early on that the superconducting condensate in cuprates may be non-uniform, and possibly described by both an s- and a d-wave order parameter [125]. Accumulating experimental evidence indicates that the cuprates indeed exhibit multi-component superconductivity. The same holds true for the newly discovered pnictides [89, 90, 126]. In cuprates, this idea is supported by several different experimental techniques, like nuclear magnetic resonance [127], angular-resolved photoemission [128], muon-spin rotation [81, 113], Raman scattering [129, 130], Andreev reflection [131], tunneling [132], and neutron crystal-field spectroscopy [133]. In particular, tunneling [134] and optical spectroscopy data [135, 136] suggest s-wave symmetry for the superconducting order parameter along the c-axis.

In order to address the complex structure of the gap in the bulk, single crystals are required. The μSR technique is bulk sensitive and works well for millimeter-sized single crystals. For a single crystal, the temperature dependence of the superfluid density can be determined separately for the three crystallographic axes, which allows conclusions about the gap symmetry. Our μSR experiments show an inflection point in the temperature dependence of the in-plane superfluid density at low temperatures for the two cuprate systems $La_{2-x}Sr_xCuO_4$ [81] and underdoped $YBa_2Cu_4O_8$ [113]. More general conclusions about the cuprates, *i.e.* intrinsic and universal properties, require investigation of structurally different cuprate systems, for which reason we also studied optimally doped single-crystalline $YBa_2Cu_3O_{7-\delta}$.

3.2.2 Experimental details

The μSR experiment on $YBa_2Cu_3O_{7-\delta}$ was made on a single crystal of dimensions roughly $4 \times 4 \times 1\,\mathrm{mm}^3$, prepared using the method described in [137]. The transition temperature $T_c = 91.2\,\mathrm{K}$ was determined by magnetization measurements, showing a transition width of 2 K, thus confirming the good sample quality. $YBa_2Cu_3O_{7-\delta}$ has an orthorhombic crystal structure with $b/a \approx 1.015$ [138]. The orthorombicity is determined by the CuO chain layer. In general, YBCO single crystals grow with built-in twinning boundaries at which the a- and b-axes commute. In order to allow for an accurate decomposition of the μSR data for each crystallographic axis, the amount of twinning was suppressed below 10% of the crystal volume by an annealing process under stress at 400 °C during 2 months.

Using transverse field μSR (for conceptual and technical details, see Sec. 2.3.1), the local magnetic field distribution in the mixed state was measured. The μSR experiments were performed at PSI on the general purpose spectrometer (GPS). The crystal was mounted in a holder, specially designed for thin platelet samples. Temperatures down to 1.7 K were reached and fields up to 0.64 T applied.

The data were analyzed using a four-component Gaussian to fit the μSR time signal, and applying the second moment method as described in Sec. 2.3.1. A sum of three Gaussians were taken to represent the local field distribution $P(B)$ due to the vortex lattice, whereas one Gaussian accounted for the background signal. The nuclear contribution to the depolarization rate σ_{nm} was determined at temperatures above T_c and taken into account according to Eq. (22). For highly anisotropic superconductors, such as the cuprates, the relation given in Eq. (23) ($\sigma \propto \lambda^{-2}$) must be modified accordingly when the external field is applied along the three crystallographic directions a, b, or c. If the external field is directed parallel to the crystallographic axis i, then the magnetic penetration depth can be derived from the second moment as [139]

$$\lambda_{jk}^{-2} = (\lambda_j \lambda_k)^{-1} \propto \sigma_{jk} = \sqrt{\sigma_j \sigma_k}, \tag{34}$$

where i, j, k stands for any of the crystallographic axes.

3.2.3 Results and discussion

The sample was field-cooled to 1.7 K in four different field strengths of 0.05, 0.1, 0.2, and 0.64 T applied parallel to the c-axis. The depolarization rate σ_{ab} was determined with 20-25 million events collected for each temperature. As in previous studies [81,113], $\sigma_{ab}(T)$ exhibits a prominent inflection point at low temperatures (see Fig. 19), which suggests the presence of two superconducting gaps of different size [124] in $YBa_2Cu_3O_{7-\delta}$. The data were analyzed assuming a small s- and a large d-wave gap. $\sigma(T)$ was accordingly represented in Eq. (25) with two components as $\sigma(T) = \sigma^d(T) + \sigma^s(T)$, with $\sigma(T)/\sigma(0) = \lambda_i^{-2}(T)/\lambda_i^{-2}(0)$, using tabulated values for $s(T/T_c)$ in Eq. (26) from Ref. [140] (solid red line in Fig. 19). This specific two-gap approach is justified by the current conventional assumption that cuprates are d-wave superconductors [141]. Hence the larger gap was chosen to have d-wave symmetry. Based on tunneling ([125] and Refs. therein) and Andreev reflection [131] experiments, however, the presence of a substantial isotropic

contribution to the superfluid density has been inferred. Therefore, the small gap was assumed to be isotropic. Note that this scheme of reasoning is also supported by magnetic field dependence measurements for the two gaps in LSCO [124], indicating the existence of a small s-wave contribution to a dominant d-wave in-plane order parameter[5]. The two zero-temperature in-plane gaps in $YBa_2Cu_3O_{7-\delta}$ were found to be $\Delta_0^d = 22.9(1)$ meV and $\Delta_0^s = 0.71(1)$ meV and were assumed to be field independent for the rather low fields applied. For $YBa_2Cu_3O_{7-\delta}$ a slight increase of the d-wave contribution to the superfluid density with increasing field was also found, which is consistent with earlier findings for LSCO, where the influence from the field was stronger for the small gap than for the larger [81].

The μSR experiments were performed with the external field applied parallel to the

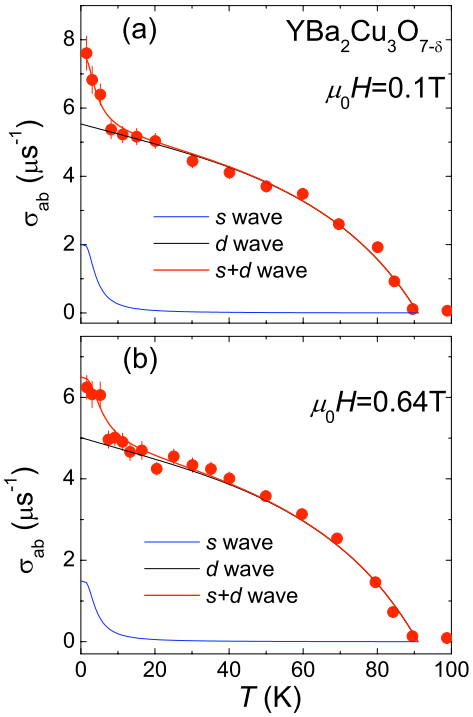

Figure 19: Temperature dependence of $\sigma_{ab} \propto \lambda_{ab}^{-2}$ measured in $YBa_2Cu_3O_{7-\delta}$ for two different fields: (a) 0.1 T and (b) 0.64 T. The solid lines represent calculations for a two-gap model, where the black line refers to the d-wave and the blue line to the s-wave contribution. After Paper **VI** (Sec. 3.2.5).

three principal crystallographic axes in order to determine λ_a^{-2}, λ_b^{-2}, and λ_c^{-2} separately. Along the a- and b-axes a field of 0.012 T and in the c-direction a field of 0.1 T was

[5]To determine the symmetry of each gap individually, the large gap can be measured separately if the smaller gap is quenched by an applied magnetic field. The symmetry of the larger gap can then be inferred from the slope of the superfluid density-vs-temperature curve at low temperatures. The actual field dependence of the small gap yields information about the **k** dependence of the smaller gap [124].

applied. From Eq. (34) one readily obtains the individual contributions as

$$\sigma_i = \frac{\sigma_{ij}\sigma_{ik}}{\sigma_{jk}} \propto \lambda_i^{-2}. \tag{35}$$

The individual components of the anisotropy parameter γ can be computed using

$$\gamma_{ij} = \lambda_i/\lambda_j = \sqrt{\sigma_j/\sigma_i}. \tag{36}$$

Fig. 20a shows the temperature dependences of the individual components $\sigma_i \propto \lambda_i^{-2}$ $(i = a, b, c)$ calculated according to Eq. (35). Both, σ_a and σ_b show a linear increase from 60 K down to 10 K, where an inflection point occurs, as was also found for the two-band approach outlined above.

The chains in YBCO are metallic systems with higher conductivity in the direction of the chains. It has been argued that one of the gaps is associated with the chains but the relative contributions from the two gaps are almost identical along the *a*- and *b*-directions. Moreover, a similar multi-gap mechanism was also found for chain-free LSCO [81]. Thus we conclude that the two-gap behavior is not a consequence of the chain structure in YBCO, but an intrinsic property of the cuprates. In contrast to σ_a and σ_b, the temperature dependence of σ_c is rather different, since it saturates below ~ 40 K, see Fig. 20a. This suggests a dominant *s*-wave mechanism in the direction of the *c*-axis, for which the analysis yields 17.5 meV, assuming an isotropic zero-temperature out-of-plane gap. The temperature dependence of the calculated anisotropy parameter is shown in Fig. 20b. The in-plane anisotropy, γ_{ab}, is almost temperature independent, whereas the out-of-plane anisotropies γ_{ca} and γ_{cb} increase for decreasing temperature, a behavior expected for multi-band superconductivity [90].

3.2.4 Conclusions

In μSR experiments with $YBa_2Cu_3O_{7-\delta}$, a distinct increase of the in-plane superfluid density was found in a series of measurements with decreasing temperature. Around 10 K an inflection point appears. Such an inflection point is expected for the case of a two-gap mechanism with $2\Delta/(k_B T_c)$ considerably smaller for one of the gaps. In contrast, the superfluid density saturates at lower temperatures for the out-of-plane component. The μSR data are thus suggesting the presence of a major *d*-wave gap in the CuO_2 planes of the cuprates, which mixes with an isotropic gap that dominates the superfluid density in direction of the *c*-axis. Due to this mixing, a small *s*-wave component would be present also in the in-plane superfluid density. This emphasizes the three-dimensional character of the cuprates, which is not supported in approaches, like *e.g.* the $t - J$ model, for which focus is exclusively on the CuO_2 planes. The small *d*-wave contribution to the out-of-plane superfluid density, which would be expected as a consequence of the band interaction, could not be resolved in the measurements.

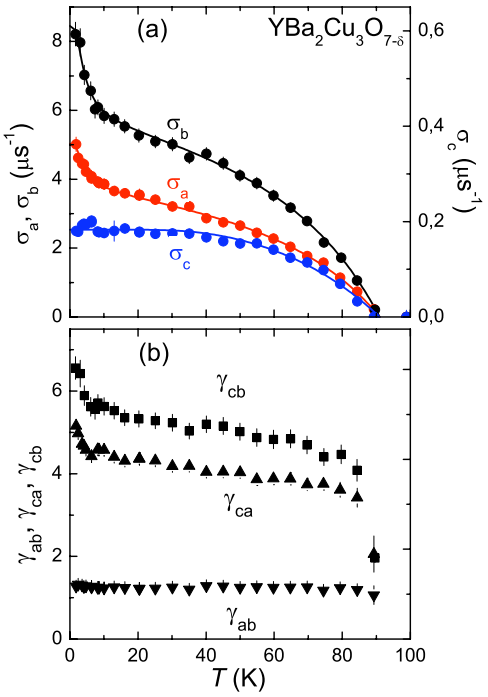

Figure 20: In panel (a) the temperature dependence of the individual components $\sigma_i \propto \lambda_i^{-2}$ $(i = a, b, c)$ for single crystalline $YBa_2Cu_3O_{7-\delta}$ are displayed. σ_a and σ_b are analyzed in a two-band model assuming a large d-wave and a small s-wave gap. σ_c was modeled using a simple s-wave approach. Panel (b) shows the calculated anisotropy parameters γ_{ab}, γ_{ca}, and γ_{cb}, as obtained from Eq. (36). After Paper **VI** (Sec. 3.2.5).

3.2.5 Paper VI: Multiple Gap Symmetries for the Order Parameter of Cuprate Superconductors from Penetration Depth Measurements

This work is published in:

R. Khasanov, S. Strässle, D. Di Castro, T. Masui, S. Miyasaka, S. Tajima, A. Bussmann-Holder, and H. Keller, *Multiple Gap Symmetries for the Order Parameter of Cuprate Superconductors from Penetration Depth Measurements*, Physical Review Letters **99**, 237601 (2007).

Abstract

The temperature dependence of the London penetration depth was measured for an untwinned single crystal of $YBa_2Cu_3O_7$ along the three principal crystallographic directions (a, b, and c). Both in-plane components (λ_a^{-2} and λ_b^{-2}) show an inflection point in their temperature dependence which is absent in the component along the c-direction (λ_c^{-2}). The data provide convincing evidence that the in-plane superconducting order parameter is a mixture of (s+d)-wave symmetry whereas it is mainly s wave along the c-direction. In conjunction with previous results it is concluded that coupled (s+d)-order parameters are universal and intrinsic to cuprate superconductors.

DOI: 10.1103/PhysRevLett.99.237601
PACS numbers: 74.20.Rp, 74.25.Ha, 74.72.Dn, 76.75.+i

Errata

- Page 1, 2^{nd} column, 11^{th} line: $La_{2-x}SrCu_xO_4$.
- Page 3, 1^{st} column, Table 1: the indices s and d of $\sigma^{s}(0)$ and $\sigma^{d}(0)$ have to be interchanged in the header of the table.

Multiple Gap Symmetries for the Order Parameter of Cuprate Superconductors from Penetration Depth Measurements

R. Khasanov,[1] S. Strässle,[1] D. Di Castro,[1,2] T. Masui,[3] S. Miyasaka,[3] S. Tajima,[3] A. Bussmann-Holder,[4] and H. Keller[1]

[1]*Physik-Institut der Universität Zürich, Winterthurerstrasse 190, CH-8057 Zürich, Switzerland*

[2]*CRS Coherentia, CNR-INFM and Dipartimento di Fisica, Universita' di Roma "La Sapienza", P.le A. Moro 2, I-00185 Roma, Italy*

[3]*Department of Physics, Osaka University, Machikaneyama 1-1, Toyonaka, Osaka 560-0043, Japan*

[4]*Max-Planck-Institut für Festkörperforschung, Heisenbergstrasse 1, D-70569 Stuttgart, Germany*

(Received 26 July 2007; published 6 December 2007)

The temperature dependence of the London penetration depth λ was measured for an untwinned single crystal of $YBa_2Cu_3O_{7-\delta}$ along the three principal crystallographic directions (a, b, and c). Both in-plane components (λ_a^{-2} and λ_b^{-2}) show an inflection point in their temperature dependence which is absent in the component along the c direction (λ_c^{-2}). The data provide convincing evidence that the in-plane superconducting order parameter is a mixture of $(s + d)$-wave symmetry whereas it is mainly s wave along the c direction. In conjunction with previous results it is concluded that coupled $s + d$-order parameters are universal and intrinsic to cuprate superconductors.

DOI: 10.1103/PhysRevLett.99.237601 PACS numbers: 74.20.Rp, 74.25.Ha, 74.72.Dn, 76.75.+i

It is believed that the CuO_2 planes are essential for the occurrence of superconductivity in cuprate high-temperature superconductors (HTS's). Even though either static or dynamic distortions of these planes destroy the cubic symmetry, many theoretical approaches ignore the observed orthorhombicity and idealize the planar structure, mostly in order to justify a d-wave order parameter. Early on, it was, however, emphasized that cuprates must have a more complex order parameter than just d wave [1,2], supported by many experiments using techniques like nuclear magnetic resonance (NMR) [3], Raman scattering [4,5], angle-resolved electron tunneling [6], Andreev reflection [7], angular-resolved photoemission (ARPES) [8], muon-spin rotation (μSR) [9–11], and neutron crystal-field spectroscopy [12]. In addition, experiments probing properties along the c axis, like, e.g., tunneling [13], bicrystal twist Josephson junctions [14], optical pulsed probe [15], and optical reflectivity [16], suggest that a pure s-wave order parameter is realized here.

Multiple order parameter scenarios were proposed shortly after the BCS theory in order to account for a complex band structure and interband scattering [17–19]. This approach has the advantage that high-temperature superconductivity can easily be realized even within weak coupling theories since interband pair scattering strongly enhances the transition temperature (T_c) as compared to a single band model. The first realization of two-band superconductivity has been made in Nb doped $SrTiO_3$ [20]. With the discovery of high-temperature superconductivity in MgB_2, two-gap superconductivity became more prominent, and meanwhile more systems exhibiting multi-band superconductivity have been discovered (see, e.g., Refs. [20–24]). Interestingly, in all these systems the coupled superconducting order parameters are of the same symmetry, i.e., $s + s$, $d + d$. In this respect HTS's are novel since here mixed order parameter symmetries are realized, namely, $s + d$. Theoretically, it has been shown that mixed order parameters support even higher values of T_c as compared to coupled order parameters of the same symmetry [25].

In order to prove that complex order parameters are intrinsic and universal to HTS, previous μSR measurements [9–11] were continued for another HTS family, namely $YBa_2Cu_3O_{7-\delta}$. The μSR technique has the advantage that it is bulk sensitive and a direct probe of the London penetration depth. Recent results for $La_{1-x}Sr_xCuO_4$ and $YBa_2Cu_4O_8$ [9–11] clearly demonstrate the existence of two coupled $(s + d)$-wave gaps in the CuO_2 planes and an s-wave gap along the c axis in $YBa_2Cu_4O_8$. While these findings already suggest that a complex gap structure is intrinsic to HTS, the new results on $YBa_2Cu_3O_{7-\delta}$, presented below, support this conclusion consistently. We are thus reasoning that $(s + d)$-wave superconductivity in the planes and s-wave superconductivity along the c direction are intrinsic and universal to cuprates which imposes serious constraints for theoretical models.

The crystal was grown by a crystal pulling technique [26] and exhibited a rectangular shape of an approximate size of $4 \times 4 \times 1$ mm^3. The sample was untwinned by annealing it under stress for 2 months at 400 °C. The total fraction, where a and b axis are exchanged, occupies approximately 8% to 10% of the entire crystal, as confirmed by measurements with a polarized microscope. T_c and the transition width were determined by dc-magnetization measurements and found to be 91.2 K and 2 K, respectively.

The transverse-field μSR experiments were carried out at the $\pi M3$ beam line at the Paul Scherrer Institute (Villigen, Switzerland). The samples were field cooled from above T_c to 1.7 K in magnetic fields ranging from 0.012 T to 0.64 T. The typical counting statistics were

~20–25 million muon detections per data point. The analysis of the data was based on a four component Gaussian fit of the μSR time spectra where one component describes the background signal stemming from muons stopped outside the sample, and the three other components describe the asymmetric local magnetic field distribution $P(B)$ in the superconductor in the mixed state:

$$P(t) = \sum_{i=1}^{3} A_i \exp(-\sigma_i^2 t^2/2)\cos(\gamma_\mu B_i t + \phi) + A_{\rm bg}\exp(-\sigma_{\rm bg}^2 t^2/2)\cos(\gamma_\mu B_{\rm bg} t + \phi) \quad (1)$$

with the first term on the right-hand site corresponding to the field distribution [27]:

$$P(B) = \gamma_\mu \sum_{i=1}^{3} \frac{A_i}{\sigma_i}\exp\left(-\frac{\gamma_\mu^2 (B - B_i)^2}{2\sigma_i^2}\right). \quad (2)$$

Here $A_i(A_{\rm bg})$, $\sigma_i(\sigma_{\rm bg})$, and $B_i(B_{\rm bg})$ are the asymmetry, the relaxation rate, and the mean field of the ith component (background), $\gamma_\mu = 2\pi \times 135.5342$ MHz/T denotes the muon gyromagnetic ratio, and ϕ is the initial phase of the muon-spin ensemble.

The magnetic field penetration depth λ was derived from the total second moment of $P(B)$:

$$\sigma_{\rm tot}^2 = \sum_{i=1}^{3} \frac{A_i}{A_1 + A_2 + A_3}[\sigma_i^2 + \gamma_\mu^2 [B_i - \langle B\rangle]^2], \quad (3)$$

as $\lambda^{-4} \propto \sigma_{\rm tot}^2 - \sigma_{nm}^2 = \sigma^2$. Here σ_{nm} is the nuclear moment contribution, σ is the superconducting state contribution, and $\langle B\rangle$ is the first moment of $P(B)$ (see Ref. [9] for details).

Since cuprates are highly anisotropic, the relation $\sigma \propto \lambda^{-2}$ has to be extended to account for magnetic fields applied along the three crystallographic directions (i, j, $k = a$, b, c). For the field applied along the ith principal axis the penetration depth is determined from the second moment like $\lambda_{jk}^{-2} = (\lambda_j \lambda_k)^{-1} \propto \sigma_{jk} = \sqrt{\sigma_j \sigma_k}$ [28]. The magnetic field dependence of $\sigma_{ab} \propto \lambda_{ab}^{-2} = (\lambda_a \lambda_b)^{-1}$ has first been measured for different fields (0.05 T, 0.1 T, 0.2 T, and 0.64 T). The field was applied along the c axis and, subsequently, the sample was cooled down from above T_c to 1.7 K. In Fig. 1 σ_{ab} is shown as a function of temperature for two representative fields of 0.1 T and 0.64 T. In analogy to previous results [9–11], an inflection point in $\sigma_{ab}(T)$ is observed at $T \simeq 10$ K, which signals the coexistence of a small s-wave and a large d-wave gap. Accordingly, the data were analyzed by decomposing $\sigma(T)$ into two components having d-wave and s-wave symmetry: $\sigma(T) = \sigma^d(T) + \sigma^s(T)$ [9–11], where both components were expressed like [10,11]:

$$\frac{\sigma(T, \Delta_0)}{\sigma(0)} = 1 + \frac{1}{\pi}\int_0^{2\pi}\int_{\Delta(T,\varphi)}^{\infty}\left(\frac{\partial f}{\partial E}\right)\frac{E dE d\varphi}{\sqrt{E^2 - \Delta(T,\varphi)^2}}. \quad (4)$$

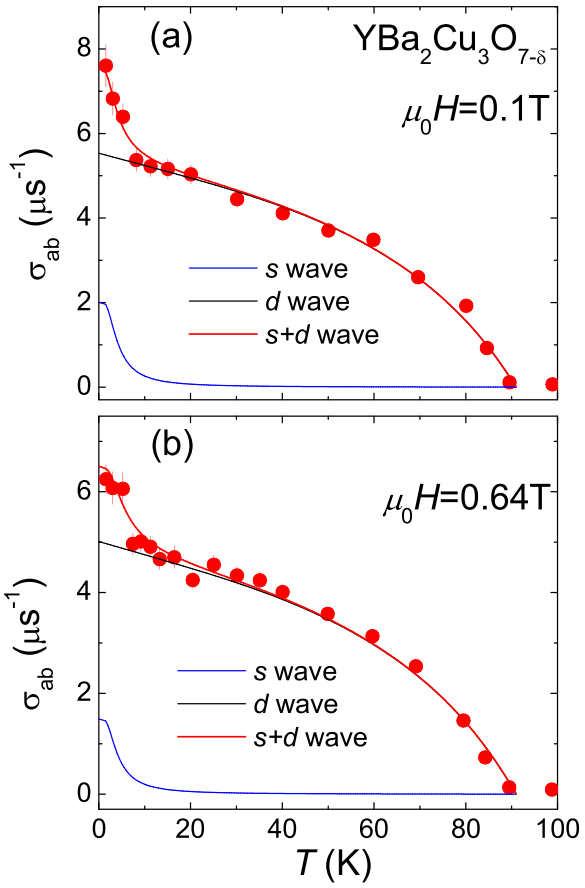

FIG. 1 (color online). Temperature dependences of $\sigma_{ab} \propto \lambda_{ab}^{-2}$ of $YBa_2Cu_3O_{7-\delta}$ measured after field cooling in $\mu_0 H = 0.1$ T (a) and 0.64 T (b). The red lines represent results of a numerical calculation using the two-gap model [9–11] with the parameters listed in Table I. The contributions of the small s-wave and the large d-wave gap to the in-plane superfluid density are shown by the blue and the black lines, respectively.

Here, $f = [1 + \exp(E/k_B T)]^{-1}$ is the Fermi function, Δ_0 is the zero-temperature gap value, and $\Delta(T, \varphi) = \Delta_0 \tilde{\Delta}(T/T_c) g(\varphi)$. For the normalized gap $\tilde{\Delta}(T/T_c)$ tabulated values of Ref. [29] were used. The function $g(\varphi)$ describes the angular dependence of the gap and is given by $g^d(\varphi) = |\cos(2\varphi)|$ for the d-wave gap [7] and $g^s(\varphi) = 1$ for the s-wave gap. Figure 1 shows the experimental data and the corresponding fits. The red lines refer to the sum of the two components, whereas the blue and the black lines display the individual s-wave and d-wave contributions, respectively. For all magnetic fields the analysis was based on common zero-temperature gap values [$\Delta_0^s = 0.71(1)$ meV and $\Delta_0^d = 22.9(1)$ meV] but field dependent second moments [$\sigma^s(0)$, $\sigma^d(0)$]. The parameters are summarized in Table I.

The d-wave contribution to the total superfluid density $\omega = \sigma^d(0)/[\sigma^s(0) + \sigma^d(0)]$ increases with increasing field (see Fig. 2), as observed already for $La_{1.83}Sr_{0.17}CuO_4$ [9].

TABLE I. Summary of the two-gap analysis for untwinned single-crystal $YBa_2Cu_3O_{7-\delta}$ for the magnetic field applied along the c direction. The meaning of the parameters is—$\mu_0 H$: applied magnetic field, $\sigma^d(0)$ and $\sigma^s(0)$: d-wave and s-wave contribution to the zero-temperature μSR relaxation rate $\sigma(0)$, $\omega = \sigma^d(0)/[\sigma^s(0) + \sigma^d(0)]$: the contribution of the large d-wave gap to the total in-plane superfluid density at $T = 0$ K, Δ_0^d: d-wave gap at $T = 0$ K, Δ_0^s: s-wave gap at $T = 0$ K.

$\mu_0 H$ (T)	$\sigma^d(0)$ (μs^{-1})	$\sigma^s(0)$ (μs^{-1})	ω	Δ_0^d (meV)	Δ_0^s (meV)
0.05	1.78(2)	4.80(7)	0.729(12)	22.9(1)[a]	0.71(1)[a]
0.1	2.01(2)	5.53(6)	0.734(11)		
0.2	1.87(2)	5.63(7)	0.751(13)		
0.64	1.49(2)	5.01(7)	0.771(16)		

[a]Common parameter for all magnetic fields.

This dependence is due to the fact that superconductivity is suppressed stronger in the s-wave band with increasing field than in the d-wave band [9].

The individual components λ_a^{-2}, λ_b^{-2}, and λ_c^{-2} as a function of temperature were obtained by applying the magnetic field along the three crystallographic axes (0.012 T along a and b, and 0.1 T along c) with the axis-related superfluid densities according to [11]:

$$\sigma_i = \sigma_{ij}\sigma_{ik}/\sigma_{jk} \propto \lambda_i^{-2}. \quad (5)$$

The results are shown in Fig. 3(a). Obviously σ_a and σ_b have a very similar temperature dependence with an inflection point at $T \simeq 10$ K and a linear increase for temperatures between 60 K and 10 K. The temperature dependence of σ_c is very different from the one of σ_a and σ_b. Here a saturation is observed at $T \lesssim 40$ K. $\sigma_a(T)$ and $\sigma_b(T)$ can be well described by the two-component approach (see above) using the same zero-temperature gap values. From this analysis the following individual contributions from the s-wave and the d-wave components along the a and b axis are obtained: $\sigma_a^s(0) = 1.19\ \mu s^{-1}$, $\sigma_a^d(0) = 3.83\ \mu s^{-1}$ and $\sigma_b^s(0) = 2.51\ \mu s^{-1}$, $\sigma_b^d(0) = 5.95\ \mu s^{-1}$. Since the relative contributions of the large d-wave component are almost the same along a and b directions, i.e., $\omega_a = 0.70$, $\omega_b = 0.76$, we conclude that not the CuO chains are the cause of the two-component behavior [30,31], but that this is an intrinsic property of cuprates. The same conclusions were reached from different experimental techniques as, e.g., NMR [3], Raman scattering [4,5], and ARPES [8]. In particular, Masui *et al.* [4] showed that the $s + d$ symmetry is required to describe the Raman data, even for *tetragonal* $Tl_2Ba_2CuO_{6+\delta}$ having no chains.

The temperature dependence of the c-axis-related superfluid density $\sigma_c \propto \lambda_c^{-2}$ resembles strongly the one ob-

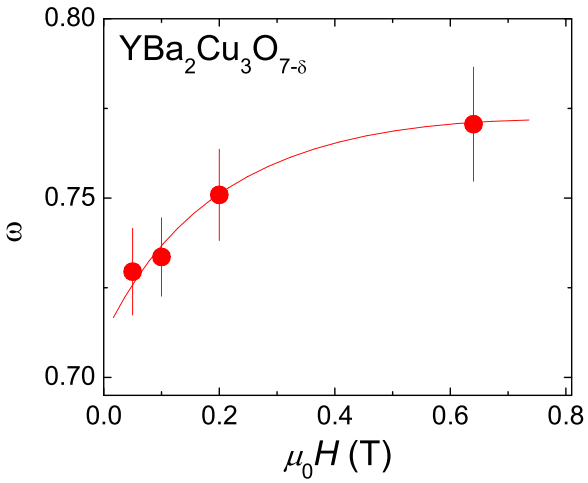

FIG. 2 (color online). The d-wave contribution to the in-plane superfluid density $\omega = \sigma^d(0)/[\sigma^s(0) + \sigma^d(0)]$ as a function of the magnetic field of $YBa_2Cu_3O_{7-\delta}$. The line is a guide to the eye.

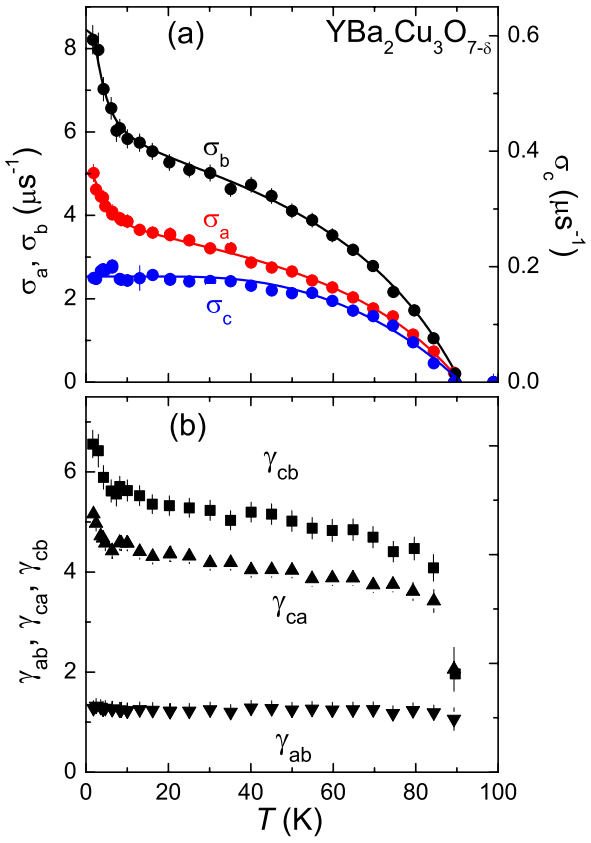

FIG. 3 (color online). (a) Temperature dependences of $\sigma_a \propto \lambda_a^{-2}$, $\sigma_b \propto \lambda_b^{-2}$, and $\sigma_c \propto \lambda_c^{-2}$ of $YBa_2Cu_3O_{7-\delta}$ obtained from $\sigma(T)$ measured along the crystallographic a, b, and c directions by using Eq. (5). Lines represent results of the analysis within the two-component (black and red lines) and one-component (blue line) models [11]. (b) Temperature dependences of the anisotropy parameters γ_{ab}, γ_{ca}, and γ_{cb} obtained as $\gamma_{ij} = \lambda_i/\lambda_j = \sqrt{\sigma_j/\sigma_i}$ (see text for details).

served for $YBa_2Cu_4O_8$ [11] and follows the one expected for an s-wave gap. The full blue curve in Fig. 3(a) stems from an analysis based on an isotropic s-wave gap [see Eq. (4)] with $\Delta_0^s = 17.52$ meV and $\sigma_c(0) = 0.183\ \mu s^{-1}$ in agreement with tunneling experiments [13]. The s-wave component along the c axis is not easily detectable by most experimental methods because either very well-oriented films or bulk methods have to be used. Since many experiments are surface sensitive only, and ab oriented samples and films are hardly available, these techniques are unable to see the s-wave component along the c axis. Its observation is, however, important since the coupling of a major d-wave component in the ab plane to the s-wave component along the c axis mixes both symmetries in the planes already. In addition, theory predicts that a pure d-wave order parameter is never observable and that also along the c direction an admixture of the d-wave order parameter has to be present [25]. This latter statement could provide an explanation for the optical conductivity spectra along the c direction where strongly anisotropic gaplike features have been observed [32,33].

Finally, the anisotropy $\gamma_{ij} = \lambda_i/\lambda_j = \sqrt{\sigma_j/\sigma_i}$ along all three crystallographic directions is calculated using Eq. (5). The results are shown in Fig. 3(b). While the in-plane anisotropy (γ_{ab}) is almost constant for all temperatures and close to 1.2, both out-of-plane components (γ_{ca} and γ_{cb}) are substantially larger (5 and 6.5 in the low-T limit) and exhibit a sharp increase, at $T \simeq 10$ K, as expected from Fig. 3(a). This high anisotropy reflects the fact that the CuO_2 planes have nearly Fermi liquidlike metallic properties whereas along the c direction almost insulating behavior is observed.

Our conclusions from the above presented data are manifold. Since $(s + d)$-wave symmetries of the superconducting order parameter were observed previously in various cuprate families [3–12], the new μSR data together with earlier results on different compounds [9–11] suggest that this behavior is *intrinsic* and *universal*. Similarly, the observation of an s-wave order parameter along the crystallographic c axis is proposed to be intrinsic as well. Specifically, this latter point emphasizes the importance of the *third* dimension for HTS's. Here it is worth mentioning that *ab initio* band structure calculations have correlated T_c with CuO_2 apical oxygen distances [34]. Also computations of ARPES intensities have concluded that contributions from the c axis are of crucial importance in understanding the physics of HTS's [35]. On the other hand, the observation of mixed order parameters and more specifically, the additional s-wave component, requires that the lattice must be considered in the physics of HTS's.

It is a pleasure to acknowledge many stimulating and supporting discussions with K. A. Müller. This work was partly performed at the Swiss Muon Source ($S\mu S$), Paul Scherrer Institute (PSI, Switzerland). The authors are grateful to A. Amato and D. Herlach for assistance during the μSR measurements. This work was supported by the Swiss National Science Foundation, by the K. Alex Müller Foundation, and the EU Project CoMePhS.

[1] K. A. Müller, Nature (London) **377**, 133 (1995).
[2] K. A. Müller and H. Keller, in *High-T_c Superconductivity 1996: Ten Years after the Discovery* (Kluwer, Dordrecht, 1997), p. 7.
[3] J. A. Martindale *et al.*, Phys. Rev. B **57**, 11 769 (1998).
[4] T. Masui *et al.*, Phys. Rev. B **68**, 060506(R) (2003).
[5] B. Friedl, C. Thomsen, and M. Cardona, Phys. Rev. Lett. **65**, 915 (1990).
[6] H. J. H. Smilde *et al.*, Phys. Rev. Lett. **95**, 257001 (2005).
[7] G. Deutscher, Rev. Mod. Phys. **77**, 109 (2005).
[8] D. H. Lu *et al.*, Phys. Rev. Lett. **86**, 4370 (2001).
[9] R. Khasanov *et al.*, Phys. Rev. Lett. **98**, 057007 (2007).
[10] R. Khasanov *et al.*, in *High-T_c Superconductors and Related Transition Metal Compounds*, edited by A. Bussmann-Holder and H. Keller (Springer, New York, 2007), p. 177.
[11] R. Khasanov *et al.*, arXiv:cond-mat/0705.0577.
[12] A. Furrer, in *High-T_c Superconductors and Related Transition Metal Compounds* edited by A. Bussmann-Holder and H. Keller (Springer, New York, 2007), p. 135.
[13] A. G. Sun *et al.*, Phys. Rev. Lett. **72**, 2267 (1994).
[14] Q. Li *et al.*, Phys. Rev. Lett. **83**, 4160 (1999).
[15] V. V. Kabanov *et al.*, Phys. Rev. B **59**, 1497 (1999).
[16] K. A. Müller, Inst. Phys. Conf. Ser. **181**, 3 (2004).
[17] H. Suhl, B. T. Matthias, and R. R. Walker, Phys. Rev. Lett. **3**, 552 (1959).
[18] V. Moskalenko, Fiz. Met. Metalloved. **8**, 503 (1959).
[19] V. Z. Kresin, J. Low Temp. Phys. **11**, 519 (1973).
[20] G. Binnig *et al.*, Phys. Rev. Lett. **45**, 1352 (1980).
[21] F. Giubileo *et al.*, Phys. Rev. Lett. **87**, 177008 (2001).
[22] E. Boaknin *et al.*, Phys. Rev. Lett. **90**, 117003 (2003).
[23] S. V. Shulga *et al.*, Phys. Rev. Lett. **80**, 1730 (1998).
[24] G. Seyfarth *et al.*, Phys. Rev. Lett. **95**, 107004 (2005).
[25] A. Bussmann-Holder, R. Micnas, and A. R. Bishop, Eur. Phys. J. B **37**, 345 (2003).
[26] Y. Yamada and Y. Shiohara, Physica (Amsterdam) **217C**, 182 (1993).
[27] R. Khasanov *et al.*, Phys. Rev. B **72**, 104504 (2005).
[28] S. L. Thiemann, Z. Radovic, and V. G. Kogan, Phys. Rev. B **39**, 11 406 (1989).
[29] B. Mühlschlegel, Z. Phys. **155**, 313 (1959).
[30] W. A. Atkinson and J. P. Carbotte, Phys. Rev. B **52**, 10 601 (1995).
[31] J. E. Sonier *et al.*, Phys. Rev. B **76**, 064522 (2007).
[32] J. Schützmann *et al.*, Phys. Rev. Lett. **73**, 174 (1994).
[33] S. Tajima *et al.*, Phys. Rev. B **55**, 6051 (1997).
[34] E. Pavarini *et al.*, Phys. Rev. Lett. **87**, 047003 (2001).
[35] S. Sahrakorpi *et al.*, Phys. Rev. Lett. **95**, 157601 (2005).

3.2.6 Two-band superconductivity in MgB_2

Although the chemical compound MgB_2 has been known for many decades, it was only in 2001 that phonon-mediated BCS superconductivity was discovered with the unexpected high transition temperature $T_c \approx 40\,K$ [142]. MgB_2 is the most prominent example of a two-band superconductor. The sp^2-hybridization of the boron $p_{x,y}$- and the magnesium s-electron orbitals leads to the so-called σ-band, the dimensionality of which is reduced. The remaining boron p_z-electron orbital forms the so-called π-band that is pronouncedly three-dimensional. MgB_2 possesses two superconducting gaps, a large σ-gap ($\sim 7\,meV$) associated with the σ-band and a smaller π-gap ($\sim 2\,meV$) manifested in the π-band (see *e.g.* [143]). Compared with the cuprates, MgB_2 is a fairly simple compound, for which a satisfying theoretical description within the BCS formalism [3] has been readily provided (see [143] and Refs. therein).

From the experimental point of view, however, there was still a considerable controversy concerning the ^{11}B magnetic shift tensor, and also a lack of experimental data for the nuclear-spin lattice relaxation rate anisotropy, for which theoretical predictions were already available. To measure the anisotropy of certain parameters, single crystals are required. We performed the first single-crystal ^{11}B [144] NMR investigation of MgB_2 (see Paper **VII**), including measurements of the nuclear spin lattice relaxation rate, and the magnetic shift as well as the anisotropies in the normal-conducting phase of the superconductor. Our results show good agreement with published theoretical calculations and in part with experimental NMR data from polycrystalline samples. Since the most accurate values for the electric field gradient are generally obtained from single-crystal NMR, we examined also the quadrupole interaction and deduced the sign of the electric field gradient.

3.2.7 Paper VII: ^{11}B NMR study of single-crystal MgB_2 in the normal conducting phase

This work is published in:

S. Strässle, J. Roos, M. Mali, H. Keller, and J. Karpinski, *^{11}B NMR study of single-crystal MgB_2 in the normal conducting phase*, Physica C **466**, 168 (2007).

Abstract

Single-crystal magnesium diboride (MgB_2) with a transition temperature to superconductivity of $T_c = 38.4\,K$ was investigated by quadrupole perturbed ^{11}B nuclear magnetic resonance in a field of 9 K in the normal conducting phase. Experimental values for the electric field gradient tensor, the magnetic shift tensor, and the nuclear spin-lattice relaxation time for boron were obtained. The anisotropy of the nuclear spin-lattice relaxation and the magnetic shift were determined. A positive sign of the electric field gradient was found. Our results show good agreement with published theoretical calculations and in part with experimental nuclear magnetic resonance data from polycrystalline samples.

Keywords: Nuclear magnetic resonance; Magnesium diboride

DOI:10.1016/j.physc.2007.07.002
PACS: 74.25.Nf; 74.70.Ad; 76.60.Cq; 76.60.Es

Available online at www.sciencedirect.com
ScienceDirect
Physica C 466 (2007) 168–173
PHYSICA C
www.elsevier.com/locate/physc

^{11}B NMR study of single-crystal MgB_2 in the normal conducting phase

S. Strässle [a,*], J. Roos [a], M. Mali [a], H. Keller [a], J. Karpinski [b]

[a] Physik-Institut der Universität Zürich, Universität Zürich, CH-8057 Zürich, Switzerland
[b] Solid State Physics Laboratory ETH, CH-8093 Zürich, Switzerland

Received 10 April 2007; received in revised form 2 July 2007; accepted 3 July 2007
Available online 13 July 2007

Abstract

Single-crystal magnesium diboride (MgB_2) with a transition temperature to superconductivity of $T_c = 38.4$ K was investigated by quadrupole perturbed ^{11}B nuclear magnetic resonance in a field of 9 T in the normal conducting phase. Experimental values for the electric field gradient tensor, the magnetic shift tensor, and the nuclear spin–lattice relaxation time for boron were obtained. The anisotropy of the nuclear spin–lattice relaxation and the magnetic shift were determined. A positive sign of the electric field gradient was found. Our results show good agreement with published theoretical calculations and in part with experimental nuclear magnetic resonance data from polycrystalline samples.

PACS: 74.25.Nf; 74.70.Ad; 76.60.Cq; 76.60.Es

Keywords: Nuclear magnetic resonance; Magnesium diboride

1. Introduction

Since the discovery of superconductivity (SC) in magnesium diboride (MgB_2) [1] considerable progress has been made in elucidating its physical properties. However, it proved to be a difficult task to grow single crystals of this intermetallic type-II superconductor. Therefore, the majority of investigations were performed on polycrystalline samples. In order to determine the anisotropy of certain parameters of this structurally highly anisotropic compound, single-crystal investigations are essential. Orienting the powder samples embedded in epoxy with a strong magnetic field to study anisotropic properties by means of nuclear magnetic resonance (NMR) has failed so far. Recently the technique for growing single crystals of MgB_2 was developed [2], and high-quality single crystals of reasonable size are now available suitable for various studies.

In particular, the observation of a substantial boron isotope effect [3,4] strongly suggests that MgB_2 is a phonon-mediated superconductor. However, the measured total isotope effect is reduced from the value calculated using the BCS standard model [5]. In first approaches to account for this reduction anharmonic phonon effects were invoked [6]. However, more recently it was shown by Mauri and collaborators [7] that the anharmonicity was overestimated and cannot explain the reduced isotope effect.

NMR is a suitable microscopic tool to probe the density of electronic states near the Fermi level through the static and fluctuating parts of the hyperfine fields created by carriers at the specific nuclear site. The measured quantities, the nuclear spin-lattice relaxation (NSLR) rate, $1/T_1$, and the Knight shift, $\mathbf{K}$, are proportional to the spin susceptibility of electrons close to the Fermi level, $\chi(\mathbf{q},\omega)$, specifically $1/(T_1T) \propto \lim_{\omega\to 0}\sum_{\mathbf{q}} \mathrm{Im}\chi(\mathbf{q},\omega)/\omega$ and $K \propto \mathrm{Re}\chi(0,0)$. The nuclear quadrupole frequency, ν_Q, reflects the overall charge distribution since it is directly connected to the electric field gradient (EFG) tensor, which is defined as the second derivative of the electrostatic potential at the nucleus site.

So far, experimental ^{11}B NMR studies on MgB_2 were performed on polycrystalline samples only [8–12]. While

* Corresponding author.
E-mail address: simon.straessle@physik.unizh.ch (S. Strässle).

0921-4534/$ - see front matter © 2007 Elsevier B.V. All rights reserved.
doi:10.1016/j.physc.2007.07.002

there is reasonable agreement on the nuclear quadrupole frequency and the NSLR rate in the normal conducting (NC) phase, there exists a considerable controversy for the magnetic shift. This discrepancy stems most probably from the difficulty to determine the small ^{11}B magnetic shift of a broad and quadrupolarly shifted ^{11}B central-line powder spectrum. Theoretical predictions for the anisotropy of the NSLR and the magnetic shift are available, but there is still a lack of experimental single-crystal data concerning the anisotropy of these quantities.

We report on the first single-crystal ^{11}B NMR investigation of MgB_2. Measurements of the NSLR rate and the magnetic shift including their anisotropies in the NC phase are presented. Since the most accurate values of the EFG tensor are generally obtained from single-crystal NMR, we examined the quadrupole interaction and also determined the sign of the EFG tensor. We compare our results to theoretical predictions and previous experimental findings.

The paper is organized as follows: In Section 2 we give a short overview of the experimental setup. Relevant NMR specific theoretical relations are summarized in Section 3. Our results are presented in Section 4, followed by a discussion in Section 5 and a short summary in Section 6.

2. Experimental details

Magnesium diboride (MgB_2) crystallizes in the fairly simple AlB_2-type structure, consisting of alternating hexagonal layers of Mg atoms and graphite-like honeycomb layers of B atoms. For our ^{11}B NMR investigation of MgB_2 a single crystal with a mass of $\approx$70 μg was used. It was prepared by a high pressure solid-state reaction technique, described in detail elsewhere [2], yielding flat crystals of excellent quality. The relevant NMR parameters of the ^{11}B isotope are [13]: natural abundance 80.1%, nuclear spin $I = 3/2$, nuclear quadrupole moment $^{11}Q = 0.04059(10) \times 10^{-28}\,\mathrm{m}^2$, and gyromagnetic ratio $\gamma_n = 8.5847 \times 10^7\,\mathrm{rad(Ts)}^{-1}$.

The NMR experiments were performed with a conventional phase-coherent pulse NMR spectrometer using a rather tiny NMR coil to optimize the filling factor. The NMR probe head was operated in an external field of $B_0 = 9$ T. By employing a (phase-alternating) accumulation technique the signal-to-noise ratio was improved. The spectra were obtained by complex Fourier transformation of the free induction decay, following a single radio-frequency excitation pulse. We measured the spin-lattice relaxation time, T_1, using the inversion-recovery pulse sequence with a typical $\pi/2$-pulse length of about 10 μs. Temperatures were stabilized with a precision of better than 0.5 K. The crystal was orientated with respect to $\mathbf{B}_0$ with an error smaller than 2°.

3. Theory

3.1. Nuclear quadrupole interaction

Consider an atom with a nuclear quadrupole moment (nuclear spin $I > 1/2$) in a crystal lattice. In case the lattice symmetry of this atom (nucleus probed by NMR) is less than cubic, quadrupolarly disturbed NMR delivers valuable information on the EFG, depending sensitively on the overall charge distribution in the crystal. This applies for B in MgB_2. Consistent with the local hexagonal symmetry the EFG at the boron site is axially symmetric along the c-axis direction, hence its major principal axis, V_{zz}, points into the c direction and the asymmetry parameter, $\eta = (V_{xx} - V_{yy})/V_{zz}$, $0 \leqslant \eta \leqslant 1$, vanishes. Here we use the convention $|V_{xx}| \leqslant |V_{yy}| \leqslant |V_{zz}|$. The Hamilton operator including Zeeman and quadrupole interaction of a nuclear spin, $\mathbf{I}$, can thus be written as [14]

$$H = H_Z + H_Q = -\hbar\gamma_n \mathbf{I}(1 + \mathbf{K}^{tot})\mathbf{B}_0 + \frac{eQV_{zz}}{4I(2I-1)}[3I_z^2 - \mathbf{I}^2], \quad (1)$$

where γ_n represents the gyromagnetic ratio and Q the electrical quadrupole moment of the nucleus. $\mathbf{K}^{tot}$ denotes the magnetic shift tensor. Since in our case the Zeeman term dominates, the quadrupole interaction can be treated as a perturbation. In a single crystal the quadrupole perturbed ^{11}B NMR spectrum is in first order split into three lines. The central line (CL) arises from the central transition, $(+\frac{1}{2}, -\frac{1}{2})$, the two satellite lines (SL's) correspond to the $(\pm\frac{1}{2}, \pm\frac{3}{2})$ transitions. The CL is affected in second-order only, resulting in an angular dependent second-order shift given by [14]

$$\nu^{(2)}_{-\frac{1}{2}\leftrightarrow\frac{1}{2}} = -\frac{\nu_Q^2}{16\nu_m}\left(I(I+1) - \frac{3}{4}\right)(1 - \cos^2\theta)(9\cos^2\theta - 1). \quad (2)$$

Here ν_m is the resonance frequency in case of no quadrupole interaction. θ denotes the angle between the crystallographic c axis and the $\mathbf{B}_0$ direction, and ν_Q indicates the quadrupole frequency defined as

$$\nu_Q = \frac{3eQ}{2I(2I-1)h} \times V_{zz} = \frac{eQ}{2h} \times V_{zz}. \quad (3)$$

The SL's are positioned symmetrically with respect to the CL and their frequency distance, $\Delta\nu$, can be described by the first-order quadrupole effect expression [14]

$$\Delta\nu = \left(m - \frac{1}{2}\right)\nu_Q(3\cos^2\theta - 1). \quad (4)$$

3.2. Magnetic shift

The magnetic coupling between the nuclear spin, $\mathbf{I}$, and its electronic environment can be viewed as a coupling of the nuclear magnetic moment $\hbar\gamma_n\mathbf{I}$ with a (time dependent) local magnetic hyperfine field, generated at the site of the nucleus by the conduction-electron spins and orbital motions. The static part of the hyperfine field produces a magnetic NMR line shift expressed by the magnetic shift tensor $\mathbf{K}^{tot}$. This tensor is defined as the relative displacement of the NMR frequency with respect to the NMR

frequency of the same nucleus in a non-metallic reference compound. In the reference frame of the EFG, using θ and ϕ as the polar angles of $\mathbf{B}_0$ and $\nu^{(2)}_{-\frac{1}{2}\leftrightarrow\frac{1}{2}}$ as defined in Eq. (2), the measured resonance frequency ν_0 is given by

$$\nu_0 = \nu_L[(1+K_{xx})^2\cos^2\phi\sin^2\theta + (1+K_{yy})^2 \times \sin^2\phi\sin^2\theta + (1+K_{zz})^2\cos^2\theta]^{\frac{1}{2}} + \nu^{(2)}_{-\frac{1}{2}\leftrightarrow\frac{1}{2}}. \quad (5)$$

The Larmor frequency, ν_L, is the resonance frequency measured in a non-metallic reference compound. $\mathbf{K}^{tot}$ can be split into an orbital, a spin, and a diamagnetic part: $\mathbf{K}^{tot}(T) = \mathbf{K}^{orb} + \mathbf{K}^{spin}(T) + \mathbf{K}^{dia}(T)$. $\mathbf{K}^{orb}$ denotes the orbital shift, stemming from the coupling of $\hbar\gamma_n\mathbf{I}$ to the electronic orbital moment. $\mathbf{K}^{spin}$ refers to the Knight (spin) shift, arising from the interaction between $\mathbf{I}$ and the spin paramagnetism of the conduction electrons. It can be decomposed in a dipole and a Fermi-contact (FC) interaction part. For a classical BCS-type superconductor the Knight shift is constant in the NC phase, decreases in the SC phase as a result of spin-singlet pairing, and approaches zero with zero slope at zero temperature [15]. $\mathbf{K}^{dia}$ finally is caused by diamagnetic properties of the sample. We can neglect it in the NC phase of MgB_2. However, below T_c the SC bulk diamagnetism sets in and gives rise to an additional shift, $\mathbf{K}^{dia}$, which has to be taken into account. The variation of the Knight shift with decreasing temperature cannot be followed easily across T_c, because it is hard to be distinguished from the dominating diamagnetic shielding. In addition the NMR line broadens in the SC phase due to the inhomogeneity of the internal magnetic field caused by the vortex structure in the mixed state of the crystal.

3.3. Spin–lattice relaxation

The nuclear spin-lattice relaxation (NSLR) of the boron nuclei in MgB_2 is dominantly caused by the fluctuating part of the local magnetic hyperfine field. T_1, the NSLR time, is defined as $1/T_1 = 2W$, where W represents the spectral density of fluctuation of internal magnetic fields at the Larmor frequency. For a noninteracting electron gas T_1 is related to the isotropic part of the Knight shift by the classical Korringa law [16]

$$T_1 T\mathbf{K}^2 = \frac{\hbar}{4\pi k_B}\left(\frac{\gamma_e}{\gamma_n}\right)^2. \quad (6)$$

Since in simple metals the FC interaction of s electrons at the Fermi level dominates the NSLR the Korringa law is generally satisfied. However, most of the Korringa T_1's, calculated with the measured $\mathbf{K}$ and Eq. (6), are shorter than the experimental ones. Appealing to other relaxation channels would make the theoretical times even shorter. A linear relation between $1/T_1$ and T is commonly called "Korringa behavior", whether Eq. (6) is satisfied or not.

In our experiment T_1 was measured by the method of selective inversion of the CL by a radio-frequency pulse and a subsequent monitoring of the nuclear magnetization recovery $M(t)$ at variable delay times t. The NSLR rate was extracted by fitting the data to the recovery law obtained for the solution of the master equation in case of selective excitation and magnetic relaxation of the CL [17]

$$\frac{M(\infty) - M(t)}{M(\infty)} = 2 \times \left[\frac{1}{10}e^{-\frac{t}{T_1}} + \frac{9}{10}e^{-\frac{6t}{T_1}}\right]. \quad (7)$$

4. Results

4.1. Spectra

The ^{11}B NMR spectra of MgB_2 are complex due to the simultaneous presence of first- and second-order quadrupole interactions, anisotropic magnetic shift, and nuclear dipolar coupling. Fig. 1 shows a single-crystal spectrum measured at a temperature of 81 K for $\mathbf{B}_0$ lying within the hexagonal planes ($\mathbf{B}_0 \perp c$). A CL and two asymmetric SL's ≈425 kHz separated in frequency with respect to the CL are observed. At the orientation $\mathbf{B}_0 \perp c$ the CL exhibits a clearly visible symmetric splitting (≈15.5 kHz) which is temperature independent in the temperature range investigated. The splitting is of homonuclear dipolar nature and angular dependent. In polycrystalline samples a similar splitting was observed [12,18]. For $\mathbf{B}_0 \perp c$ the present CL is well described by the sum of two Lorentzian lines with identical line width. The full line width at half maximum (FWHM) of the Lorentzian is ≈8 kHz and constant in the NC phase. However, it increases, as expected, in the SC phase due to the inhomogeneity of the internal magnetic field caused by the vortex structure in the mixed state. The sudden increase of the line width allows to determine $T_c(9\ T \perp c) = 24(1)$ K, which is slightly higher than previously reported values [11,19].

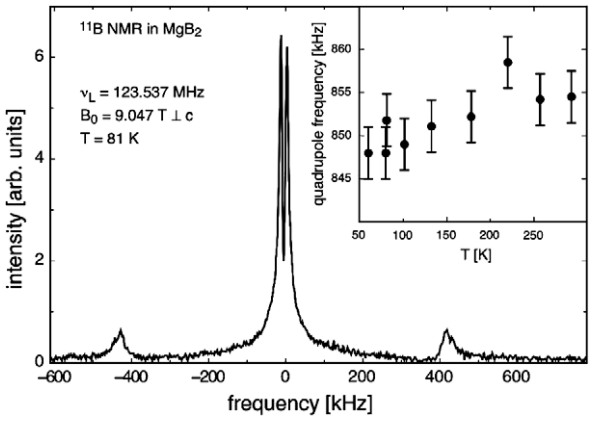

Fig. 1. ^{11}B NMR spectrum of the MgB_2 single crystal at 81 K ($B_0 \perp c$) showing a dipolarly split central line and two satellite lines asymmetric in shape. The frequency position of the central line is 123.5455 MHz, whereas the Larmor frequency is 123.5370 MHz (H_3BO_3). The inset shows the temperature dependence of the quadrupole frequency in single-crystal MgB_2.

4.2. Nuclear quadrupole interaction

In order to determine the nuclear quadrupole frequency, ν_Q, the frequency distance of the two SL's, $\Delta\nu$, at $\mathbf{B}_0 \perp c$ at various temperatures was measured (see inset Fig. 1). Applying Eq. (4) we obtained $\nu_Q = 849.5(3.0)$ kHz at 81 K, in agreement with experimental results reported on polycrystalline samples [8–11]. We observed a slight increase of ν_Q with increasing temperature in the range from 60 K up to 290 K of about 8(3) kHz. Previous powder measurements yielded a temperature independent ν_Q [8–11]. In order to check the orientation accuracy we measured the angular dependence of $\Delta\nu$ at 81 K. The result is plotted in Fig. 2, where the solid line represents the calculated angular dependence of $\Delta\nu$ using Eq. (4) and the measured $\nu_Q = 849.5$ kHz, in good agreement with experimental data.

4.3. Magnetic shift

The big advantage of having a single-crystal sample is the possibility to measure the anisotropy of several physical properties with the full spin-signal intensity. We investigated the frequency shift of the CL. The CL frequency vs. θ in the NC phase at 81 K is shown in Fig. 3. We denote by K_α a shift component measured with the external field parallel to the crystallographic α axis ($\alpha = a, b, c$). The fit of the experimental data to Eq. (5) using our measured values $\nu_Q = 849.5(3.0)$ kHz and $\nu_L = 123.5370$ MHz (aqueous solution of H_3BO_3) results in $K_c^{tot} = 119(3)$ ppm($\mathbf{B}_0 \| c$) and $K_{ab}^{tot} = 62(2)$ ppm($\mathbf{B}_0 \perp c$). One can determine the isotropic and the anisotropic part of $\mathbf{K}^{tot}$ according to $K_{iso}^{tot} = \frac{1}{3} \times (K_c^{tot} + 2K_{ab}^{tot}) = 81(5)$ ppm and $K_{aniso}^{tot} = \frac{1}{3} \times (K_c^{tot} - K_{ab}^{tot}) = 19(4)$ ppm, respectively. The isotropic shift is in agreement with previous experiments on non-oriented powder samples [8–10,12], correcting the data for the different reference materials used. Gerashenko et al. [9] give an upper limit for the anisotropic part of the Knight shift of 30 ppm measured in a 9.1 T field, whereas Baek et al. [12], using a maximum field of 7.2 T, could not detect any anisotropy.

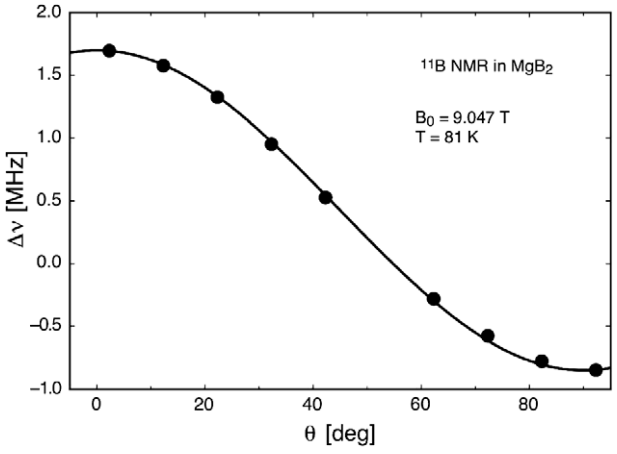

Fig. 2. Frequency difference between the two satellite lines, $\Delta\nu$, for single-crystal MgB_2 at 81K measured in an external magnetic field of $B_0 = 9$ T in dependence of the angle θ between crystallographic c-axis and $\mathbf{B}_0$ (errors are smaller than symbols). The solid line represents the calculated separation of the satellite lines (see text) using a quadrupole frequency of $\nu_Q = 849.5$ kHz.

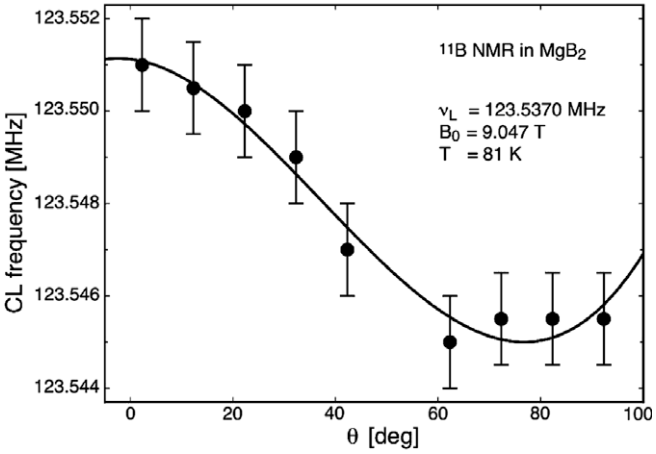

Fig. 3. Frequency position of the central line for single-crystal MgB_2 at 81 K measured in an external magnetic field of $B_0 = 9$ T in dependence of the angle θ between the crystallographic c axis and $\mathbf{B}_0$. The solid line represents a fit to the data (see text), yielding $K_{iso}^{tot} = 81(5)$ ppm and $K_{aniso}^{tot} = 19(4)$ ppm.

Our data reveal, within error bars, a temperature independent magnetic shift in the NC phase, in agreement with previous measurements on polycrystalline samples [9,10], whereas Jung et al. [8] report a decrease of the shift in their powder sample starting already at a temperature well above T_c. At the SC transition the observed change of the magnetic shift due to the onset of bulk diamagnetism yields $T_c(9\text{ T} \perp c) = 23(1)$ K, which is in good agreement with our determination of T_c from the change in the line width.

4.4. Spin–lattice relaxation time

We investigated $T_1(\theta)$ in the NC phase at 81 K and used Eq. (7) to analyze the data. In contrast to the powder measurements of Gerashenko et al. [9], our measurements reveal a clearly anisotropic T_1. At the orientation $\mathbf{B}_0 \| c$ and $\mathbf{B}_0 \perp c$ we find $T_1^{\|} = 1.93(3)$ s and $T_1^{\perp} = 1.78(3)$ s, respectively, resulting in a rate ratio $T_1^{\|}/T_1^{\perp} = 1.08(3)$.

The temperature dependence of $(T_1T)^{-1}$, shown in Fig. 4, was measured at $\mathbf{B}_0 \perp c$. A temperature independent value of $(T_1T)^{-1} = 6.8 \times 10^{-3}\ \text{K}^{-1}\ \text{s}^{-1}$ was found, in reasonable agreement with previous works on polycrystalline samples [8–10,12]. The worsening of the signal-to-noise ratio caused by the diamagnetic shielding due to the onset of superconductivity entails the need of a substantial increase of the measuring time in addition to the necessary increase due to the slow down of the NSLR, which made it impossible for us to get reliable data on the NSLR below T_c by measuring a single crystal.

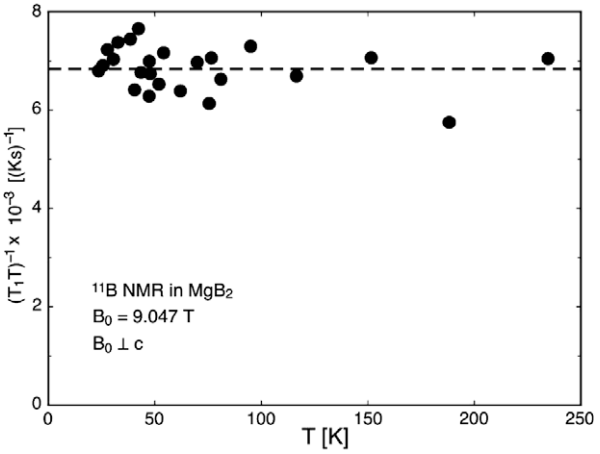

Fig. 4. Temperature dependence of $(T_1T)^{-1}$ at $\mathbf{B}_0 \perp c$ in single-crystal MgB_2 in an external field of 9 T. The dashed line illustrates the Korringa behavior with $(T_1T)^{-1} = 6.8 \times 10^{-3}\ \mathrm{K^{-1}\,s^{-1}}$. The arrow indicates the transition temperature to superconductivity as deduced from magnetic shift data.

5. Discussion

5.1. Nuclear quadrupole interaction

Using the ^{11}B quadrupole moment ^{11}Q and the experimentally determined ^{11}B ν_Q, we extract according to Eq. (3) the absolute value $|V_{zz}| = 17.3(1) \times 10^{20}\ \mathrm{V/m^2}$. We compare this value of $|V_{zz}|$ with that of *ab initio* calculations. The determination of V_{zz} at the boron site by Tsvyashchenko et al. [20] yields $V_{zz} = 18.5 \times 10^{20}\ \mathrm{V/m^2}$, in agreement with our experimental value. Experimental data by Mali et al. [21] confirm their calculation of $|V_{zz}|$ at the Mg site. Medvedeva et al. [22] report $|V_{zz}| = 18.8 \times 10^{20}\ \mathrm{V/m^2}$, which is also in agreement with our experiment.

The spectral shape of the ^{11}B CL and the SL's are governed by nearest-neighbor homonuclear dipolar interaction. The SL's are asymmetric in shape, as can be seen in Fig. 1. It was shown by Silver et al. [23] that the magnetic dipole coupling between like nuclei causes asymmetric SL's in quadrupolarly split single-crystal NMR spectra, which permits the determination of the sign of V_{zz}. With the positive gyromagnetic ratio of the boron nucleus we find $V_{zz} > 0$, as reported by Tsvyashchenko and co-workers [20]. However, Medvedeva et al. [22] find $V_{zz} < 0$, in contradiction to our finding.

For the discussion of the temperature dependence of the nuclear quadrupole frequency ν_Q we apply a semi-empirical approach. We separate the EFG tensor caused by the electronic and the ionic environment of the nucleus into a lattice and a valence part, $V_{\alpha\alpha} = V^{\mathrm{lat}}_{\alpha\alpha} + V^{\mathrm{val}}_{\alpha\alpha}$. The lattice contribution, $V^{\mathrm{lat}}_{\alpha\alpha}$, $(\alpha = x, y, z)$, stems from the distribution of the ions surrounding the nucleus. According to the point-charge model, these ions are approximated by point charges. The valence part, $V^{\mathrm{val}}_{\alpha\alpha}$, arises from electronic shells of the probed atom. $V^{\mathrm{val}}_{\alpha\alpha}$ is temperature independent, since the valence does not change. However, the absolute value of the lattice contribution, $|V^{\mathrm{lat}}_{\alpha\alpha}|$, generally diminishes with increasing temperature due to thermal expansion of the lattice. Therefore we can explain the temperature dependence of ν_Q by taking $V^{\mathrm{val}}_{\alpha\alpha}$ to be positive and $V^{\mathrm{lat}}_{\alpha\alpha}$ to be negative.

5.2. Magnetic shift

According to first-principal calculations of Pavarini and Mazin [24], the total effect of the FC polarization at the boron site in MgB_2 is small compared to the FC interaction at the Mg site. They interpret this as a consequence of the opposite sign of the comparable contributions of the 1s shell and the 2s shell. Moreover, there are only few boron s-type states present at the Fermi surface. In contrast to simple metals, in MgB_2 the FC contribution is not dominant. Therefore, the relative effect of the dipolar term is substantial and leads to a noticeable anisotropy of $\mathbf{K}^{\mathrm{spin}}$. The estimated anisotropy of the magnetic shift is about 30% [24], which is in good agreement with our result of $\approx$25%.

5.3. Spin–lattice relaxation time

Empirically, in most simple metals the FC interaction with s electrons appears to be the dominant relaxation channel, which causes an isotropic NSLR time. The experimental finding of $T_1^{\parallel}/T_1^{\perp} = 1.08(3)$ implies that relaxation mechanisms different from the FC polarization participate substantially in the relaxation process of ^{11}B in MgB_2. Band structure calculations considering hyperfine dipolar and orbital interactions with p electrons only, result in a rate ratio $T_1^{\parallel}/T_1^{\perp} \approx 1.2$ [9].

Using Eq. (6) we may calculate for 81 K an experimentally derived Korringa ratio $R^{\parallel} = \frac{4\pi k_B}{\hbar}\left(\frac{\gamma_n}{\gamma_e}\right)^2 (T_1^{\parallel}T) \times K_{\mathrm{ab}}^2) = 0.2$ and $R^{\perp} = \frac{4\pi k_B}{\hbar}\left(\frac{\gamma_n}{\gamma_e}\right)^2 (T_1^{\perp}T) \times \frac{1}{2}(K_{\mathrm{c}}^2 + K_{\mathrm{ab}}^2) = 0.5$. Earlier NMR studies on polycrystalline samples also revealed R values well below 1 [8,10,12,25]. The clear deviation from $R = 1$ indicates again that interactions different from the FC one must be involved in the relaxation process.

For MgB_2 the states at the Fermi level are mainly boron p-type, so that the FC term may become comparable or even smaller than the p-type dipole and orbital contribution to the NSLR. First-principal calculations (LDA) of Pavarini and Mazin [24] and Antropov et al. [26] suggest that in MgB_2 the orbital NSLR mechanism of the p electrons dominates over the dipolar and the FC ones due to the presence of all three p orbitals at the Fermi level. The orbital contribution of p-type electrons is expected to be proportional to temperature and not to follow the Korringa law [27], in agreement with experiments. Antropov et al. [26] estimate for the ratio $T_1^{\parallel}/T_1^{\perp} \approx 1.06$, consistent with our experimental value of 1.08(3).

6. Summary

We investigated single-crystal MgB_2 by means of NMR. In particular, measurements of the quadrupole frequency,

the anisotropic magnetic shift, and the anisotropic nuclear spin–lattice relaxation time in the normal conducting phase are reported. In addition, we determined the sign of the electric field gradient to be positive. The observed value of the quadrupole frequency, ν_Q, is in agreement with previous measurements on polycrystalline samples and theoretical predictions. In contrast to earlier works, ν_Q was found to be (slightly) temperature dependent. Our values and temperature dependences for the isotropic part of the magnetic shift and for the nuclear spin-lattice relaxation time, T_1, are in agreement with earlier NMR results of polycrystalline samples and theoretical predictions. The measured anisotropy of the magnetic shift of $\approx$25% is consistent with *ab initio* calculations. Moreover, the anisotropy of T_1 of 8(3)% extracted from the NMR data is in agreement with theoretical predictions. From the analysis of the data collected in the superconducting phase, we could not obtain reliable information on the Knight shift and on the nuclear spin-lattice relaxation rate.

Acknowledgements

We thank M. Angst for valuable discussions. This work was supported by the Swiss National Science Foundation and by the NCCR program Materials with Novel Electronic Properties (MaNEP) sponsored by the Swiss National Science Foundation.

References

[1] J. Nagamatsu, N. Nagakawa, T. Muranaka, Y. Zenitani, J. Akimitsu, Nature 410 (2001) 63.
[2] J. Karpinski, M. Angst, J. Jun, S.M. Kazakov, R. Puzniak, A. Wisniewski, J. Roos, H. Keller, L. Degiorgi, M.R. Eskildsen, L. Vinnikov, A. Mironov, Supercond. Sci. Technol. 16 (2003) 221.
[3] S.L. Bud'ko, G. Lapertot, C. Petrovic, C.E. Cunningham, N. Anderson, P.C. Canfield, Phys. Rev. Lett. 86 (2001) 1877.
[4] D.G. Hinks, H. Claus, J.D. Jorgensen, Nature 411 (2001) 457.
[5] J. Bardeen, L.N. Cooper, J.R. Schrieffer, Phys. Rev. 106 (1957) 162.
[6] A.Y. Liu, I.I. Mazin, J. Kortus, Phys. Rev. Lett. 87 (2001) 087005;
T. Yildirim, O. Gülseren, J.W. Lynn, C.M. Brown, T.J. Udovic, Q. Huang, N. Rogado, K.A. Regan, M.A. Hayward, J.S. Slusky, T. He, M.K. Haas, P. Khalifah, K. Inumaru, R.J. Cava, Phys. Rev. Lett. 87 (2001) 037001;
H.J. Choi, D. Roundy, H. Sun, M.L. Cohen, S.G. Louie, Phys. Rev. B 66 (2002) 020513.
[7] M. Lazzeri, M. Calandra, F. Mauri, Phys. Rev. B 68 (2003) 220509(R);
M. d'Astuto, M. Calandra, S. Reich, A. Shukla, M. Lazzeri, F. Mauri, J. Karpinski, N.D. Zhigadlo, A. Bossak, M. Krisch, Phys. Rev. B 75 (2007) 174508.
[8] J.K. Jung, S.H. Baek, F. Borsa, S.L. Bud'ko, G. Lapertot, P.C. Canfield, Phys. Rev. B 64 (2001) 12514.
[9] A. Gerashenko, K. Mikhalev, S. Verkhovskii, T. D'yachkova, A. Tyutyunnik, V. Zubkov, Appl. Magn. Reson. 21 (2001) 157.
[10] H. Kotegawa, K. Ishida, Y. Kitaoka, T. Muranaka, J. Akimitsu, Phys. Rev. Lett. 87 (2001) 127001.
[11] G. Papavassiliou, M. Pissas, M. Fardis, M. Karayanni, C. Christides, Phys. Rev. B 65 (2001) 012510.
[12] S.H. Baek, B.J. Suh, E. Pavarini, F. Borsa, R.G. Barnes, S.L. Bud'ko, P.C. Canfield, Phys. Rev. B 66 (2002) 104510.
[13] <http://www.webelements.com>.
[14] A. Abragam, The principles of nuclear magnetism, Clarendon, Oxford, 1961.
[15] K. Yoshida, Phys. Rev. 110 (1958) 769.
[16] J. Korringa, Physica 16 (1950) 601.
[17] E.R. Andrew, D.P. Tunstall, Proc. Phys. Soc. London 78 (1961) 1;
A. Narath, Phys. Rev. 167 (1967) 162;
A. Suter, M. Mali, J. Roos, D. Brinkmann, J. Phys.: Condens. Matter 10 (1998) 5977.
[18] D.R. Torgeson, R.G. Barnes, R.B. Creel, J. Chem. Phys. 56 (1972) 4178.
[19] M. Angst, R. Puzniak, A. Wisniewski, J. Jun, S.M. Kazakov, J. Karpinski, J. Roos, H. Keller, Phys. Rev. Lett. 88 (2002) 167004.
[20] A.V. Tsvyashchenko, L.N. Fomicheva, M.V. Magnitskaya, E.N. Shirani, V.B. Brudanin, D.V. Filossofov, O.I. Kochetov, N.A. Lebedev, A.F. Novgorodov, A.V. Salamatin, N.A. Korolev, A.I. Velichov, V.V. Timkin, A.P. Menushenkov, A.V. Kuznetsov, V.M. Shabanov, Z.Z. Akselrod, Solid State Commun. 119 (2001) 153, calculation performed within the density-functional theory using the full potential linearized augmented plane-wave method, with the generalized gradient approximation.
[21] M. Mali, J. Roos, A. Shengelaya, H. Keller, Phys. Rev. B 65 (2002) 100518.
[22] N.I. Medvedeva, A.L. Ivanovskii, J.E. Medvedeva, A.J. Freeman, D.L. Novikov, Phys. Rev. B 65 (2001) 052501, calculation performed within the first-principles full-potential linear muffin-tin orbital generalized gradient approximation method.
[23] A.H. Silver, T. Kushida, J. Lambe, Phys. Rev. 125 (1962) 1147.
[24] E. Pavarini, I.I. Mazin, Phys. Rev. B 64 (2001) 140504.
[25] S. Serventi, G. Allodi, C. Bucci, R. De Renzi, G. Guidi, E. Pavarini, P. Manfrinetti, A. Palenzona, Phys. Rev. B 67 (2003) 134518.
[26] V.P. Antropov, K.D. Belashchenko, M. van Schilfgaarde, S.N. Tashkeev, in: A. Narlikar (Ed.), Studies of High Temperature Superconductors, Vol. 38, Nova. Sci.Pub., 2001.
[27] G.C. Carter, L.H. Bennet, D.J. Kahan, Metallic Shifts in NMR, Progress in Material Science, Vol. 20, Pergamon Press, New York, 1977.

4 Outlook

The ^{89}Y NMR investigation of $Y_2Ba_4Cu_7O_{15-\delta}$ presented in this thesis provides new and significant constraints for orbital-current models. The work should stimulate detailed calculations of the expected orbital-current field strength at the Y site in YBCO compounds. Further experimental work should extend to NMR investigations of other cuprate superconductors, using different nuclei as probes.

Our ^{139}La NMR/NQR study shows that charge effects are present in cuprates, but further experimental effort is necessary to investigate if they are related to superconductivity. In particular, the La NQR spin-lattice relaxation behavior should be studied and compared with the La NMR spin-lattice relaxation, which might yield valuable information about the nature of the relaxation mechanism. Also the complex behavior of the NMR spin-lattice relaxation anisotropy should be investigated in more detail. Preliminary results show that the NMR and NQR line widths increase at low temperatures. The reason for the broadening is not yet understood. In addition, measurements of the in-plane copper nuclei in $LaBa_2Cu_3O_{7-\delta}$ and the comparison with the corresponding results for YBCO will allow more general conclusions. A study of compounds with higher oxygen deficiency δ and of the doping dependence would likewise be desirable.

Our μSR study of optimally doped $(BiPb)_2(SrLa)_2CuO_{6+\delta}$ (OP Bi2201) combined with ARPES results, suggests that the pseudogap and the superconducting phase in OP Bi2201 are selectively dominated by different parts of the Fermi surface. Other superconductors should be investigated in order to elucidate whether the selective property is generic. ARPES experiments focussing on the distribution of the quasiparticle weight at the Fermi surface might prove useful to further clarify the relation between the pseudogap and superconductivity. Knowledge about the connection between the pseudogap and the superconducting gap will help to determine their respective origin.

A confirmation of the non-trivial oxygen-isotope effect of the superconducting energy gap in $Y_{1-x}Pr_xBa_2Cu_3O_{7-\delta}$ by use of other techniques would be desirable. By means of tunneling, for instance, a direct measurement of the dependence of the gap magnitude on isotope mass should be attempted. Tunneling is a surface sensitive method for which sample quality is a critical issue. Whenever oxygen-isotope exchange is feasible, measurements on different cuprate superconductors should be considered. A possible candidate is Pr-free stoichiometric $YBa_2Cu_4O_8$, although the expected isotope effect would be small due to the high intrinsic doping level. For LSCO an extended investigation of the doping dependence with different relative amounts of La and Sr is possible, making this compound a promising candidate for investigations of the oxygen-isotope effect.

MgB_2 is the binary compound with the highest transition temperature known at the time of writing, and it has been proven unambiguously that a two-gap mechanism is at work. In contrast, multi-band superconductivity in the cuprates is still not generally accepted. For the newly discovered pnictide superconductors many experiments suggest a multi-band structure. Considering the state of the present knowledge, it is necessary to weigh the feasibility of multi-band mechanisms for high-temperature superconductors in general.

Even two decades after their discovery, cuprate superconductors remains a very interesting field of research in solid-state physics, and indeed several open questions have

to be answered. The recent discovery of superconductivity in the pnictides may generate new ideas that help to uncover the microscopic mechanisms of high-temperature superconductivity.

References

[1] H. Kamerlingh-Onnes, *The resistance of pure mercury at helium temperatures*, Comm. Phys. Lab. Uni Leiden **120b, 122b, 124c** (1911).

[2] W. Meissner and R. Ochsenfeld, *Ein neuer Effekt bei Eintritt der Supraleitfähigkeit*, Naturwissenschaften **21**, 787 (1933).

[3] J. Bardeen, L. N. Cooper, and J. R. Schrieffer, *Theory of Superconductivity*, Phys. Rev. **108**, 1175 (1957).

[4] J. G. Bednorz and K. A. Müller, *Possible high-T_c superconductivity in the Ba-La-Cu-O system*, Zeitschrift für Physik B **64**, 189 (1986).

[5] A. Schilling, M. Cantoni, J. D. Guo, and H. R. Ott, *Superconductivity above 130K in the Hg-Ba-Ca-Cu-O system*, Nature **363**, 56 (1993).

[6] P. Dai, B. C. Chakoumakos, G. F. Sun, K. W. Wong, Y. Xin, and D. F. Lu, *Synthesis and neutron powder diffraction study of the superconductor $HgBa_2Ca_2Cu_3O_{8+\delta}$ by Tl substitution*, Physica C **243**, 201 (1995).

[7] P. A. Lee and G. Sha, *Why are orbital currents central to high T_c materials*, Solid State Commun. **126**, 71 (2003).

[8] W. W. Warren, R. E. Walstedt, G. F. Brennert, R. J. Cava, R. Tycko, R. F. Bell, and G. Dabbagh, *Cu spin dynamics and superconducting precursor effects in planes above T_c in $YBa_2Cu_3O_{6.7}$*, Phys. Rev. Lett. **62**, 1193 (1989).

[9] M. Kugler, O. Fischer, C. Renner, S. Ono, and Y. Ando, *Scanning Tunneling Spectroscopy of $Bi_2Sr_2CuO_{6+\delta}$: New Evidence for the Common Origin of the Pseudogap and Superconductivity*, Phys. Rev. Lett. **86**, 4911 (2001).

[10] H. Ding, T. Yokoya, J. C. Campuzano, T. Takahashi, M. Randeria, M. R. Norman, T. Mochiku, K. Kadowaki, and J. Giapintzakis, *Spectroscopic evidence for a pseudogap in the normal state of underdoped high-T_c superconductors*, Nature **382**, 51 (1996).

[11] H. Takagi, B. Batlogg, H. L. Kao, J. Kwo, R. J. Cava, J. J. Krajewski, and W. F. Peck, *Systematic evolution of temperature-dependent resistivity in $La_{2-x}Sr_xCuO_4$*, Phys. Rev. Lett. **69**, 2975 (1992).

[12] N. M. M. Ido and M. Oda, *Correlation between Superconducting Gap and Pseudogap in High-T_c Cuprates*, J. Low Temp. Phys. **117**, 329 (1999).

[13] D. Rubio Temprano, J. Mesot, S. Janssen, K. Conder, A. Furrer, H. Mutka, and K. A. Müller, *Large Isotope Effect on the Pseudogap in the High-Temperature Superconductor $HoBa_2Cu_4O_8$*, Phys. Rev. Lett. **84**, 1990 (2000).

[14] T. Kondo, T. Takeuchi, A. Kaminski, S. Tsuda, and S. Shin, *Evidence for Two Energy Scales in the Superconducting State of Optimally Doped (Bi,Pb)$_2$(Sr,La)$_2$CuO$_{6+x}$*, Phys. Rev. Lett. **98**, 267004 (2007).

[15] B. Batlogg, H. Y. Hwang, H. Takagi, R. J. Cava, H. L. Kao, and J. Kwo, *Normal state phase diagram of (La,Sr)$_2$CuO$_4$ from charge and spin dynamics*, Physica C **235**, 130 (1994).

[16] M. R. Norman, *High Temperature Superconductivity - Magnetic Mechanisms*, Handbook of Magnetism and Advanced Magnetic Materials, Vol. 5, ed. H. Kronmüller and S. Parkin (Wiley, New York, 2007), p. 2671; see also: arXiv:cond-mat/0609559 .

[17] P. Lee, N. Nagaosa, and X.-G. Wen, *Doping a Mott insulator: Physics of high-temperature superconductivity*, Reviews of Modern Physics **78**, 17 (2006).

[18] N. J. Curro, T. Imai, C. P. Slichter, and B. Dabrowski, *High-temperature ^{63}Cu(2) nuclear quadrupole and magnetic resonance measurements of YBa$_2$Cu$_4$O$_8$*, Phys. Rev. B **56**, 877 (1997).

[19] H. Alloul, T. Ohno, and P. Mendels, *^{89}Y NMR evidence for a fermi-liquid behavior in YBa$_2$Cu$_3$O$_{6+x}$*, Phys. Rev. Lett. **63**, 1700 (1989).

[20] G. Q. Zheng, P. L. Kuhns, A. P. Reyes, B. Liang, and C. T. Lin, *Critical Point and the Nature of the Pseudogap of Single-Layered Copper-Oxide Bi$_2$Sr$_{2-x}$La$_x$CuOx + δ Superconductors*, Phys. Rev. Lett. **94**, 047006 (2005).

[21] B. Leridon, P. Monod, and D. Colson, *Thermodynamic signature of a phase transition to the pseudogap phase of $YBa_2Cu_3O_x$ high-T_c superconductor*, arXiv:0806.2128 (2008).

[22] F. Raffa, T. Ohno, M. Mali, J. Roos, D. Brinkmann, K. Conder, and M. Eremin, *Isotope Dependence of the Spin Gap in YBa$_2$Cu$_4$O$_8$ as Determined by Cu NQR Relaxation*, Phys. Rev. Lett. **81**, 5912 (1998).

[23] H.-J. Grafe, D. Paar, G. Lang, N. J. Curro, G. Behr, J. Werner, J. Hamann-Borrero, C. Hess, N. Leps, R. Klingeler, and B. Buchner, *^{75}As NMR Studies of Superconducting LaFeAsO$_{0.9}$F$_{0.1}$*, Phys. Rev. Lett. **101**, 047003 (2008).

[24] R. Gonnelli, D. Daghero, M. Tortello, G. Ummarino, V. Stepanov, J. Kim, and R. Kremer, *Coexistence of two order parameters and a pseudogap in the iron-based superconductor LaFeAsO$_{1-x}$F$_x$*, arXiv:0807.3149 (2008).

[25] W. S. Lee, I. M. Vishik, K. Tanaka, D. H. Lu, T. Sasagawa, N. Nagaosa, T. P. Devereaux, and Z. Hussain and Z.-X. Shen, *Abrupt onset of a second energy gap at the superconducting transition of underdoped Bi2212*, Nature (London) **450**, 81 (2007).

[26] Y. H. Liu, Y. Toda, K. Shimatake, N. Momono, M. Oda, and M. Ido, *Direct Observation of the Coexistence of the Pseudogap and Superconducting Quasiparticles in $Bi_2Sr_2CaCu_2O_{8+y}$ by Time-Resolved Optical Spectroscopy*, Phys. Rev. Lett. **101**, 137003 (2008).

[27] A. Kanigel, U. Chatterjee, M. Randeria, M. R. Norman, G. Koren, K. Kadowaki, and J. C. Campuzano, *Evidence for Pairing above the Transition Temperature of Cuprate Superconductors from the Electronic Dispersion in the Pseudogap Phase*, Phys. Rev. Lett. **101**, 137002 (2008).

[28] M. Randeria, N. Trivedi, A. Moreo, and R. T. Scalettar, *Pairing and spin gap in the normal state of short coherence length superconductors*, Phys. Rev. Lett. **69**, 2001 (1992).

[29] V. J. Emery and S. A. Kivelson, *Importance of phase fluctuations in superconductors with small superfluid density*, Nature **374**, 434 (1995).

[30] K. Tanaka, W. S. Lee, D. H. Lu, A. Fujimori, T. Fujii, I. Risdiana, I. Terasaki, D. J. Scalapino, T. P. Devereaux, Z. Hussain, and Z.-X. Shen, *Distinct Fermi-Momentum-Dependent Energy Gaps in Deeply Underdoped Bi2212*, Science **314**, 1910 (2006).

[31] K. Terashima, H. Matsui, T. Sato, T. Takahashi, M. Kofu, and K. Hirota, *Anomalous Momentum Dependence of the Superconducting Coherence Peak and Its Relation to the Pseudogap of $La_{1.85}Sr_{0.15}CuO_4$*, Phys. Rev. Lett. **99**, 017003 (2007).

[32] H. A. Mook, Y. Sidis, B. Fauque, V. Baledent, and P. Bourges, *Observation of magnetic order in a superconducting $YBa_2Cu_3O_{6.6}$ single crystal using polarized neutron scattering*, Phys. Rev. B **78**, 020506 (2008).

[33] B. Fauque, Y. Sidis, V. Hinkov, S. Pailhes, C. T. Lin, X. Chaud, and P. Bourges, *Magnetic Order in the Pseudogap Phase of High-T_c Superconductors*, Phys. Rev. Lett. **96**, 197001 (2006).

[34] Y. Li, V. Baledent, N. Barisic, Y. Cho, B. Fauque, Y. Sidis, G. Yu, X. Zhao, P. Bourges, and M. Greven, *Unusual magnetic order in the pseudogap region of the superconductor $HgBa_2CuO_{4+\delta}$*, Nature (London) **455**, 372 (2008).

[35] G. J. MacDougall, A. A. Aczel, J. P. Carlo, T. Ito, J. Rodriguez, P. L. Russo, Y. J. Uemura, S. Wakimoto, and G. M. Luke, *Absence of Broken Time-Reversal Symmetry in the Pseudogap State of the High Temperature $La_{2-x}Sr_xCuO_4$ Superconductor from Muon-Spin-Relaxation Measurements*, Phys. Rev. Lett. **101** (2008).

[36] A. Shekhter, L. Shu, V. Aji, D. E. MacLaughlin, and C. M. Varma, *Screening of Point Charge Impurities in Highly Anisotropic Metals: Application to μ^+-Spin Relaxation in Underdoped Cuprate Superconductors*, Phys. Rev. Lett. **101**, 227004 (2008).

[37] M. C. Wise, W. D.and Boyer, K. Chatterjee, T. Kondo, T. Takeuchi, H. Ikuta, Y. Wang, and E. W. Hudson, *Charge-density-wave origin of cuprate checkerboard visualized by scanning tunnelling microscopy*, Nature Physics **4**, 696 (2008).

[38] V. J. Emery, S. A. Kivelson, and J. M. Tranquada, *Stripe phases in high-temperature superconductors*, Proceedings of the National Academy of Sciences of the United States of America **96**, 8814 (1999).

[39] M. Mali, J. Roos, H. Keller, A. V. Dooglav, Y. A. Sakhratov, and A. V. Savinkov, *Clues Obtained from the Oxygen Isotope Effect on NMR/NQR Parameters Observed in $YBa_2Cu_4O_8$*, Journal of Superconductivity **15**, 511 (2002).

[40] A. Suter, M. Mali, J. Roos, and D. Brinkmann, *Charge Degree of Freedom and the Single-Spin Fluid Model in $YBa_2Cu_4O_8$*, Phys. Rev. Lett. **84**, 4938 (2000).

[41] T. Moriya, *The effect of electron-electron interaction on the nuclear spin relaxation in metals*, J. Phys. Soc. Japan **18**, 516 (1963).

[42] T. Moriya, Y. Takahashi, and K. Ueda, *Antiferromagnetic Spin Fluctuations and Superconductivity in Two-Dimensional Metals - A Possible Model for High T_c Oxides*, J. Phys. Soc. Japan **59**, 2905 (1990).

[43] C. P. Slichter, S. E. Barrett, J. A. Martindale, D. J. Durand, C. H. Pennington, C. A. Klug, K. E. O'Hara, S. M. DeSoto, T. Imai, J. P. Rice, T. A. Friedmann, and D. M. Ginsberg, *NMR Studies of the Superconducting State of Copper Oxide Superconductors*, Applied Magnetic Resonance **3**, 423 (1992).

[44] J. Rossat-Mignod, L. P. Regnault, C. Vettier, P. Burlet, J. Y. Henry, and G. Lapertot, *Investigation of the spin dynamics in $YBa_2Cu_3O_{6+x}$ by inelastic neutron scattering*, Physica B **169**, 58 (1991).

[45] H. A. Mook, M. Yethiraj, G. Aeppli, T. E. Mason, and T. Armstrong, *Polarized neutron determination of the magnetic excitations in $YBa_2Cu_3O_7$*, Phys. Rev. Lett. **70**, 3490 (1993).

[46] J. Rossat-Mignod, L. P. Regnault, C. Vettier, P. Bourges, P. Burlet, J. Bossy, J. Y. Henry, and G. Lapertot, *Spin dynamics in the high-T_c system $YBa_2Cu_3O_{6+x}$*, Physica B **180-181**, 383 (1992).

[47] B. J. Sternlieb, G. Shirane, J. M. Tranquada, M. Sato, and S. Shamoto, *Temperature dependence of the dynamic susceptibility $\chi''(\omega)$ in superconducting $YBa_2Cu_3O_{6.6}$ ($T_c = 53\,\mathrm{K}$)*, Phys. Rev. B **47**, 5320 (1993).

[48] J. M. Tranquada, P. M. Gehring, G. Shirane, S. Shamoto, and M. Sato, *Neutron-scattering study of the dynamical spin susceptibility in $YBa_2Cu_3O_{6.6}$*, Phys. Rev. B **46**, 5561 (1992).

[49] H. F. Fong, B. Keimer, P. W. Anderson, D. Reznik, F. Doğan, and I. A. Aksay, *Phonon and Magnetic Neutron Scattering at 41 meV in $YBa_2Cu_3O_7$*, Phys. Rev. Lett. **75**, 316 (1995).

[50] A. Abragam, *Principles of Nuclear Magnetism*, Clarendon, Oxford, 1961.

[51] C. Slichter, *Principles of Magnetic Resonance*, Springer, Berlin, 1990.

[52] T. C. Hsu, J. B. Marston, and I. Affleck, *Two observable features of the staggered-flux phase at nonzero doping*, Phys. Rev. B **43**, 2866 (1991).

[53] C. Nayak, *Density-wave states of nonzero angular momentum*, Phys. Rev. B **62**, 4880 (2000).

[54] C. M. Varma, *Theory of the pseudogap state of the cuprates*, Phys. Rev. B **73**, 155113 (2006).

[55] V. Aji and C. M. Varma, *Theory of the Quantum Critical Fluctuations in Cuprate Superconductors*, Phys. Rev. Lett. **99**, 067003 (2007).

[56] J. Xia, E. Schemm, G. Deutscher, S. A. Kivelson, D. A. Bonn, W. N. Hardy, R. Liang, W. Siemons, G. Koster, M. M. Fejer, and A. Kapitulnik, *Polar Kerr-Effect Measurements of the High-Temperature $YBa_2Cu_3O_{6+x}$ Superconductor: Evidence for Broken Symmetry near the Pseudogap Temperature*, Phys. Rev. Lett. **100**, 127002 (2008).

[57] C. Weber, A. Läuchli, F. Mila, and T. Giamarchi, *Orbital currents in extended Hubbard models of high-T_c cuprates*, arXiv:0803.3983 (2008).

[58] J. Y. Genoud, T. Graf, G. Triscone, A. Junod, and J. Muller, *Variation of the superconducting and structural properties of $Y_2Ba_4Cu_7O_z$ with oxygen content ($14.1 < z < 15.3$, $30\ K \leqslant Tc \geqslant 95\ K$)*, Physica C **192**, 137 (1992).

[59] R. Stern, M. Mali, I. Mangelschots, J. Roos, D. Brinkmann, J.-Y. Genoud, T. Graf, and J. Muller, *Charge-carrier density and interplane coupling in $Y_2Ba_4Cu_7O_{15}$: A Cu NMR-NQR study*, Phys. Rev. B **50**, 426 (1994).

[60] M. V. Eremin, I. Eremin, and A. Terzi, *Network patterns and strength of orbital currents in layered cuprates*, Phys. Rev. B **66**, 104524 (2002).

[61] S. A. Kivelson, I. P. Bindloss, E. Fradkin, V. Oganesyan, J. M. Tranquada, A. Kapitulnik, and C. Howald, *How to detect fluctuating stripes in the high-temperature superconductors*, Rev. Mod. Phys. **75**, 1201 (2003).

[62] J. E. Hoffman, E. W. Hudson, K. M. Lang, V. Madhavan, H. Eisaki, S. Uchida, and J. C. Davis, *A Four Unit Cell Periodic Pattern of Quasi-Particle States Surrounding Vortex Cores in $Bi_2Sr_2CaCu_2O_{8+\delta}$*, Science **295**, 466 (2002).

[63] L. P. Gor'kov and G. B. Teitel'baum, *Pseudogap regime in high-Tc cuprates as a manifestation of a frustrated phase separation (NMR view)*, Physica B: Condensed Matter **359-361**, 509 (2005).

[64] S. G. Brass and M. H. Ghandehari, *Synthesis of $LaBa_2Cu_3O_{7?y}$ through tetragonal to orthorhombic phase transition at high oxygen deficiency*, Appl. Phys. Lett. **53**, 2235 (1988).

[65] M.-S. Wu and T.-T. Fang, *Effect of Processing on the Structure, Oxygen Content, and Superconductivity of $LaBa_2Cu_3O_y$*, J. Am. Ceram. Soc. **81**, 1644 (1998).

[66] M. Corti, B. J. Suh, F. Tabak, A. Rigamonti, F. Borsa, M. Xu, and B. Dabrowski, *Flux-line dynamics in $YBa_2Cu_4O_8$ from ^{89}Y NMR*, Phys. Rev. B **54**, 9469 (1996).

[67] A. Maisuradze, R. Khasanov, A. Shengelaya, and H. Keller, *Analysis of μSR line shapes in the vortex state of type-II superconductors*, arXiv:0805.3646 (2008).

[68] M. Tinkham, *Introduction to Superconductivity*, McGraw-Hill Book Co, Singapore, 1996.

[69] F. London and H. London, *The electromagnetic equations of the superconductor*, Proc. Roy. Soc. **A149**, 71 (1935).

[70] V. L. Ginzburg and L. D. Landau, Zh. Eksperim. i. Teor. Fiz. **20**, 1064 (1950).

[71] L. P. Gor'kov, JETP **9**, 1364 (1959).

[72] A. Abrikosov, *On magnetic properties of superconductors of second type*, Soviet Physics JETP **5**, 1174 (1957).

[73] E. H. Brandt, *Flux distribution and penetration depth measured by muon spin rotation in high-T_c superconductors*, Phys. Rev. B **37**, 2349 (1988).

[74] J. White, V. Hinkov, R. Heslop, R. Lycett, E. Forgan, C. Bowell, S. Strässle, A. Abrahamsen, M. Laver, C. Dewhurst, J. Kohlbrecher, J. Gavilano, J. Mesot, B. Keimer, and A. Erb, *Fermi surface and order parameter driven vortex lattice structure transitions in twin-free $YBa_2Cu_3O_7$*, arXiv:0810.1947 (2008).

[75] T. Kondo, T. Takeuchi, U. Mizutani, T. Yokoya, S. Tsuda, and S. Shin, *Contribution of electronic structure to thermoelectric power in $(Bi,Pb)_2(Sr,La)_2CuO_{6+\delta}$*, Phys. Rev. B **72**, 024533 (2005).

[76] H. Brandt, *Properties of the ideal Ginzburg-Landau vortex lattice*, Phys. Rev. B **68**, 054506 (2003).

[77] Y. Wang, S. Ono, Y. Onose, G. Gu, Y. Ando, Y. Tokura, S. Uchida, and N. P. Ong, *Dependence of Upper Critical Field and Pairing Strength on Doping in Cuprates*, Science **299**, 86 (2003).

[78] H. Won and K. Maki, *Nonlinear response and scaling law in the vortex state of d-wave superconductors*, Europhys. Lett. **54**, 248 (2001).

[79] S. L. Lee, P. Zimmermann, H. Keller, M. Warden, I. M. Savić, R. Schauwecker, D. Zech, R. Cubitt, E. M. Forgan, P. H. Kes, T. W. Li, A. A. Menovsky, and Z. Tarnawski, *Evidence for flux-lattice melting and a dimensional crossover in single-crystal $Bi_{2.15}Sr_{1.85}CaCu_2O_{8+\delta}$ from muon spin rotation studies*, Phys. Rev. Lett. **71**, 3862 (1993).

[80] T. M. Riseman, J. H. Brewer, K. H. Chow, W. N. Hardy, R. F. Kiefl, S. R. Kreitzman, R. Liang, W. A. MacFarlane, P. Mendels, G. D. Morris, J. Rammer, J. W. Schneider, C. Niedermayer, and S. L. Lee, *Ginzburg-Landau parameter in $YBa_2Cu_3O_{6.95}$ below the irreversibility temperature as measured by μ^+SR in high magnetic fields*, Phys. Rev. B **52**, 10569 (1995).

[81] R. Khasanov, A. Shengelaya, A. Maisuradze, F. L. Mattina, A. Bussmann-Holder, H. Keller, and K. A. Müller, *Experimental Evidence for Two Gaps in the High-Temperature $La_{1.83}Sr_{0.17}CuO_4$ Superconductor*, Phys. Rev. Lett. **98**, 057007 (2007).

[82] A. Carrington and F. Manzano, *Magnetic penetration depth of MgB_2*, Physica C **385**, 205 (2003).

[83] K. Ichimura, K. Nomura, F. Minami, and S. Takekawa, *Scanning tunnelling spectroscopy of an oxide superconductor $Bi_2Sr_2CaCu_2O_{8-\delta}$*, Journal of Physics: Condensed Matter **2**, 9961 (1990).

[84] W. Guyard, M. L. Tacon, M. Cazayous, A. Sacuto, A. Georges, D. Colson, and A. Forget, *Breakpoint in the evolution of the gap through the cuprate phase diagram*, Phys. Rev. B **77**, 024524 (2008).

[85] L. Gao, Z. Huang, R. Meng, J. Lin, F. Chen, L. Beauvais, Y. Sun, Y. Xue, and C. Chu, *Study of superconductivity in the Hg-Ba-Ca-Cu-O system*, Physica C **213**, 261 (1993).

[86] M.-S. Kim, J. A. Skinta, T. R. Lemberger, W. N. Kang, H.-J. Kim, E.-M. Choi, and S.-I. Lee, *Reflection of a two-gap nature in penetration-depth measurements of MgB_2 film*, Phys. Rev. B **66**, 064511 (2002).

[87] C. Niedermayer, C. Bernhard, T. Holden, R. K. Kremer, and K. Ahn, *Muon spin relaxation study of the magnetic penetration depth in MgB_2*, Phys. Rev. B **65**, 094512 (2002).

[88] D. D. Castro, M. Angst, D. G. Eshchenko, R. Khasanov, J. Roos, I. M. Savić, A. Shengelaya, S. L. Bud'ko, P. C. Canfield, K. Conder, J. Karpinski, S. M. Kazakov, R. A. Ribeiro, and H. Keller, *Absence of a boron isotope effect in the magnetic penetration depth of MgB_2*, Phys. Rev. B **70**, 014519 (2004).

[89] F. Hunte, J. Jaroszynski, A. Gurevich, D. C. Larbalestier, R. Jin, A. S. Sefat, M. A. McGuire, B. C. Sales, D. K. Christen, and D. Mandrus, *Two-band superconductivity in $LaFeAsO_{0.89}F_{0.11}$ at very high magnetic fields*, Nature **453**, 903 (2008).

[90] S. Weyeneth, U. Mosele, N. Zhigadlo, S. Katrych, Z. Bukowski, J. Karpinski, S. Kohout, J. Roos, and H. Keller, *Anisotropy of superconducting single crystal $SmFeAsO_{0.8}F_{0.2}$ studied by torque magnetometry*, arXiv:0806.1024 (2008).

[91] R. E. Glover and M. Tinkham, *Conductivity of Superconducting Films for Photon Energies between 0.3 and $4kT_c$*, Phys. Rev. **108**, 243 (1957).

[92] E. Maxwell, *Isotope Effect in the Superconductivity of Mercury*, Phys. Rev. **78**, 477 (1950).

[93] C. A. Reynolds, B. Serin, W. H. Wright, and L. B. Nesbitt, *Superconductivity of Isotopes of Mercury*, Phys. Rev. **78**, 487 (1950).

[94] H. Fröhlich, *Isotope Effect in Superconductivity*, Proc. Phys. Soc. **A63**, 778 (1950).

[95] J. Bardeen, *Zero-Point Vibrations and Superconductivity*, Phys. Rev. **79**, 167 (1950).

[96] G. M. Eliashberg, Soviet Phys. JETP **11**, 696 (1960).

[97] G. M. Eliashberg, Soviet Phys. JETP **12**, 1000 (1961).

[98] W. L. McMillan, *Transition Temperature of Strong-Coupled Superconductors*, Phys. Rev. **167**, 331 (1968).

[99] P. B. Allen and R. C. Dynes, *Transition temperature of strong-coupled superconductors reanalyzed*, Phys. Rev. B **12**, 905 (1975).

[100] H. Keller, *Superconductivity in Complex Systems,* ed. K. A. Müller and A. Bussmann-Holder, Springer Series Structure and Bonding **114**, 143 (2005).

[101] G. M. Zhao and D. E. Morris, *Observation of a possible oxygen isotope effect on the effective mass of carriers in $YBa_2Cu_3O_{6.94}$*, Phys. Rev. B **51**, 16487 (1995).

[102] G. M. Zhao, M. B. Hunt, H. Keller, and K. A. Müller, *Evidence for polaronic supercarriers in the copper oxide superconductors $La_{2x}Sr_xCuO_4$*, Nature (London) **385**, 236 (1997).

[103] J. Hofer, K. Conder, T. Sasagawa, G. M. Zhao, M. Willemin, H. Keller, and K. Kishio, *Oxygen-Isotope Effect on the In-Plane Penetration Depth in Underdoped $La_{2x}Sr_xCuO_4$ Single Crystals*, Phys. Rev. Lett. **84**, 4192 (2000).

[104] R. Khasanov, D. G. Eshchenko, H. Luetkens, E. Morenzoni, T. Prokscha, A. Suter, N. Garifianov, M. Mali, J. Roos, K. Conder, and H. Keller, *Direct Observation of the Oxygen Isotope Effect on the In-Plane Magnetic Field Penetration Depth in Optimally Doped $YBa_2Cu_3O_{7-\delta}$*, Phys. Rev. Lett. **92**, 057602 (2004).

[105] K. Conder, *Oxygen diffusion in the superconductors of the YBaCuO family: isotope exchange measurements and models*, Mater. Sci. Eng. **R32**, 41 (2001).

[106] C. Panagopoulos, J. R. Cooper, G. B. Peacock, I. Gameson, P. P. Edwards, W. Schmidbauer, and J. W. Hodby, *Anisotropic magnetic penetration depth of grain-aligned* $HgBa_2Ca_2Cu_3O_{8+\delta}$, Phys. Rev. B **53**, R2999 (1996).

[107] D. Shoenberg, *Properties of Superconducting Colloids and Emulsions*, Proc. Roy. Soc. **A175**, 49 (1940).

[108] V. I. Fesenko, V. N. Gorbunov, and V. P. Smilga, *Analytical properties of muon polarization spectra in type-II superconductors and experimental data interpretation for mono- and polycrystalline HTSCs*, Physica C **176**, 551 (1991).

[109] C. L. Seaman, J. J. Neumeier, M. B. Maple, L. P. Le, G. M. Luke, B. J. Sternlieb, Y. J. Uemura, J. H. Brewer, R. Kadono, R. F. Kiefl, S. R. Krietzman, and T. M. Riseman, *Magnetic penetration depth of* $Y_{1-x}Pr_xBa_2Cu_3O_{6.97}$ *measured by muon-spin relaxation*, Phys. Rev. B **42**, 6801 (1990).

[110] R. Khasanov, A. Shengelaya, D. D. Castro, E. Morenzoni, A. Maisuradze, I. M. Savic, K. Conder, E. Pomjakushina, and H. Keller, *Oxygen isotope effect on superconductivity and magnetism in* $Y_{1-x}Pr_xBa_2Cu_3O_{7-\delta}$, arXiv:0711.2257v1 (2008).

[111] A. Bussmann-Holder and H. Keller, *Polaron effects in high-temperature cuprate superconductors,* in *Polarons in Advanced Materials*, Springer Series in Materials Science **103**, 599 (2007).

[112] A. Kohen, G. Leibovitch, and G. Deutscher, *Andreev Reflections on* $Y_{1-x}Ca_xBa_2Cu_3O_{7-\delta}$*: Evidence for an Unusual Proximity Effect*, Phys. Rev. Lett. **90**, 207005.

[113] R. Khasanov, A. Shengelaya, J. Karpinski, A. Bussmann-Holder, H. Keller, and K. A. Müller, *s-Wave Symmetry Along the c-Axis and* $s + d$ *In-plane Superconductivity in Bulk* $YBa_2Cu_4O_8$, J. Supercond. Novel Magn. **21**, 81 (2008).

[114] R. Khasanov, S. Strässle, D. D. Castro, T. Masui, S. Miyasaka, S. Tajima, A. Bussmann-Holder, and H. Keller, *Multiple Gap Symmetries for the Order Parameter of Cuprate Superconductors from Penetration Depth Measurements*, Phys. Rev. Lett. **99**, 237601 (2007).

[115] N.-C. Yeh, C.-T. Chen, G. Hammerl, J. Mannhart, A. Schmehl, C. W. Schneider, R. R. Schulz, S. Tajima, K. Yoshida, D. Garrigus, and M. Strasik, *Evidence of Doping-Dependent Pairing Symmetry in Cuprate Superconductors*, Phys. Rev. Lett. **87**, 087003 (2001).

[116] M. C. Boyer, W. D. Wise, K. Chatterjee, T. Kondo, T. Takeuchi, H. Ikuta, and E. W. Hudson, *Imaging the two gaps of the high-temperature superconductor* $Bi_2Sr_2CuO_{6+x}$, Nat. Phys. **3**, 802 (2007).

[117] K. K. Gomes, N. A. Pasupathy, A. Pushp, S. Ono, Y. Ando, and A. Yazdani, *Visualizing pair formation on the atomic scale in the high-*T_c *superconductor* $Bi_2Sr_2CaCu_2O_{8+\delta}$, Nature (London) **447**, 569 (2007).

[118] S. Sugai, H. Suzuki, Y. Takayanagi, T. Hosokawa, and N. Hayamizu, *Carrier-density-dependent momentum shift of the coherent peak and the LO phonon mode in p-type high-T_c superconductors*, Phys. Rev. B **68**, 184504 (2003).

[119] H. Suhl, B. T. Matthias, and L. R. Walker, *Bardeen-Cooper-Schrieffer Theory of Superconductivity in the Case of Overlapping Bands*, Phys. Rev. Lett. **3**, 552 (1959).

[120] A. Bussmann-Holder, R. Micnas, and A. R. Bishop, *Enhancements of the superconducting transition temperature within the two-band model*, Eur. Phys. J. B **37**, 345 (2003).

[121] G. Binnig, A. Baratoff, H. E. Hoenig, and J. G. Bednorz, *Two-Band Superconductivity in Nb-Doped $SrTiO_3$*, Phys. Rev. Lett. **45**, 1352 (1980).

[122] R. S. Gonnelli, D. Daghero, G. A. Ummarino, V. A. Stepanov, J. Jun, S. M. Kazakov, and J. Karpinski, *Direct Evidence for Two-Band Superconductivity in MgB_2 Single Crystals from Directional Point-Contact Spectroscopy in Magnetic Fields*, Phys. Rev. Lett. **89**, 247004 (2002).

[123] A. Floris, A. Sanna, M. Lüders, G. Profeta, N. N. Lathiotakis, M. A. L. Marques, C. Franchini, E. K. U. Gross, A. Continenza, and S. Massidda, *Superconducting properties of MgB_2 from first principles*, Physica C **456**, 45 (2007).

[124] A. Bussmann-Holder, R. Khasanov, A. Shengelaya, A. Maisuradze, F. LaMattina, H. Keller, and K. A. Müller, *Mixed order parameter symmetries in cuprate superconductors*, Eur. Phys. Lett. **77**, 27002 (2007).

[125] K. A. Müller, *Possible coexistence of s- and d-wave condensates in copper oxide superconductors*, Nature (London) **377**, 133 (1995).

[126] K. Matano, Z. A. Ren, X. L. Dong, L. L. Sun, Z. X. Zhao, and G. Q. Zheng, *Spin-singlet superconductivity with multiple gaps in $PrFeAsO_{0.89}F_{0.11}$*, Europhys. Lett. **83**, 57001 (2008).

[127] J. A. Martindale, P. C. Hammel, W. L. Hults, and J. L. Smith, *Temperature dependence of the anisotropy of the planar oxygen nuclear spin-lattice relaxation rate in $YBa_2Cu_3O_y$*, Phys. Rev. B **57**, 11769 (1998).

[128] D. H. Lu, D. L. Feng, N. P. Armitage, K. M. Shen, A. Damascelli, C. Kim, F. Ronning, Z.-X. Shen, D. A. Bonn, R. Liang, W. N. Hardy, A. I. Rykov, and S. Tajima, *Superconducting Gap and Strong In-Plane Anisotropy in Untwinned $YBa_2Cu_3O_{7-\delta}$*, Phys. Rev. Lett. **86**, 4370 (2001).

[129] T. Masui, M. Limonov, H. Uchiyama, S. Lee, S. Tajima, and A. Yamanaka, *Raman study of carrier-overdoping effects on the gap in high-T_c superconducting cuprates*, Phys. Rev. B **68**, 060506 (2003).

[130] B. Friedl, C. Thomsen, and M. Cardona, *Determination of the superconducting gap in $RBa_2Cu_3O_{7-\delta}$*, Phys. Rev. Lett. **65**, 915 (1990).

[131] G. Deutscher, *Andreev-Saint-James reflections: A probe of cuprate superconductors*, Reviews of Modern Physics **77**, 109 (2005).

[132] H. J. H. Smilde, A. A. Golubov, Ariando, G. Rijnders, J. M. Dekkers, S. Harkema, D. H. A. Blank, H. Rogalla, and H. Hilgenkamp, *Admixtures to d-Wave Gap Symmetry in Untwinned $YBa_2Cu_3O_7$ Superconducting Films Measured by Angle-Resolved Electron Tunneling*, Phys. Rev. Lett. **95**, 257001 (2005).

[133] A. Furrer, *Imaging the two gaps of the high-temperature superconductor $Bi_2Sr_2CuO_{6+x}$,* in *High-T_c Superconductors and Related Transition Metal Compounds* ed. A. Bussmann-Holder and H. Keller, Springer (New York) , 135 (2007).

[134] A. G. Sun, D. A. Gajewski, M. B. Maple, and R. C. Dynes, *Observation of Josephson pair tunneling between a high-T_c cuprate ($YBa_2Cu_3O_{7-\delta}$) and a conventional superconductor (Pb)*, Phys. Rev. Lett. **72**, 2267 (1994).

[135] V. V. Kabanov, J. Demsar, B. Podobnik, and D. Mihailovic, *Quasiparticle relaxation dynamics in superconductors with different gap structures: Theory and experiments on $YBa_2Cu_3O_{7-\delta}$*, Phys. Rev. B **59**, 1497 (1999).

[136] K. A. Müller, Inst. Phys. Conf. Ser. **181**, 3 (2004).

[137] Y. Yamada and Y. Shiohara, *Continuous crystal growth of $YBa_2Cu_3O_{7-x}$ by the modified top-seeded crystal pulling method*, Physica C **217**, 182 (1993).

[138] J. D. Jorgensen, M. A. Beno, D. G. Hinks, L. Soderholm, K. J. Volin, R. L. Hitterman, J. D. Grace, I. K. Schuller, C. U. Segre, K. Zhang, and M. S. Kleefisch, *Oxygen ordering and the orthorhombic-to-tetragonal phase transition in $YBa_2Cu_3O_{7-x}$*, Phys. Rev. B **36**, 3608 (1987).

[139] S. L. Thiemann, Z. Radović, and V. G. Kogan, *Field structure of vortex lattices in uniaxial superconductors*, Phys. Rev. B **39**, 11406 (1989).

[140] B. Mühlschlegel, *Die thermodynamischen Funktionen des Supraleiters*, Z. Phys. **155**, 313 (1959).

[141] C. C. Tsuei, J. R. Kirtley, C. C. Chi, L. S. Yu-Jahnes, A. Gupta, T. Shaw, J. Z. Sun, and M. B. Ketchen, *Pairing Symmetry and Flux Quantization in a Tricrystal Superconducting Ring of $YBa_2Cu_3O_{7-\delta}$*, Phys. Rev. Lett. **73**, 593 (1994).

[142] J. Nagamatsu, N. Nakagawa, T. Muranaka, Y. Zenitani, and J. Akimitsu, *Superconductivity at 39K in magnesium diboride*, Nature **410**, 63 (2001).

[143] X. X. Xi, *Two-band superconductor magnesium diboride*, Rep. Prog. Phys. **71**, 116501 (2008).

[144] J. Karpinski, M. Angst, J. Jun, S. Kazakov, R. Puzniak, A. Wisniewski, J. Roos, H. Keller, L. Degiorgi, M. Eskildsen, L. Vinnikov, and A. Mironov, *MgB_2 single crystals: high pressure growth and physical properties*, Supercond. Sci. Technol. **16**, 221 (2003).

List of publications

- **S. Strässle**, J. Roos, M. Mali, H. Keller, and J. Karpinski, ^{11}B *NMR study of single-crystal* MgB_2 *in the normal conducting phase*, Physica C **466**, 168 (2007).

- **S. Strässle**, J. Roos, M. Mali, K. Conder, E. Pomjakushina, and H. Keller, ^{139}La *NMR and NQR investigations of the superconductor* $LaBa_2Cu_3O_{7-\delta}$, Physica C **460-462**, 890 (2007).

- R. Khasanov, **S. Strässle**, D. Di Castro, T. Masui, S. Miyasaka, S. Tajima, A. Bussmann-Holder, and H. Keller, *Multiple Gap Symmetries for the Order Parameter of Cuprate Superconductors from Penetration Depth Measurements*, Physical Review Letters **99**, 237601 (2007).

- R. Khasanov, **S. Strässle**, K. Conder, E. Pomjakushina, A. Bussmann-Holder, and H. Keller, *Universal correlations of isotope effects in* $Y_{1-x}Pr_xBa_2Cu_3O_{7-\delta}$, Physical Review B **77**, 104530 (2008).

- R. Khasanov, Takeshi Kondo, **S. Strässle**, D.O.G. Heron, A. Kaminski, H. Keller, S.L. Lee, and Tsunehiro Takeuchi, *Evidence for competition between the superconducting and the pseudogap state in* $(BiPb)_2(SrLa)_2CuO_{6+\delta}$ *from muon-spin rotation experiments*, Physical Review Letters **101**, 227002 (2008).

- **S. Strässle**, J. Roos, M. Mali, T. Ohno, and H. Keller, *Lack of evidence for orbital-current effects in* $Y_2Ba_4Cu_7O_{15-\delta}$ *from* ^{89}Y *NMR*, Physical Review Letters **101**, 237001 (2008).

- **S. Strässle**, R. Khasanov, T. Kondo, D.O.G. Heron, A. Kaminski, H. Keller, S.L. Lee, and T. Takeuchi, *Superfluid density and angular dependence of the energy gap in optimally doped* $(BiPb)_2(SrLa)_2CuO_{6+\delta}$, Journal of Superconductivity and Novel Magnetism **22**, 189 (2009).

- R. Khasanov, Takeshi Kondo, **S. Strässle**, D.O.G. Heron, A. Kaminski, H. Keller, S.L. Lee, and Tsunehiro Takeuchi, *Zero-field superfluid density in* $d-wave$ *superconductor evaluated from the results of muon-spin-rotation experiments in the mixed state*, Physical Review B **79**, 180507 (2009).

- J.S. White, V. Hinkov, R.W. Heslop, R.J. Lycett, E.M. Forgan, C. Bowell, **S. Strässle**, A.B. Abrahamsen, M. Laver, C.D. Dewhurst, J. Kohlbrecher, J.L. Gavilano, J. Mesot, B. Keimer, and A. Erb, *Fermi surface and order parameter driven vortex lattice structure transitions in twin-free* $YBa_2Cu_3O_7$, Physical Review Letters **102**, 097001 (2009).